Politecnico di Torino

ScuDo
Scuola di Dottorato ~ Doctoral School
WHAT YOU ARE, TAKES YOU FAR

Doctoral Dissertation
Doctoral Program in Physics (36^{th}cycle)

MHD stability of magnetically confined plasmas in presence of superthermal particles

Vertical Displacement Oscillatory Modes

By

Tommaso Barberis

******

Supervisor(s):
Prof. Francesco Porcelli, Supervisor

Doctoral Examination Committee:
Prof. J. Graves, Referee, University of York
Prof. F. Pegoraro , Referee, University of Pisa
Prof. F. Laviano, Polytechnic University of Turin
Dr. S. Sharapov, Culham Centre for Fusion Energy
Prof. F. Zonca, E.N.E.A. C.R. Frascati

Politecnico di Torino
2024

Declaration

I hereby declare that, the contents and organization of this dissertation constitute my own original work and does not compromise in any way the rights of third parties, including those relating to the security of personal data.

Tommaso Barberis
2024

* This dissertation is presented in partial fulfillment of the requirements for **Ph.D. degree** in the Graduate School of Politecnico di Torino (ScuDo).

Acknowledgements

I would like to express my deepest gratitude to my supervisor, Prof. F. Porcelli, for his invaluable guidance, support, and encouragement throughout my PhD journey and even before. His expertise, wisdom, and unwavering commitment have been instrumental in shaping my research and academic growth. Additionally, I extend my great thanks to Dr. C. Kim and Dr. S. Sharapov for their mentorship, insightful discussions, and invaluable contributions to my understanding of theoretical, numerical, and experimental aspects of plasma physics.

I am also grateful very to my colleagues, Stefano, Matteo, Luca, Lorenzo, and Elisa, for their, collaboration, support and for the fun times. I would like to acknowledge my friends, both old and new, whose encouragement, companionship, and laughter have provided solace and joy during challenging times.

Last but not least, I am deeply thankful to my family and my parents for their unconditional love, encouragement, and unwavering belief in my abilities. Their support has been my pillar of strength throughout this journey.

Thank you all for being a part of my life and for contributing to my growth as a researcher and as an individual.

Abstract

Axisymmetric modes in elongated plasmas are normally associated with a well-known ideal instability resulting in a vertical shift of the whole plasma column. This vertical instability is stabilized by means of passive feedback consisting of eddy currents induced by the plasma motion in a nearby wall and/or in plasma-facing components. When a thin resistive wall is considered, the n=0 mode dispersion relation can be studied analytically with reduced ideal Magneto Hydrodynamic (MHD) models and is cubic. Under relevant conditions, two roots are oscillatory and weakly damped. These oscillatory modes present Alfvénic frequency and are dependent on plasma elongation and on the relative position of the plasma boundary and of the wall. The third root is unstable and represents the so-called resistive wall mode (RWM). We focus on the two oscillatory modes, dubbed Vertical Displacement Oscillatory Modes (VDOM), that can be driven unstable due to their resonant interaction with energetic ions. The fast ion drive, involving MeV ions in present days tokamak experiments such as JET, may overcome dissipative and resistive wall damping, setting an instability threshold. The effects of energetic particles are added within the framework of the hybrid kinetic-MHD model. An energetic ion distribution function with $\partial F/\partial E > 0$ is required to drive the instability, achievable with pitch angle anisotropy or with an isotropic distribution in velocity space with regions of positive slope as a function of energy. The latter situation can be achieved by considering losses of fast ions or due to fast ion source modulation. The theory presented here is partly motivated by the observation of saturated n=0 fluctuations in the Joint European Torus (JET), which were initially interpreted in terms of a saturated n=0 Global Alfvén Eigenmode (GAE). Modeling of recent JET discharges using the NIMROD extended-MHD code will be presented, focusing on mode structure and frequency dependence. It is early for us to conclude whether the mode observed at JET is a VDOM rather than a GAE, nevertheless, we discuss

the main points of distinction between GAE and VDOM that may facilitate their experimental identification.

Contents

List of Figures

List of Tables

Chapter 1

Introduction

1.1 Nuclear fusion

Nuclear fusion reactions occur when two light nuclei combine, releasing a large amount of energy due to a slight loss of mass during the process. Stars derive their energy from such reactions. Since the latter half of the 20th century, scientists have been actively researching controlled thermonuclear fusion as a means of producing electricity.

The development of a functional fusion reactor still stands now as a significant scientific challenge. The successful realization of controlled thermonuclear fusion as a novel energy source holds immense potential, impacting both societal and environmental perspectives. This pursuit involves harnessing the energy generated by fusion reactions in a controlled manner for practical electricity generation, presenting an opportunity for a clean and nearly limitless power supply. The realization of a fusion reactor represents a substantial scientific and technological milestone, with far-reaching implications for meeting our increasing energy demands. It transcends mere scientific curiosity, evolving into a critical solution for addressing our current and future energy needs while prioritizing environmental sustainability. In essence, the journey toward controlled fusion is not solely a scientific endeavor but a pathway that could revolutionize our approach to energy production in the 21st century.

The complexities inherent in mastering nuclear fusion lie in the extreme conditions essential for its realization. Fusion reactions need exceedingly high temperatures to occur. In such conditions, nuclei acquire enough energy to overcome the

strong repulsion between positively charged nuclei, known as the Coulomb barrier. This overcoming of the Coulomb barrier is facilitated by a quantum mechanical phenomenon called tunneling. Despite lacking sufficient classical energy to surpass the barrier, there is a small probability that particles can tunnel through it due to their wave-like nature. When nuclei tunnel through the barrier, they come within range of the strong nuclear force, which is attractive at very short distances. This force then binds the nuclei together, resulting in nuclear fusion. This reaction results in the release of a large amount of energy. Therefore, the exploitation of controlled nuclear fusion demands the creation and sustenance of these complex and extreme conditions, representing a significant scientific and engineering challenge.

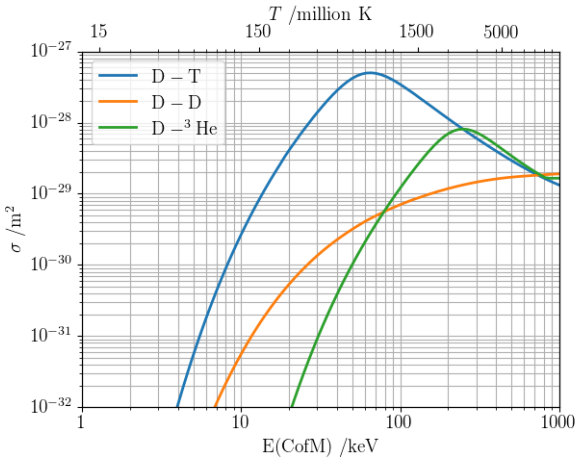

Fig. 1.1 Fusion reaction cross sections as a function of the centre of mass energy (temperature)

Figure (1.1) depicts the cross section for various nuclear fusion reactions plotted against the center of mass energy. Achieving a noteworthy cross section necessitates high energies, pushing the fuel into a plasma state, a state of matter characterized by ionization, where collective phenomena play a crucial role. Figure 1.1 also underscores why contemporary fusion research predominantly concentrates on deuterium-tritium (D-T) plasmas.

The specific fusion reaction considered is:

$$ {}^{2}_{1}D + {}^{3}_{1}T \rightarrow {}^{4}_{2}He(3.5MeV) + {}^{1}_{0}n(14.1MeV). \tag{1.1} $$

This reaction exhibits the highest fusion cross section at a lower temperature with respect to other reactions. This particular reaction, offers a balance where a substantial cross section is achievable at temperatures that align with experimental conditions.

To harness fusion energy in laboratory environments, it is crucial to satisfy a well-established condition known as the Lawson criterion [4]. In the context of the deuterium-tritium (D-T) reaction, the ${}^4_2He$ particles, often referred to as α particles, play a pivotal role. Their task is to exchange their energy to the plasma, ensuring the self-sustaining high-temperature condition required for continuous thermonuclear burn. This process is essential for maintaining the balance between energy losses and inputs, enabling the effective exploitation of fusion energy in controlled laboratory settings.

$$\frac{dW}{dt} = P_{aux} + P_{\alpha} - P_{loss} \tag{1.2}$$

Here $W \sim 3nT$ is the energy density of a plasma with temperature T and density $n = n_{electrons} = n_{ions}$. The plasma heating input power is represented by P_{aux}; P_{α} is the α particles heating power density and P_{loss} takes into account the different losses caused by conducting, radiative and convective phenomena. In order to quantify the power losses, the plasma confinement time, τ_E, is introduced: $P_{loss} = W/\tau_E \sim 3nT/\tau_E$. The alpha particles heating in a D-T plasma, follows:

$$P_{\alpha} = n_D n_T \langle \sigma v \rangle \mathscr{E}_{\alpha} = \frac{1}{4} n^2 \langle \sigma v \rangle \mathscr{E}_{\alpha} \tag{1.3}$$

where $\mathscr{E}_{\alpha} = 3.5MeV$ and $\langle \sigma v \rangle$ is the velocity averaged fusion reaction cross section. For a D-T plasma with temperature between $10keV$ and $20keV$, the fusion reaction rate can be approximated by $\langle \sigma v \rangle \simeq c_0 T^2$. The criterion for ignition, requiring the alpha heating to overcome the power losses without auxiliary heating, $P_{\alpha} \geq P_{loss}$, can be written as:

$$n\tau_E T > \frac{12}{\mathscr{E}_{\alpha} c_0} > 3 \times 10^{21} keV \cdot s \cdot m^{-3} \tag{1.4}$$

where $n\tau_E T$ is typically referred as the “fusion triple product".

To satisfy the relation of Eq. (1.4) in laboratory plasmas, researchers have explored two distinct approaches: *inertial* confinement and *magnetic* confinement. The former involves high-power lasers to heat and compress a fuel pellet, achieving

remarkably high densities ($n \sim 10^{31} m^{-3}$) within an extremely brief confinement time $\tau_E \sim 10^{-11} s$. Very recent experiments reported outstanding advancements of the inertial fusion approach [5]. Conversely, magnetic confinement relies on the use of strong magnetic fields to confine a plasma with lower density ($n \sim 10^{20} m^{-3}$) for a confinement time exceeding $\tau_E \sim 1s$.

The magnetic confinement method takes advantage of the fundamental nature of a plasma, comprising charged particles responsive to electromagnetic fields. When subject to the Lorentz force, a moving charged particle exhibit a gyrating motion characterized by a finite excursion referred to as the *Larmor radius* and a frequency known as the *cyclotron* frequency. In magnetic confinement devices, the magnetic field is carefully engineered to ensure that the drift motions of particles remain small compared to their Larmor radius. As a result, particles predominantly follow the magnetic field lines, which act as guides, preventing plasma particles from reaching the walls of the device. This magnetic configuration effectively serves as a containment structure for the plasma. The magnetic force thus acts against the plasma pressure that tends to make the plasma expand outwards. This is described using the ratio between plasma pressure and magnetic pressure, called β parameter:

$$\beta = \frac{8\pi n k_b T}{B^2}. \tag{1.5}$$

Good confinement is characterized by $\beta \ll 1$. Since the early stages of research in controlled nuclear fusion, a variety of magnetic confinement devices have been conceptualized and thoroughly examined. The majority of contemporary fusion experiments draw inspiration from the success of a well-established design known as Tokamak.

1.2 Tokamak

The tokamak, conceived by the Soviets in the late '60s, remains a cornerstone in controlled nuclear fusion research. While modifications have been implemented to improve its performance, the fundamental principles of the tokamak design persist in present-day machines. Figure (1.2) illustrates the core schematic of a tokamak: external toroidal field coils induce a toroidal magnetic field, and the plasma current itself generates a poloidal field, resulting in a total helical magnetic field.

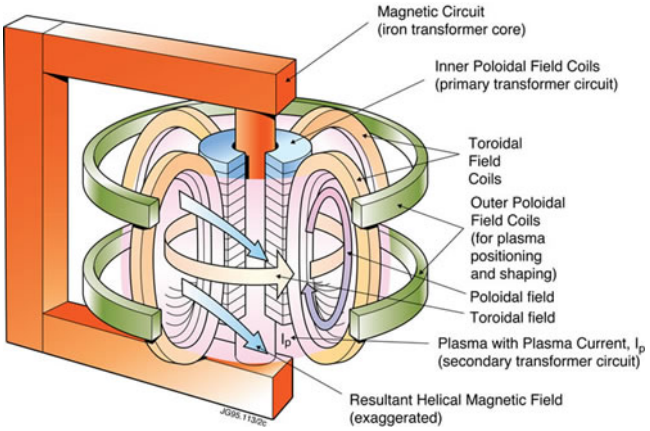

Fig. 1.2 Simplified Tokamak scheme.

This plasma current is induced within a transformer circuit, where the internal solenoid serves as the primary component. External poloidal coils play a crucial role in shaping the plasma and adjusting its vertical position. The ohmic heating, originating from the plasma current, contributes to heating the plasma, yet its efficiency diminishes at higher temperatures, due to the resistivity scaling with temperature, $\eta \propto T^{-3/2}$. To reach the high temperatures required for fusion, several heating methods have been developed. Notably, neutral beam injection (NBI) involves launching high-energy neutrals into the plasma, while ion cyclotron resonant heating (ICRH) employs high-power, $\sim$ 10MHz electromagnetic waves, resonant with the ion cyclotron motion. Both these techniques introduce ions in the plasma with energies that can be order of magnitudes larger with respect to the plasma thermal energy. These *energetic ions* will decelerate through collisions, mainly with electrons, heating the plasma in the process. The other common heating technique is the electron cyclotron resonant heating (ECRH), which uses $\sim$ 100GHz electromagnetic waves to transfer energy to the electrons.

The most promising path toward achieving controlled thermonuclear fusion as a new energy source currently revolves around the tokamak devices. Numerous projects are in various stages of development, offering potential breakthroughs in fusion research. Worldwide, several tokamak experiments are actively operating. Among these, the JET (Joint European Torus) tokamak experiment stands out as possibly the one that obtained the most advanced performances. Unfortunately, the decommissioning of JET started while this thesis is being written. Nevertheless, JET has yielded numerous noteworthy results during its very long operation. Very recent

experimental observations from JET play a crucial role in the context of the research presented in this work.

The leading next-step in tokamak device is the ITER project, the International Tokamak Experimental Reactor. Currently under construction in southern France, ITER represents a collaborative effort involving technologically advanced countries worldwide. On an italian national level, the Divertor Test Tokamak experiment (DTT) is now undert construction at the ENEA laboratories in Frascati. Meanwhile, at MIT, the SPARC project, a compact, high magnetic field device that holds promise for advancing fusion research, will be completed before the end of the decade.

1.3 Equilibrium and stability

The performance of a magnetic confinement device is undoubtedly tied to the principles of equilibrium and stability. The study of these properties in plasmas is often conducted using a fluid model known as *Magneto Hydro Dynamics* (MHD), which will be discussed in Chapter 3 and is further detailed in Ref. [1].

To provide an introductory overview, it's important to highlight that achieving and maintaining MHD equilibrium and stability are indispensable prerequisites for a magnetic confinement device. Instabilities within the plasma can lead to various adverse outcomes, ranging from a deterioration in device performance to the sudden termination of the plasma, a phenomenon called *plasma disruption*, that may endanger the machine integrity. Therefore, a thorough understanding and control of MHD equilibrium and stability are critical factors in the design and operation of magnetic confinement devices for successful plasma discharges. The primary goal of MHD in the context of magnetic fusion, is to investigate a magnetic configuration capable of maintaining a stable equilibrium. This equilibrium must have parameters, such as plasma pressure and current, sufficiently large to satisfy the criteria outlined in Eq. (1.4) achieving and sustaining controlled thermonuclear fusion. An important outcome of ideal MHD is that plasma stability can be explored through the analysis of normal modes of the plasma. These modes involve oscillations around the torus and in the poloidal direction, characterized by toroidal and poloidal mode numbers denoted as n and m, respectively. These integer numbers define the number of oscillations along each direction. This approach allows for a comprehensive study of the dynamic behavior of the plasma system and the associated magnetic field,

providing valuable insights into the stability characteristics of the fusion device. In the realm of MHD, a rich nomenclature of model variations can be identified based on distinct assumptions and simplifications. The most simple variant is the "Ideal MHD" model, characterized by numerous simplifications, that often allows for analytic work and can describe some of the most dangerous plasma instabilities. Moving beyond the simplicity of Ideal MHD, more sophisticated versions are often labeled as "extended MHD". These advanced versions take into account factors such as finite resistivity or kinetic effects, offering a more comprehensive understanding of plasma behavior.

In this thesis, particular attention will be directed towards the significance of kinetic effects associated with the presence of *energetic ions*. To investigate the impact of energetic ions on the MHD stability of the plasma, we will introduce the hybrid kinetic MHD model in Chapter 3. The presence of ions with energies significantly higher than the plasma's thermal energy holds crucial implications for plasma stability. A notable example are sawtooth oscillations, periodic relaxations of the plasma profile induced by plasma instabilities. The presence of energetic ions can lead to the occurrence of "monster" sawteeth, characterized by a substantial increase in both period and amplitude of these relaxations. Without proper consideration, sawtooth oscillations may result in disruptions, posing concerns for new high-performance devices, such as DTT [6].

1.4 Content of the thesis

Within the framework of normal modes arising from Ideal MHD in the tokamak configuration, toroidally axisymmetric modes, characterized by toroidal mode number $n = 0$, take center stage in this thesis. These modes exhibit a notable characteristic: their structure is constant along the toroidal direction. In tokamak plasmas, various types of axisymmetric modes, such as geodesic acoustic modes and global Alfvén modes, have been observed and extensively investigated.

Of particular interest for our investigation are vertical displacement oscillatory modes, a type of axisymmetric mode that has received comparatively less attention. These modes emerge due to the non-circular plasma cross-section in a tokamak and will be the central focus of our analytical and numerical exploration.

1.4.1 Plasma vertical stability

In the pursuit of improved performance, modern tokamak experiments very often consider the *magnetic divertor* configuration (Figure (1.3)) and make use plasma shaping.

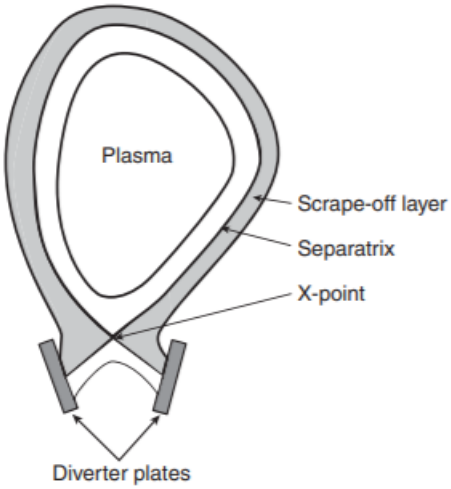

Fig. 1.3 Schematic diagram of a divertor (single null configuration),[1]

The magnetic divertor, characterized by single or double null divertor configurations with one or two magnetic X-points, confines the plasma within a last-closed-magnetic-surface. This design proves effective in managing the flux of thermal plasma directed towards the inner metallic wall of the toroidal confinement chamber, successfully addressing challenges associated with plasma-wall interactions.

Plasma shaping plays an important role by optimizing the total current carried by the plasma. This approach enhances the overall confinement performance of a tokamak experiment. On the other hand, plasma shaping, through elongating the plasma cross-section, is strongly linked with dangerous axisymmetric movements of the plasma column, referred to as vertical displacement events (VDE). The non-circular plasma cross-section renders the plasma equilibrium unstable at the Ideal MHD level, specifically against axisymmetric ($n = 0$) displacements in the vertical direction. This vertical instability manifests as a rigid shift of the entire plasma vertically, potentially leading to disruptions. In the case of an unstable VDE, the termination of the multi-Mega-Ampere plasma current occurs within a characteristic Alfven time scale $\tau_A = R_0/v_A$ (where R_0 is the toroidal major radius and v_A is the

propagation velocity of Alfven waves). Typically measured in microseconds, this termination induces dangerous electromagnetic stresses on the confinement device. Therefore, in tokamak experiments, special precautions are necessary to prevent the onset of VDEs. A conductive wall surrounding the plasma, along with specific plasma-facing components, provides a passive feedback mechanism for stabilizing the vertical instability. This measure results in the emergence of stable oscillations with a frequency close to the characteristic Alfven frequency $2\pi/\tau_A$, referred to in this work as Vertical Displacement Oscillatory Modes (VDOM). Additionally, a new instability, growing on the timescale of wall resistive diffusion, arises. Thanks to its slower growth rate, this non-rotating $n = 0$ resistive wall mode is stabilized in tokamaks through an active feedback system utilizing coils positioned outside the vacuum chamber.

1.4.2 Particle resonances

As previously mentioned, the effective confinement of energetic particles resulting from fusion reactions, such as fusion α_s with energies in the MeV range, is a critical aspect in realizing a fusion reactor. In current tokamaks, populations of energetic particles can be produced through heating techniques to explore their impact on plasma behavior. These energetic ions exhibit non-Maxwellian distributions in velocity space, being out of thermodynamic equilibrium, and serve as a free energy source that can be used to trigger various types of macroscopic instabilities.

Very often, the presence of superthermal ions in the plasma can induce instabilities through resonant interactions between these particles and the normal mode fluctuations of the thermal plasma. The resonance condition involves frequencies associated with the periodic motion of magnetically confined energetic particles matching with the frequency of oscillations of thermal plasma collective modes. Due to their high energy, energetic particles exhibit various forms of periodic motion, and each associated frequency can resonate with different normal modes. For example, the precessional motion around the torus of energetic ions has frequencies that resonate with the $n = 1, m = 1$ MHD mode, resulting in what is known as "fishbone oscillations", discussed for the first time in Ref. [7] and [8]. The periodic motion of particles in the poloidal plane, describing so-called trapped and passing orbits, presents a higher oscillation frequency compared to the precessional frequency. Resonances between this motion and MHD modes may involve modes with Alfvenic

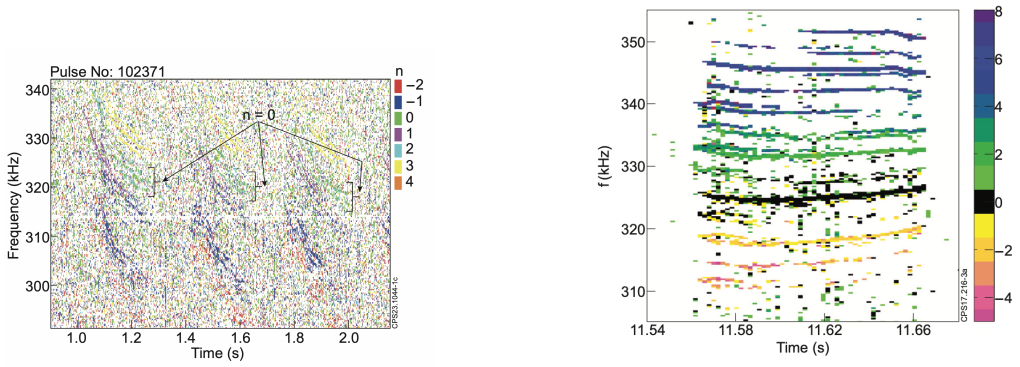

(a) (b)

Fig. 1.4 Spectrograms from different JET discharges showing n=0 modes, (a) [2] and (b) [3]

frequencies. An example of these are Toroidal Alfven Eigenmodes (TAE) [9] and Ellipticity indiced Alfvén Eigenmodes (EAE) [10], important plasma modes that are destabilized only in the presence of energetic ions.

This study focuses on the resonant interaction between the motion of energetic particles in the poloidal plane and the $n = 0$ vertical displacements. Similar to the cases of fishbones and TAE, the presence of fast ions represents a free energy source for the oscillatory mode arising from the stabilization of the vertical instability. Given suitable conditions, the wave-particle resonant interaction has the potential to destabilize the VDOM.

1.4.3 JET experimental observations

Recent experimental observations from the JET tokamak represent a partial motivation for the research outlined in this thesis. Plasma discharges featuring fast ion populations with energies extending into the MeV range exhibit the destabilization of $n = 0$ modes with Alfvénic frequency. The presence of these modes is identified through measurements of magnetic perturbations using Mirnov Coils. Figure 1.4 presents magnetic spectrograms illustrating the various modes (with different toroidal mode number) observed in the experiment.

The spectrograms reported in Fig. 1.4, refer to two similar shots in which a particular heating scheme, called third harmonic heating was employed in JET. A combination of NBI and ICRH tuned to heat the beam ions was used in order to

produce an energetic population of Deuterium with energies in the range $100\ keV - 1\ MeV$. The frequency of the $n = 0$ modes is $f_0 \sim 320 - 330 kHz$.

More recently, during the last DT3 experimental campaign, $n = 0$ modes driven by alpha particles resulting from D-T fusion reactions have been detected at a slightly lower frequency, approximately $\sim 180 kHz$. Similar types of axisymmetric Alfvénic oscillations have been observed in various tokamak experiments, such as TFTR [11] and MAST [12]. Some of these observations have been identified as Global Alfvén Eigenmodes with $n = 0$ [13]. The objective of this work is to offer a new theoretical description proposing an alternative interpretation for these observations, framing them in terms of Vertical Displacement Oscillatory Modes destabilized by fast ions.

1.5 Outline of this thesis

In this thesis, the focus is on exploring Vertical Displacement Oscillatory Modes (VDOM) in tokamak plasmas, which emerge due to the passive feedback stabilization of the ideal vertical instability. These oscillations exhibit an Alfvénic characteristic frequency, and their destabilization can occur through resonant interaction with MeV ions.

The primary aim of this study is to provide a first theoretical investigation of the VDOM. Initial insights into the main characteristics of the mode and its destabilization due to fast ion effects are highlighted using simplified models that allow for analytic treatment. More realistic conditions are then considered for numerical Magnetohydrodynamics (MHD) simulations, taking a step closer to the potential identification of these modes in present-day tokamak experiments.

The analytical depiction of the VDOM is obtained within the framework of Ideal MHD, taking into account the plasma feedback stabilization achieved with a nearby resistive wall. The analysis is further expanded to include the resonant interaction with energetic ions, employing the hybrid-kinetic MHD model. To deepen our understanding, the analytical models are complemented with numerical simulations using the NIMROD code. This transition from simplified analytical models to realistic plasma geometries and profiles is crucial for a comprehensive understanding of the mode characteristics.

The thesis is structured as follows: Chapter 2 delves into particle trajectories in tokamaks, deriving the drift kinetic equation for a comprehensive kinetic description of the plasma. In Chapter 3, the magnetohydrodynamic model is introduced, extending from ideal MHD to include kinetic effects in the hybrid kinetic MHD model. The extended energy principle is discussed for the study of plasma stability in presence of superthermal ions. The importance of the equilibrium distribution function of fast ions in stability studies is highlighted. At the end of this chapter, distributions functions considering the effect of sawtooth oscillations firstly derived by us in [14] are reported.

Chapter 4 studies the VDOM dispersion relation within the ideal MHD framework, considering a resistive wall as a passive feedback system around the plasma, following [15]. In addition to the VDOM solution, a focus on the resistive wall mode growth near marginal stability, based on [16], is presented in this chapter. Chapter 5 incorporates the kinetic effects of resonant superthermal ions using different distribution functions in the hybrid kinetic MHD model, as discussed in [17]. In Chapter 6, reporting the results of [18, 2] the simplified models from Chapters 4 and 5 are extended to realistic tokamak conditions using the NIMROD MHD code, incorporating experimental data from recent JET discharges. These last three chapters report the bulk of the original results described in this work.

Finally, Chapter 7 concludes this thesis by summarizing the key findings and contributions.

Chapter 2

Particles trajectories

To describe the mechanism behind the wave-particle interaction that induces kinetic-MHD instabilities in tokamaks, a thorough understanding of the motion exhibited by magnetically confined particles is essential. The movement of ions is entirely dictated by the magnetic configuration of the device. Therefore, we will provide a brief overview of the tokamak magnetic configuration. Three distinct frequencies associated with particle motion, corresponding to three invariants, can be identified: the cyclotron frequency linked to the particle Larmor gyration, the bounce (or passing) frequency of the particle motion in the poloidal cross-section, and the precession frequency characterizing the motion along the torus. This chapter aims to provide the description of particle trajectories using a Lagrangian formalism, particularly focusing on the Drift kinetic approximation. The subject of this chapter has been extensively covered in various books. For more detailed descriptions of the topics discussed herein, well-known publications on Plasma Physics provide valuable resources. A non-exhaustive list includes [19–21].

2.1 Particles trajectories in Tokamaks

2.1.1 Constants of motion

A straightforward method for characterizing particle motion is to examine the 6D space of positions $\mathbf{x}$ and velocities $\mathbf{v}$. Through the exploitation of system symmetries

and conserved quantities, it is possible to minimize the number of variables required to describe the particle trajectory.

In the absence wave-particle interactions or collisions, the total energy of a particle is an invariant of its equilibrium orbit when the electric field evolves on shorter timescales compared with the cyclotron motion. In the presence of a cross-field electric potential ϕ, the particle energy consists both kinetic and electrostatic potential energy. It's worth noting that for superthermal particles, the potential energy is significantly smaller than the kinetic energy, and can be neglected in certain conditions. The symmetry in the toroidal direction of the Tokamak configuration introduces one other invariant of the particle motion, the canonical toroidal angolar momentum:

$$P_\varphi = \frac{Ze}{c}\psi + mRv_\varphi. \tag{2.1}$$

Here, Ze and m represent the particle charge and mass, respectively; R is the particle major radius (detailed below); v_φ denotes its velocity in the toroidal direction, and ψ represents the poloidal magnetic flux. In addition to these two exact conserved quantities of the particle motion, different adiabatic invariants can be associated with various periodicities of the trajectory [21].

2.1.2 Gyromotion and drifts

The tokamak configuration can be characterized using this simplified model: The coordinate system considered is illustrated in Figure (2.1), where φ represents the toroidal angle, θ denotes the poloidal angle, R_0 signifies the tokamak major radius, and r indicates the distance from the magnetic axis. The major radius of the particle is $R = R_0 + r\cos(\theta)$.

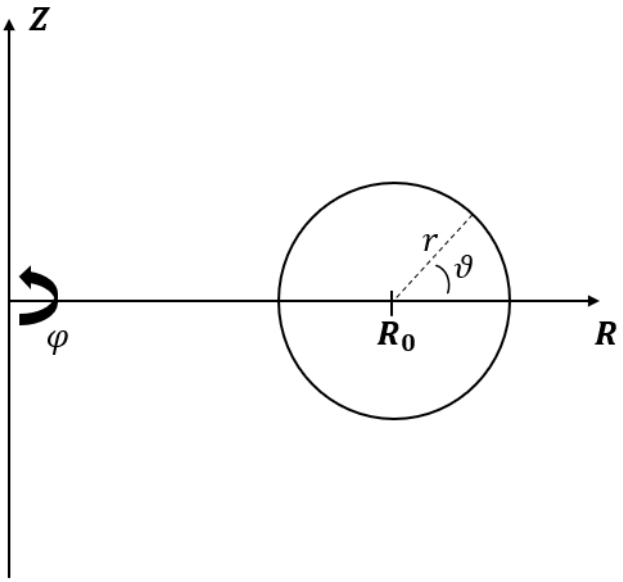

Fig. 2.1 Schematic of the toroidal coordinate system.

The magnetic field **B** is:

$$\mathbf{B}(r,\theta) = \frac{1}{h}[B_{\varphi_0}\hat{e}_\varphi + B_{\theta_0}(r)\hat{e}_\theta] \tag{2.2}$$

where B_{φ_0} and B_{θ_0} are respectively toroidal and poloidal magnetic fields and h:

$$h(r,\theta) = \frac{R}{R_0} = 1 + \varepsilon cos(\theta) \tag{2.3}$$

with aspect ratio $\varepsilon = r/R_0$.

Particles will follow the magnetic field lines, undergoing a gyrating motion with a frequency known as the *cyclotron frequency*, denoted as $\Omega_c = ZeB/cm$. This motion occurs within a radius $\rho_L = v_\perp/\Omega_c$, referred to as the Larmor radius, $v_\perp$ being the particle velocity in the plane perpendicular to the field lines. Associated with this periodic motion is an adiabatic invariant known as the particle magnetic moment, given by $\mu = mv_\perp^2/2B$. This parameter represents the magnetic dipole moment of the charged particle, akin to viewing the particle as a charged current ring with a radius ρ_L. The phenomena studied in this work involve length and time scales that are much larger than those associated with the gyromotion of particles in tokamaks, satisfying the ordering $k_\perp \rho_L \ll 1$ and $\omega/\Omega_c \ll 1$. Thus, the magnetic moment serves

as a conserved quantity of the particle motion, and in the following we will focus on the motion of the guiding center of the particle orbit.

The guiding center position experiences several drifts caused by external forces. Firstly, the presence of an electric field induces the cross-field drift, expressed as:

$$\mathbf{v}_{\mathbf{E}\times\mathbf{B}} = \frac{\mathbf{E}\times\mathbf{B}}{B^2} \tag{2.4}$$

Two additional drifts impact the guiding center trajectory: toroidal curvature and magnetic field gradient drifts:

$$\mathbf{v}_D = \mathbf{v}_\kappa + \mathbf{v}_{\nabla B} = \frac{1}{m\Omega_c}\hat{e}_\parallel \times (mv_\parallel^2\kappa + \mu\nabla B) \tag{2.5}$$

where $\hat{e}_\parallel = \mathbf{B}/B$ is the unit vector along the field lines and the field lines curvature can be defined as $\kappa = (\hat{\mathbf{e}}_\parallel \cdot \nabla)\hat{\mathbf{e}}_\parallel$. Considering a constant toroidal field B_{φ_0} dominant compared to the poloidal component ($B_{\theta_0}(r)/B_{\varphi_0} \sim \varepsilon$), the $\hat{e}_\parallel$ direction is primarily toroidal. Under these conditions, it can be demonstrated that $\mathbf{v}_D$ is mainly in the vertical direction.

2.1.3 Passing and Trapped particles

The force related to the ∇B drift is also called the mirror force and is strongly interconnected with the conservation of the magnetic moment μ. Assuming that the varying magnetic field can be expressed as $B = (B_{\varphi_0}/h)(1+\mathscr{O}(\varepsilon^2))$, it follows that a particle moving along the field line will experience a more intense magnetic field on the inside of the torus and a weaker field on the outside. This magnetic field modulation is of order ε: $B_{\max} - B_{\min} = B(\theta=\pi) - B(\theta=0) \simeq 2\varepsilon B_{\varphi_0} + \mathscr{O}(\varepsilon^2)$.

Since the magnetic moment $\mu = mv_\perp^2/2B$ is conserved, the particle velocity across the field line, $v_\perp$, must vary together with the changing magnetic field. Considering that the particle kinetic energy $E = mv^2/2$ (neglecting electric potential contributions to the kinetic energy of the particles) is conserved, it is useful to introduce a new invariant quantity of the guiding center motion of the particles, the pitch angle:

$$\Lambda = \frac{\mu B_{\varphi_0}}{E} = \frac{v_\perp^2}{v^2}h(r,\theta). \tag{2.6}$$

The pitch angle varies between $0 \leq \Lambda \leq 1+\varepsilon$, and the guiding center velocity along the field line can be rewrittend as:

$$v_{\parallel} = \pm v(1-\frac{v_{\perp}^2}{v^2})^{1/2} = \pm v(1-\frac{\Lambda}{h})^{1/2}. \tag{2.7}$$

Two principal types of particle trajectories can be identified for the guiding center motion in a tokamak:

- **Circulating (or passing) particles:** This category includes particles for which $0 \leq \Lambda \leq 1-\varepsilon$. In this regime, the guiding center motion completes a full orbit around the magnetic axis within a poloidal cross-section.
- **Trapped particles:** For particles with $1-\varepsilon \leq \Lambda \leq 1+\varepsilon$, the parallel velocity $v_{\parallel}$ changes sign during the orbit, resulting in a distinctive "banana orbit" when projected onto the poloidal plane. The trajectory reaches its maximum θ value at the bounce angle θ_b, where $v_{\parallel}(\theta_b) = 0$.

The two different orbits are sketched in Fig. 2.2.

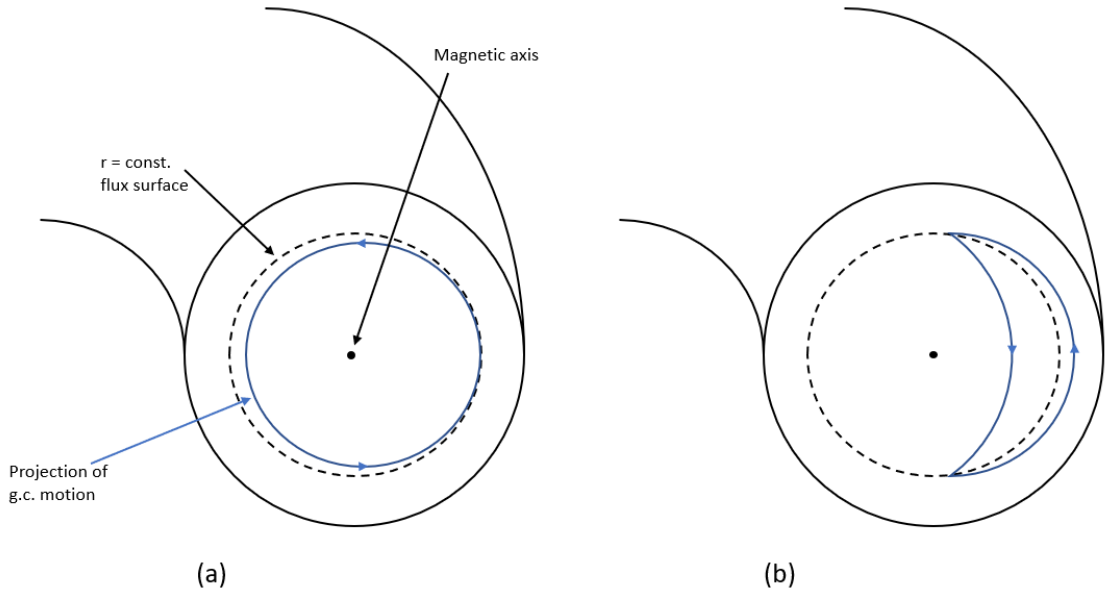

Fig. 2.2 Scheme of the projection on the poloidal cross section of particle orbits in tokamaks: passing particles (a) and trapped particles (b)

It is important to remark that the particles dominant motion is along the field lines, i.e. in the toroidal direction. The orbits depicted in Fig. 2.2 represent projections of particle motion onto the poloidal plane. Completion of these orbits may necessitate a significant number of toroidal passes.

The frequencies associated with different orbits can be obtained using the bounce-averaging formalism, as detailed below for both passing and trapped particles and discuss in further detail in [20, 22]. We assume a circular flux surfaces MHD equilibrium, and consider the guiding center's excursion from its associated flux surface to be negligible.

Passing

The characteristic time required for a passing particle to complete a closed orbit in the poloidal plane, and consequently its associated frequency, can be studied by examining its integral expression over a full orbit:

$$\tau_t = \oint d\tau \approx \oint \frac{dl}{v_\parallel}(1+\mathscr{O}(v_D/v_\parallel)). \tag{2.8}$$

To express dl, it can be rewritten as follows:

$$\frac{rd\theta}{B_\theta} = \frac{Rd\varphi}{B_\varphi} = \frac{dl}{B} \rightarrow dl = \frac{rB}{B_\theta}d\theta \approx R_0 q(r) d\theta \tag{2.9}$$

with safety factor, $q(r) = rB_\varphi/R_0B_\theta$.
When considering a small radial excursion of a guiding center orbit from a given flux surface $r = r_0$, expressed as $r(t) = r_0 + \delta r$ with $|\delta r| \ll r_0$, the function $q(r)$ approximates to nearly constant over the orbit. It follows that

$$\tau_t \approx R_0 q \oint \frac{d\theta}{v_\parallel} = \frac{R_0 q}{v}\int_0^{2\pi} \frac{d\theta}{(1-\Lambda/h)^{1/2}} \tag{2.10}$$

Defining a parameter κ:

$$\begin{aligned} \kappa^2 &= \frac{1}{2} + \frac{1}{2\varepsilon}(1-\Lambda); \\ (1-\Lambda) &= 2\varepsilon\kappa^2 - \varepsilon; \end{aligned} \tag{2.11}$$

the denominator of the integral of Eq. (2.10) can be rewritten as a function of the poloidal angle:

$$(1-\frac{\Lambda}{h}) = \frac{1}{h}(1+\varepsilon cos(\theta)-\Lambda) = \frac{(1-\Lambda+\varepsilon cos(\theta))}{1+\varepsilon cos(\theta)} \tag{2.12}$$

In the limit of deeply passing particles we consider $1-\Lambda \sim \mathscr{O}(1)$, thus $\kappa^2 \sim \mathscr{O}(1/\varepsilon)$. In this situation we obtain at zeroth order in ε:

$$\frac{(1-\Lambda+\varepsilon cos(\theta))}{1+\varepsilon cos(\theta)} = (1-\Lambda)+\mathscr{O}(\varepsilon) = 2\varepsilon\kappa^2+\mathscr{O}(\varepsilon) \tag{2.13}$$

With Eq. 2.13 the transit time integral is straightforward and reads:

$$\tau_t = \frac{R_0 q}{v}\frac{1}{(2\varepsilon\kappa^2)^{1/2}}\int_0^{2\pi} d\theta = \sqrt{2}\frac{R_0 q}{v\sqrt{\varepsilon}}\frac{\pi}{\kappa} \tag{2.14}$$

Approaching instead the passing-trapped limit, $1-\Lambda$ is of order $\mathscr{O}(\varepsilon)$ and $\kappa^2 \sim \mathscr{O}(1)$, therefore we can approximate:

$$\begin{aligned}
&\frac{(1-\Lambda+\varepsilon cos(\theta))}{1+\varepsilon cos(\theta)} = (1-\Lambda+\varepsilon cos(\theta))+\mathscr{O}(\varepsilon^2) \\
&\approx (2\varepsilon\kappa^2-\varepsilon+\varepsilon cos(\theta)) = 2\varepsilon\kappa^2\left(1-\frac{1}{\kappa^2}\frac{1-cos(\theta)}{2}\right) \\
&= 2\varepsilon\kappa^2\left(1-\frac{1}{\kappa^2}sin^2(\theta/2)\right)
\end{aligned} \tag{2.15}$$

Substituting Eq. (2.15) back into Eq. (2.10), the transit time can be written as:

$$\tau_t = \frac{R_0 q}{v}\int_0^{2\pi}\frac{d\theta}{(1-\Lambda/h)^{1/2}} = \frac{R_0 q}{v}\frac{1}{(2\varepsilon)^{1/2}\kappa}\int_0^{2\pi}\frac{d\theta}{\left(1-\frac{1}{\kappa^2}sin^2(\theta/2)\right)^{1/2}} \tag{2.16}$$

Then, changing integration variable $\theta = 2\phi$, $d\theta = 2d\phi$:

$$\tau_t = \frac{R_0 q}{v}\frac{1}{(2\varepsilon)^{1/2}\kappa}2\int_0^{\pi}\frac{d\phi}{\left(1-\frac{1}{\kappa^2}sin^2(\phi)\right)} = 2\sqrt{2}\frac{R_0 q}{v\sqrt{\varepsilon}}\frac{\mathscr{K}(1/\kappa^2)}{\kappa} \tag{2.17}$$

Here, $\mathscr{K}(x)$ denotes the "complete elliptic integral of the first kind". The limit of Eq. 2.17 for $\kappa \gg 1$, coincides with the result of Eq. 2.14 obtained in the deeply

passing limit. The two results thus match at the zeroth order in ε for $1 \gg 1-\Lambda \gg \varepsilon$. In the following we will thus consider the transit time described by Eq. 2.17 at the zeroth order in ε. A more rigorous derivation for arbitrary order in ε can be found in the recent work by Stephens et al. [22] that agrees with our expression in the small ε limit. The transit frequency can thus be defined as:

$$\omega_t = \frac{2\pi}{\tau_t} = \frac{\pi}{\sqrt{2}} \frac{v\sqrt{\varepsilon}}{R_0 q} \frac{\kappa}{\mathscr{K}(1/\kappa^2)} \tag{2.18}$$

Trapped

Similarly to what we described for passing particles, the characteristic time required for a trapped particle to complete a closed banana orbit in the poloidal plane is obtained from its integral expression over a full orbit. Assuming again small radial excursion of the particle orbits from the flux surfaces, the bounce time can be written as:

$$\tau_b \approx R_0 q \oint \frac{d\theta}{v_\parallel} = \frac{4R_0 q}{v} \int_0^{\theta_b} \frac{d\theta}{(1-\Lambda/h)^{1/2}} \tag{2.19}$$

where θ_b is the bounce angle associated with the sign change of $v_\parallel$. From Eq. (2.7) one obtains, to first order in ε, that $(\Lambda-1)/\varepsilon = \cos(\theta_b)$, and with the definition of κ in Eq. (2.11):

$$\kappa^2 = \frac{1-\cos(\theta_b)}{2} = \sin^2(\theta_b/2) \tag{2.20}$$

We then introduce a new variable ζ defined through:

$$\sin(\theta/2) = \kappa \sin(\zeta) \tag{2.21}$$

The denominator of Eq. (2.19) can be rewritten as a function of ζ:

$$\begin{aligned}(1-\frac{\Lambda}{h}) &= \frac{1}{h}(1+\varepsilon cos(\theta)-\Lambda) = \varepsilon(2\kappa^2-1+cos(\theta)) + \mathscr{O}(\varepsilon^2) \\ &\approx 2\varepsilon(\kappa^2 - \frac{cos(\theta)-1}{2}) = 2\varepsilon(\kappa^2 - \sin(\theta/2)^2) = 2\varepsilon(\kappa^2 - \kappa^2\sin(\zeta)^2) \\ &= 2\varepsilon\kappa^2\cos^2(\zeta)\end{aligned} \tag{2.22}$$

Substituting in the integral expression, and changing the integration variable, we obtain:

$$\tau_b = \frac{4R_0q}{v}\int_0^{\pi/2}\frac{1}{\sqrt{2\varepsilon}\kappa\cos(\zeta)}\frac{2\kappa\cos(\zeta)d\zeta}{\sqrt{1-\kappa^2\sin^2(\zeta)}} = \frac{4\sqrt{2}R_0q}{v\sqrt{\varepsilon}}\mathscr{K}(\kappa^2) \tag{2.23}$$

The bounce frequency then reads:

$$\omega_b = \frac{2\pi}{\tau_b} = \frac{\pi}{2\sqrt{2}}\frac{v\sqrt{\varepsilon}}{R_0q}\frac{1}{\mathscr{K}(\kappa^2)} \tag{2.24}$$

In tokamak plasmas, the frequencies associated with the orbits discussed above are significantly smaller compared to the cyclotron frequency for both thermal plasma particles and fast ions ($\Omega_c \gg \omega_t, \omega_b$). In the following chapters, the analysis will focus on this periodic motion of the fast ions in the poloidal plane. For superthermal particles the bounce and transit frequencies can be comparable with the frequecy of Alvénic modes $\omega_t, \omega_b \sim \omega_A = 2\pi/\tau_A$, leading to wave-particle resonances. As for the case of the gyromotion, associated with the periodic motion of the guiding center in the poloidal plane it is possible to identify the second adiabatic invariant:

$$J_l = \oint v_\parallel dl. \tag{2.25}$$

where the integration is over a complete bounce/passing orbit.

The final periodic motion exhibited by particles within a tokamak magnetic configuration is the toroidal precession. This motion is primarily linked to the cross-field drift, causing particles to deviate from their reference magnetic surface and inducing a precessional motion of the particle orbits in the toroidal direction. An estimate for the frequency at which a banana orbit completes a toroidal revolution, i.e., its precession frequency, is:

$$\omega_D = \frac{qv_\perp^2}{2\Omega_c r R_0}\left(\frac{2\mathscr{E}(\kappa^2)}{\mathscr{K}(\kappa^2)} - 1\right) \tag{2.26}$$

where κ is defined in Eq. (2.11).

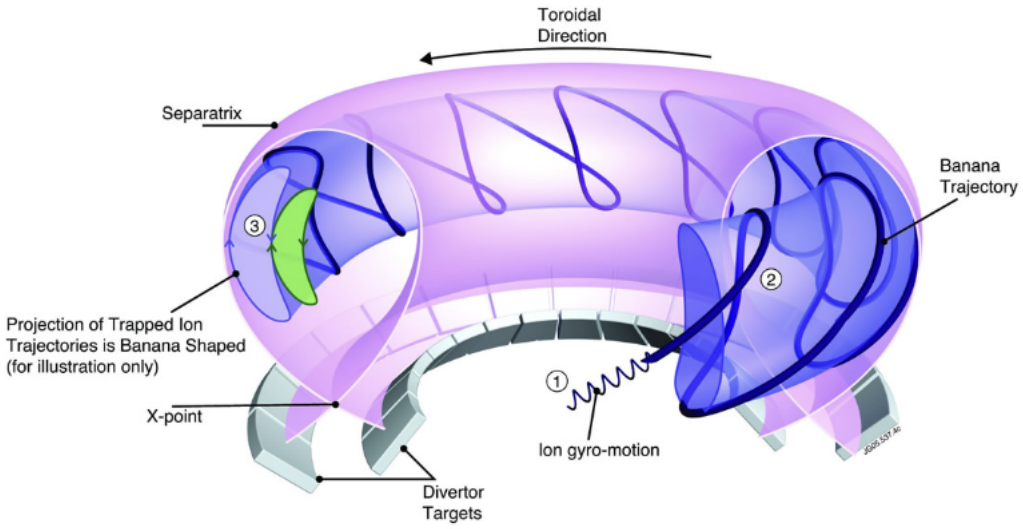

Fig. 2.3

The toroidal precession motion typically exhibits the slowest frequency, and in standard conditions, $\Omega_c \gg \omega_{b,t} \gg \omega_D$ is satisfied. Similar to previous cases, this periodic motion is linked to an adiabatic invariant of particle motion. The third adiabatic invariant is the magnetic flux enclosed by the precessional drift orbit:

$$\Phi = \oint v_D dl. \tag{2.27}$$

where the integral is over a full precessional orbit of the center of a banana motion. The full particle motion in the tokamak configuration, exhibithing the three periodicities, is displayed in Fig. 2.3.

The conservation of adiabatic invariants of the particle motion has strong implications on the properties and behaviour of a plasma. As we briefly mentioned, the conservation of the magnetic moment is related to the magnetic mirror force. Several designs and experiments tried to exploit the mirror confinement in magnetic configurations with open field lines in the past. The conservation of the second and third adiabatic invariants strongly impacts the stability of tokamak plasmas [23, 24]. However, a crucial reminder is necessary: the adiabatic invariants are not rigorous conserved quantities of the particle motion. The theory of adiabatic invariants, well established within classical mechanics, is discussed extensively for plasma physics in

the work by Northrop [25], and briefly in a more recent publication from Heidbrink and White [26].

It is possible to summarize the conditions required to ensure the conservation of an adiabatic invariant:

- Small orbit variations within the timescale of the periodic motion.
- Perturbations must not resonate with the motion periodicity.
- Small perturbations

These schematic conditions clearly illustrate that the conservation of adiabatic invariants is linked to the phenomena under investigation, rather than the particle motion itself.

As previously mentioned, in this work we focus our attention on MHD modes with timescales on the order of the Alfvén time, τ_A, which may resonate with the periodic orbits of fast ions in the poloidal plane, $\omega_{b,t}$. The magnetic moment can be safely considered a constant of particle motion, as briefly discussed in Sec. 2.1.2. However, for the specific problem addressed in this work, the other two adiabatic invariants are not conserved. Thus, the particle motion can be characterized by considering the conservation of total energy E, canonical toroidal momentum P_φ, and magnetic moment μ.

2.2 Drift kinetics

In this section, our focus shifts to a more detailed description of the motion of superthermal particles, that requires a kinetic model. The perturbations of interest satisfy the ordering $k_\perp \rho_h \ll 1$ and $\omega/\Omega_h \ll 1$, where ρ_h and Ω_h represent the Larmor radius and cyclotron frequency of energetic particles, respectively. The guiding center velocity correct to first order in $\delta = \rho/R_0 \ll 1$ (dropping the subscript h for Ω and ρ) is :

$$\dot{\mathbf{R}} = v_\parallel \hat{e}_\parallel + \frac{1}{m\Omega}\hat{e}_\parallel \times (\mu \nabla B + m v_\parallel^2 \boldsymbol{\kappa} - Ze\mathbf{E}) = v_\parallel \hat{e}_\parallel + \mathbf{v}_D + \mathbf{v}_{\mathbf{E}\times\mathbf{B}} \tag{2.28}$$

where $\mathbf{R}$ denotes the guiding center position, the overdot indicates the time derivative. The different drifts of the particle motion discussed in Sec. 2.1.2 are assumed to be

of the same order of magnitude. The $\mathbf{E}\times\mathbf{B}$ drift is comparable to the grad B and curvature drift if $E/B = \mathscr{O}(\delta)$. Therefore, $\mathbf{v}_D \sim \mathbf{v}_{\mathbf{E}\times\mathbf{B}} = \mathscr{O}(\delta)$ while $v_\parallel \hat{e}_\parallel = \mathscr{O}(1)$. Terms of order $\mathscr{O}(\delta^2)$ have been neglected, including additional particles drifts such as the so-called polarization drift and the drift $(v_\parallel/\Omega)\hat{e}_\parallel \times (\partial \hat{e}_\parallel)/\partial t$.
The particle acceleration in the parallel direction, correct to order δ, is

$$m\dot{v}_\parallel = -\mu \hat{e}_\parallel \cdot \nabla B + Ze\hat{e}_\parallel \cdot \mathbf{E} + mv_\parallel \kappa \cdot \dot{\mathbf{R}} \tag{2.29}$$

The equation of motion detailed above can be obtained through a Lagrangian formulation of the guiding center motion described by Littlejohn in Ref. [27]:

$$\mathscr{L} = \left(\frac{Ze}{c}\mathbf{A} + mv_\parallel \hat{e}_\parallel\right) \cdot \dot{\mathbf{R}} + \frac{1}{\Omega} y\dot{\alpha} - \frac{1}{2}mv_\parallel^2 - y - Ze\phi \tag{2.30}$$

Here, $\mathbf{A}$ and ϕ denote electromagnetic potentials, $y = \mu B = mv_\perp/2$ represents the *perpendicular energy* and α is the gyroangle in the velocity space. This Lagrangian is a function of the 6 variables:

$$\mathscr{L} = \mathscr{L}(\mathbf{R}, v_\parallel, y, \alpha; \dot{\mathbf{R}}, \dot{v}_\parallel, \dot{y}, \dot{\alpha}; t) \tag{2.31}$$

in which α, $\dot{v}_\parallel$ and $\dot{y}$ do not appear. Equations (2.28-2.29) can be easily obtained from the Euler-Lagrange equations correct to order δ

$$\frac{d}{dt}\left(\frac{\partial \mathscr{L}}{\partial \dot{q}_i}\right) = \frac{\partial \mathscr{L}}{\partial q_i} \tag{2.32}$$

with q_i, $i \in 1;6$ being the Lagrangian variables. The following relations, showing the conservation of the magnetic moment, and defining the cyclotron frequency, are derived form the Euler Lagrange equations:

$$\frac{d}{dt}\left(\frac{\partial \mathscr{L}}{\partial \dot{\alpha}}\right) = \frac{\partial \mathscr{L}}{\partial \alpha} = 0 \rightarrow \frac{d}{dt}\left(\frac{y}{B}\right) = \frac{d\mu}{dt} = 0 \tag{2.33}$$

$$\frac{d}{dt}\left(\frac{\partial \mathscr{L}}{\partial \dot{y}}\right) = \frac{\partial \mathscr{L}}{\partial y} = 0 \rightarrow \dot{\alpha} = \Omega \tag{2.34}$$

Within this Lagrangian formalism, it is possible to write the collisionless Vlasov equation describing the evolution of the particle distribution function:

$$\frac{\partial f}{\partial t} + \sum_{i=1}^{6} \dot{q}_i \frac{\partial f}{\partial q_i} = 0 \tag{2.35}$$

$$\rightarrow \frac{\partial f}{\partial t} + \dot{\mathbf{R}} \cdot \nabla f + \dot{v}_{\parallel} \frac{\partial f}{\partial v_{\parallel}} + \dot{y} \frac{\partial f}{\partial y} + \dot{\alpha} \frac{\partial f}{\partial \alpha} = 0 \tag{2.36}$$

where f is the distribution function in terms of the Lagrangian variables: $f = f(\mathbf{R}, v_{\parallel}, y, \alpha; t)$. By inspection, the term with $\partial f / \partial \alpha$ is multiplied by Ω, and is the largest. Setting $f = f_0 + f_1 + ...$ with $f_1 / f_0 = \mathscr{O}(\delta)$, by comparison with the other leading order terms, it is possible to show that

$$\dot{\alpha} \frac{\partial f_0}{\partial \alpha} = 0 \tag{2.37}$$

meaning that f_0 is independent of α. Thus, to first order:

$$\frac{\partial f_0}{\partial t} + \dot{\mathbf{R}} \cdot \nabla f_0 + \dot{v}_{\parallel} \frac{\partial f_0}{\partial v_{\parallel}} + \dot{y} \frac{\partial f_0}{\partial y} + \dot{\alpha} \frac{\partial f_1}{\partial \alpha} = 0 \tag{2.38}$$

The last term can be eliminated considering the average over the gyroangle, $\oint d\alpha \dot{\alpha} \partial f_1 / \partial \alpha = 0$. The other terms $\dot{\mathbf{R}}$, $\dot{v}_{\parallel}$, and $\dot{y}$ do not depend on α to first order in δ, and the α-average is trivial. In this way, one obtains the *collisionless drift-kinetic equation*:

$$\frac{\partial f_0}{\partial t} + \dot{\mathbf{R}} \cdot \nabla f_0 + \dot{v}_{\parallel} \frac{\partial f_0}{\partial v_{\parallel}} + \dot{y} \frac{\partial f_0}{\partial y} = 0 \tag{2.39}$$

the subscript "0" will be dropped in the following. At equilibrium, $\partial / \partial t = 0$, the distribution function can be described using the invariant of the motions described in Sec. 2.1.

$$F = F(E, \mu, P_{\varphi}; \sigma) \tag{2.40}$$

with the total energy of the particle E, canonical toroidal momentum P_φ and magnetic moment μ rewritten in terms of the Lagrangian variables:

$$E = \frac{1}{2} m v_\parallel^2 + y + Ze\phi(\mathbf{R}) \tag{2.41}$$

$$\mu = \frac{y}{B(\mathbf{R})} \tag{2.42}$$

$$P_\varphi = \frac{\partial \mathscr{L}}{\partial \dot{\varphi}} = \frac{Ze}{c}\psi + mRv_\parallel \frac{B_\varphi}{B} \tag{2.43}$$

An orbit is uniquely determined by choosing the three invariants. However, an additional index, denoted as σ, is required to distinguish between co- and counter-particles. These particles share the same orbit but have opposite sign for $v_\parallel$.

2.2.1 The linearized drift-kinetic equation

Introducing a perturbation to the system and denoting perturbed quantities with the subscript "(1)", the distribution function can be expressed as $f = F + f^{(1)}$. The linearized form of the drift-kinetic equation is then given by:

$$\frac{df^{(1)}}{dt} + \dot{\mathbf{R}}^{(1)} \cdot \nabla F + \dot{v}_\parallel^{(1)} \frac{\partial F}{\partial v_\parallel} + \dot{y}^{(1)} \frac{\partial F}{\partial y} = 0 \tag{2.44}$$

This can be reformulated by considering the equilibrium dependence on the invariants of Eqs. 2.41-2.43:

$$\begin{aligned} &\frac{df^{(1)}}{dt} + \left(\dot{\mathbf{R}} \cdot \nabla P_\varphi + \dot{v}_\parallel^{(1)} \frac{\partial P_\varphi}{\partial v_\parallel} \right) \frac{\partial F}{\partial P_\varphi} + \left(Ze\dot{\mathbf{R}}^{(1)} \cdot \nabla \phi + \right. \\ &\left. + m v_\parallel \dot{v}_\parallel^{(1)} + y^{(1)} \right) \frac{\partial F}{\partial E} + \left(\frac{\dot{y}^{(1)}}{B} - \frac{y}{B} \dot{\mathbf{R}}^{(1)} \cdot \nabla B \right) \frac{\partial F}{\partial \mu} = 0 \end{aligned} \tag{2.45}$$

The terms multiplying each derivative of the equilibrium distribution function can be rewritten in terms of the perturbed Lagrangian of the particle motion, leading to:

$$\frac{df^{(1)}}{dt}+\left(\frac{\partial\mathscr{L}^{(1)}}{\partial\varphi}-\frac{d}{dt}P_{\varphi}^{(1)}\right)\frac{\partial F}{\partial P_{\varphi}}- \\ -\left(\frac{\partial\mathscr{L}^{(1)}}{\partial t}+Ze\frac{d\phi^{(1)}}{dt}\right)\frac{\partial F}{\partial E}+\mu\left(\frac{d}{dt}\frac{B^{(1)}}{B}\right)\frac{\partial F}{\partial\mu}=0 \tag{2.46}$$

We define $h^{(1)}$ as the so-called "nonadiabatic part" of the perturbed distribution function $f^{(1)}$, such that it satisfies:

$$\frac{dh^{(1)}}{dt}=\frac{\partial F}{\partial E}\frac{\partial\mathscr{L}^{(1)}}{\partial t}-\frac{\partial F}{\partial P_{\varphi}}\frac{\partial\mathscr{L}^{(1)}}{\partial\varphi} \tag{2.47}$$

The perturbed distribution function can be obtained integrating in time as:

$$f^{(1)}=P_{\varphi}^{(1)}\frac{\partial F}{\partial P_{\varphi}}+Ze\phi^{(1)}\frac{\partial F}{\partial E}-\mu\frac{B^{(1)}}{B}\frac{\partial F}{\partial\mu}+h^{(1)} \tag{2.48}$$

The perturbed Lagrangian to leading order in δ is:

$$\mathscr{L}^{(1)}=\frac{Ze}{c}\mathbf{A}^{(1)}\cdot\dot{\mathbf{R}}-Ze\phi^{(1)}-\mu B^{(1)}+\mathscr{O}(\delta) \tag{2.49}$$

Higher order terms in delta would lead correction of at least $\mathscr{O}(\delta^2)$ corrections in Eq. (2.48). This form of the perturbed Lagrangian can be utilized to solve for $h^{(1)}$ in Eq. (2.47). The coordinate system $\mathbf{R}=(\psi,\theta,\varphi)$ is introduced, where ψ labels the equilibrium magnetic surfaces, θ is a generalized poloidal angle and φ is the previously defined toroidal angle. Exploiting the toroidal symmetry of the system, the perturbed Lagrangian is assumed to take the form:

$$\mathscr{L}^{(1)}(\mathbf{R},t)=\hat{\mathscr{L}}^{(1)}(\psi,\theta)exp(-i\omega t-in\varphi) \tag{2.50}$$

where n is the toroidal mode number. Equation (2.47) can be recast as:

$$\frac{dh^{(1)}}{dt}=-i(\omega-n\omega_{*})\frac{\partial F}{\partial E}\mathscr{L}^{(1)} \tag{2.51}$$

with ω_* being a constant of the unperturbed particle motion defined as $(\partial F/\partial P_\varphi)/(\partial F/\partial E)$. The formal solution of Eq. (2.51) is

$$h^{(1)} = -i(\omega - n\omega_*)\frac{\partial F}{\partial E}\int_{-\infty}^{t} \mathscr{L}^{(1)}(\tau)d\tau \tag{2.52}$$

where the lower limit of integration is set according to the causality prescription and $\mathscr{L}^{(1)}(\tau) = \hat{\mathscr{L}}^{(1)}(\psi(\tau),\theta(\tau))exp(-i\omega\tau - in\varphi(\tau))$. The particle position in (ψ,θ,φ) coordinates depends on τ through the guiding center equations:

$$\dot{\psi} = \dot{\mathbf{R}}\cdot\nabla\psi, \quad \dot{\theta} = \dot{\mathbf{R}}\cdot\nabla\theta, \quad \dot{\varphi} = \dot{\mathbf{R}}\cdot\nabla\varphi \tag{2.53}$$

with $\dot{\mathbf{R}}$ given in Eq. (2.28). It is possible to decompose $\varphi(\tau)$ into its secular and oscillating components:

$$\varphi(\tau) = \langle\dot{\varphi}\rangle\tau + \tilde{\varphi}(\tau) \tag{2.54}$$

Here, the brackets $\langle\cdot\rangle$ denote the average over a complete orbit in the poloidal cross section, which can be either mirror-trapped or passing for energetic particles. Bounce and transit times are defined in Sec. 2.1.3, together with the bounce average procedure used for orbit averaged quantities:

$$\langle A\rangle = \frac{1}{\tau_{b/t}}\oint A d\tau \tag{2.55}$$

The quantity $\tilde{\mathscr{L}}^{(1)} = \hat{\mathscr{L}}^{(1)}exp(-in\tilde{\varphi})$ is a periodic function of τ that can be expanded in Fourier series:

$$\tilde{\mathscr{L}}^{(1)}(\tau) = \sum_{-\infty}^{\infty}{}_p\Upsilon_p(E,\mu,P_\varphi;\sigma)exp(-ip\omega_{b,t}\tau). \tag{2.56}$$

The Fourier coefficients are defined as

$$\Upsilon_p(E,\mu,P_\varphi;\sigma) = \oint\frac{d\tau}{\tau_{b/t}}\tilde{\mathscr{L}}^{(1)}exp(ip\omega_{b,t}\tau) \tag{2.57}$$

The "nonadiabatic" part of the distribution function of Eq. (2.52) can be rewritten considering the Fourier expansion of the perturbed Lagrangian over the particle

periodicity:

$$h^{(1)} = -i(\omega - n\omega_*)\frac{\partial F}{\partial E}\sum_{-\infty}^{\infty}{}_p \Upsilon_p \int_{-\infty}^{t} exp[-i(\omega + n\langle\dot{\varphi}\rangle + p\omega_{b,t})\tau] = \tag{2.58}$$

$$= (\omega - n\omega_*)\frac{\partial F}{\partial E}\sum_{-\infty}^{\infty}{}_p \Upsilon_p \frac{exp[-i(\omega + n\langle\dot{\varphi}\rangle + p\omega_{b,t})\tau]}{\omega + n\langle\dot{\varphi}\rangle + p\omega_{b,t}} \tag{2.59}$$

The significant impact of the "nonadiabatic" component, $h^{(1)}$, in the perturbed distribution function $f^{(1)}$ is evident in the explicit appearance of the *resonant denominator* in Eq. (2.59), leading to the mode-particle resonance condition. This denominator vanishes for different p harmonics satisfying the condition:

$$\omega + n\langle\dot{\varphi}\rangle + p\omega_{b,t} = 0, \quad p = 0, \pm 1, \pm 2, ... \tag{2.60}$$

The perturbation under consideration for this study is axisymmetric, meaning it has a toroidal mode number $n = 0$. In this specific scenario, the resonant condition becomes even simpler and reduces to:

$$\omega + p\omega_{b,t} = 0, \quad p = 0, \pm 1, \pm 2, ... \tag{2.61}$$

Hence, the periodic motion of energetic particles in the poloidal cross-section, whether in a passing orbit or a trapped orbit, is the crucial motion that can be resonant with $n = 0$ axisymmetric modes.

2.3 Concluding remarks

This chapter has provided a detailed account of particle trajectories within the tokamak configuration. The characterization of the guiding center motion of particles has been considered to derive the collisionless drift-kinetic equation through a Lagrangian formalism. This comprehensive kinetic description of the plasma will serve as a crucial foundation for subsequent chapters.

Chapter 3

Ideal and hybrid kinetic MHD models

A plasma, a complex system comprised of a vast number of ionized particles, exhibits long-range electromagnetic interactions. Unlike systems dominated by nearest-neighbor collisions, the behavior of a plasma is characterized by the influence of macroscopic electric and magnetic fields. In tokamak plasmas, these *collective phenomena* have the potential to perturb the equilibrium magnetic configuration, giving rise to large-scale instabilities that impact significant portions of the plasma column. To describe these instabilities, it is not necessary to delve into the detailed description of the local single-particle motion outlined in Ch. 2. Instead, the plasma behaviour can be effectively characterized by a fluid formalism known as *Magneto-Hydro-Dynamics* (MHD). Analogous to a fluid description using the Navier-Stokes equations, MHD theory treats the plasma as a fluid composed of charged particles. This fluid can interact with external electromagnetic fields and, in turn, generate electromagnetic perturbations through the motion of charged particles. However, the fluid formalism is not suitable for studying plasma behavior in the presence of superthermal particles. A detailed kinetic treatment is required in order to describe the effect of fast ions in the plasma. In this chapter, we will introduce the hybrid kinetic MHD model that will be employed in the subsequent chapters. The derivation and study of MHD theory

3.1 Magneto-Hydro-Dynamics

The MHD model represents the plasma as a continuous fluid rather than a collection of individual particles. While this model is simple enough to be exactly solved in certain cases of interest, it lacks the level of detail needed to describe some physical phenomena accurately. The Ideal MHD model, in particular, is the simplest fluid model for a plasma. Despite its simplicity, it allows for the study of the impact of the magnetic configuration on the plasma's equilibrium and stability. However, limitations arise when attempting to explore a wide range of physical phenomena with this model, as for example superthermal particles effects. The starting point of the Ideal MHD model derivation is the complete mathematical description of a plasma in terms of the kinetic Boltzmann equation coupled with Maxewell's equations:

$$\frac{\partial f_j}{\partial t} + \mathbf{v}\cdot\nabla f_j + \frac{q_j}{m_j}(\mathbf{E} + \frac{1}{c}\mathbf{v}\times\mathbf{B})\cdot\frac{\partial f_j}{\partial \mathbf{v}} = \left(\frac{\partial f_j}{\partial t}\right)_{coll} \tag{3.1}$$

where $f_j(\mathbf{r},\mathbf{v},t)$ is the distribution function of the j species (j = electrons, ions, ...) and $(\partial f_j/\partial t)_{coll}$ is the collisions term. To derive the fluid description of the plasma, we consider the moments of the Boltzmann equation ($\{B.e.\}_j$) to transition from a microscopic to a macroscopic description:

$$0^{th}\text{ moment} \rightarrow \sum_j m_j \int d^3v \{B.e.\}_j \rightarrow \frac{\partial \rho_m}{\partial t} + \nabla\cdot(\rho_m \mathbf{u}) \tag{3.2}$$

$$1^{st}\text{ moment} \rightarrow \sum_j m_j \int d^3v \mathbf{v}\{B.e.\}_j \rightarrow \rho_m \frac{d\mathbf{u}}{dt} = -\nabla\cdot\overline{\mathbf{P}} + \frac{1}{c}\mathbf{J}\times\mathbf{B} \tag{3.3}$$

$$2^{nd}\text{ moment} \rightarrow \sum_j \frac{1}{2} m_j \int d^3v v^2 \{B.e.\}_j \rightarrow \frac{d}{dt}\left(\frac{p}{\rho_m^{\Gamma}}\right) = \textit{heat flux/pressure tensor} \tag{3.4}$$

These equations now depend on the fluid variables: mass density ρ, fluid velocity $\mathbf{u}$ and pressure tensor $\overline{\mathbf{P}}$, along with the plasma current density $\mathbf{J}$. As is standard for fluid models, the equations derived from the moments of the distribution function will always depend on a higher-order moment term. Combining these moment equations with Maxwell's equations for the electromagnetic fields still results in an incomplete set of equations. A fluid closure is needed.

3.1.1 Fluid closure

A fluid closure is a local relation, connecting moments of the distribution such as ρ_m, $\mathbf{u}$, and $\overline{\mathbf{P}}$. The validity of a fluid closure relies on certain conditions: firstly, the dimension l of fluid elements must be small compared to other relevant length scales, i.e., $l \ll L$ (where L is the macroscopic length of the system) and $l \ll \lambda$ (where λ is a generic wavelength of the system). Additionally, fluid elements must maintain their coherence for times much longer than relevant time scales. In a neutral gas described by fluid dynamics, collisions play a crucial role in ensuring the coherence of fluid elements. Gas particles tend to stick together due to collisions with neighbors, and their motion can be represented as the superposition of local mass motion along with an isotropic distribution of velocities. By connecting $\mathbf{u}$ with the physical interpretation of fluid element velocity and reducing $\overline{\mathbf{P}}$ to a scalar pressure p, the continuity equation and the momentum equation for a simple gas involve the unknowns $\rho_m, \mathbf{u}$, and p. To close the fluid model and make the system solvable, a third equation of state is needed to establish the connection between $\rho_m, \mathbf{u}$, and p. The description of collisions in terms of the collisional mean-free-path λ_{mfp} and the collisional time τ_{coll} allows for a collisional fluid closure. It becomes feasible by choosing the size of the fluid element l such that $\lambda_{mfp} \ll l \ll L$, while satisfying conditions $k\lambda_{mfp} \ll 1$ and $\omega\tau_{coll} \gg 1$.

In fusion plasmas, collisions are infrequent. The relevant time scale for ideal MHD phenomena is the Alfvén time τ_A, typically in the order of microseconds, and the typical value of τ_{coll} is around 10^{-4} seconds. The mean free path is of the order of $10^2/10^3 m$ while phenomena that can be studied with MHD have much smaller characteristic wavelengths of the order of $10m$. This implies that collisions cannot ensure the coherence of the fluid element, as ideal MHD effects happen on much faster time scales and on much smaller length scales. Therefore, alternative mechanisms must be considered and the concept of fluid elements becomes weaker in this context. The definition of fluid elements in the plane perpendicular to the magnetic field can be ensured when the Larmor radius ρ_L is sufficiently small. In this scenario, Larmor orbits serve as fundamental "quasi-particles" in the system. In the direction parallel to the field lines, however, there is no general argument to define a fluid element. In general, the MHD validity is considered as a low-frequency, long-wavelenght limit of the Vlasov description of a plasma, obtained through the moments of the Boltzmann equation [1].

In axisymmetric systems like tokamaks, on the other hand, the periodicity in the toroidal direction can be used as an argument for the fluid closure of the system. Considering the moments of the Boltzmann equation in the perpendicular and parallel directions, one obtains evolution equations for the perpendicular and parallel pressures. Two equations of state are required. Neglecting both heat fluxes, the so-called CGL, or double-adiabatic, closure for a magnetized plasma is obtained [28]. Assuming a diagonal pressure tensor:

$$\overline{\mathbf{P}} = p_\perp \bar{\mathbf{I}} + (p_\parallel - p_\perp)\hat{e_\parallel}\hat{e_\parallel} \tag{3.5}$$

and equation of state:

$$\frac{d}{dt}\left(\frac{p_\perp}{\rho_m B}\right) = 0, \quad \frac{d}{dt}\left(\frac{p_\parallel B^2}{\rho_m^3}\right) = 0 \tag{3.6}$$

The Ideal MHD closure is a particular case of CGL closure with $p_\perp = p_\parallel = p$, reducing thus the pressure to a scalar quantity:

$$\overline{\mathbf{P}} = p\bar{\mathbf{I}} \rightarrow \rho_m \frac{d\mathbf{u}}{dt} = -\nabla p + \frac{1}{c}\mathbf{J}\times\mathbf{B} \tag{3.7}$$

The heat fluxes in the second moment equation are neglected, truncating the dependence on higher-order moments, assuming an adiabatic equation of state:

$$\frac{d}{dt}\left(\frac{p}{\rho_m^\Gamma}\right) = 0, \quad \Gamma = 5/3 \tag{3.8}$$

that can be recovered from Eqs. (3.6)

Maxwell's equations are considered for the description of magnetic field **B**, electric field **E**, and current density **J**. The Ideal MHD approximation involves neglecting the displacement current in Faraday's law and assuming ideal Ohm's law. This treatment characterizes the plasma as a perfect conductor, justifying the term "ideal". In tokamak plasmas, where the ideal MHD time scale dominates resistive diffusive time, this assumption is generally valid. However, the model can be extended to account for resistivity in Ohm's law, leading to the *resistive MHD* model, in scenarios where resistivity becomes significant. The following set of

equations represents the Ideal MHD model (in c.g.s. units):

$$\frac{\partial \rho}{\partial t} + \nabla \cdot (\rho \mathbf{u}) = 0 \tag{3.9}$$

$$\rho \frac{d\mathbf{u}}{dt} = \frac{1}{c}\mathbf{J} \times \mathbf{B} - \nabla p \tag{3.10}$$

$$\frac{d}{dt}\left(\frac{p}{\rho^{\Gamma}}\right) = 0 \tag{3.11}$$

$$\nabla \times \mathbf{E} = -\frac{1}{c}\frac{\partial \mathbf{B}}{\partial t} \tag{3.12}$$

$$\nabla \times \mathbf{B} = \frac{4\pi}{c}\mathbf{J} \tag{3.13}$$

$$\mathbf{E} + \frac{1}{c}\mathbf{u} \times \mathbf{B} = 0 \tag{3.14}$$

where $d/dt = \partial/\partial t + \mathbf{u} \cdot \nabla$ is the convective (or material) derivative following the fluid elements. The mass equation in the MHD framework represents the conservation of mass in the plasma, neglecting phenomena such as mass injection via gas puffing, pellets or neutral beams or fuel depletion due to nuclear reactions. The momentum equation accounts for the interaction of three forces: the pressure gradient ∇p, the Lorentz force $\mathbf{J} \times \mathbf{B}$ and the inertial force $\rho d\mathbf{v}/dt$. In static equilibrium, it describes the balance between the ∇p force and the magnetic force $\mathbf{J} \times \mathbf{B}$, maintaining plasma confinement. The energy equation serves as the equation of state for closing the fluid model. The complete derivation of the MHD model is reported, for example, in Ref.[1].

3.1.2 Normal modes and Energy principle

The MHD model allows us to investigate how a plasma behaves within a specific magnetic configuration. The plasma equilibrium is characterized by setting the time derivatives in Eqs. (3.9-3.14) to zero, $\partial/\partial t = 0$. Additionally, it is assumed that there is no fluid flow in equilibrium, setting $\mathbf{u} = 0$. From Eq. (3.10), it is evident that at equilibrium, a balance must be maintained between the magnetic force and the pressure gradient:

$$\frac{1}{c}\mathbf{J} \times \mathbf{B} = \nabla p \tag{3.15}$$

In a tokamak's equilibrium state, the pressure gradient is thus constrained by the confining effects of the magnetic field. However, solving this equation for arbitrary

poloidal shaping is complex. The magnetic field's poloidal component is influenced not only by external factors like poloidal coils but also by the poloidal magnetic flux, associated with the plasma current. This flux, in turn, affects the pressure profile.

Once this delicate equilibrium force balance is established, the next step is to examine its response to small perturbations, studying its *stability* properties. The ideal MHD model can be linearized, expanding all quantities in their equilibrium and perturbed parts $Q(\mathbf{r},t) = Q_0(\mathbf{r}) + Q_1(\mathbf{r},t)$, with small perturbation satisfying $|Q_1/Q_0| \ll 1$. This approach allows for the investigation of the *linear stability* of the system. The perturbed part of a quantity can be related to the *displacement vector* $\tilde{\overline{\xi}}(\mathbf{r},t)$, which characterizes the shift of the plasma from its equilibrium position:

$$\mathbf{u}_1 = \frac{\partial \tilde{\overline{\xi}}}{\partial t} \tag{3.16}$$

Substituting the linearized mass and energy equations (3.9) and (3.11), along with Faraday's law (3.13), into the momentum equation (3.10) in terms of the displacement vector, in absence of equilibrium flows, we can derive:

$$\rho \frac{\partial^2 \tilde{\overline{\xi}}}{\partial t^2} = \mathbf{F}(\tilde{\overline{\xi}}) = \frac{1}{c}\mathbf{J} \times \mathbf{B}_1 + \frac{1}{c}\mathbf{J}_1 \times \mathbf{B} - \nabla p_1 \tag{3.17}$$

where the subscript 0 for equilibrium quantities has been dropped. $\mathbf{F}$ is called the force operator. The linear stability can be investigated through a *normal modes* analysis. By considering solutions of the form $\tilde{\overline{\xi}}(\mathbf{r},t) = \sum_q a_q \overline{\xi}_q(\mathbf{r}) \exp(-i\omega_q t)$, we obtain the eigenvalue problem formalism for each decoupled q component:

$$-\omega_q^2 \rho \overline{\xi}_q = \mathbf{F}(\overline{\xi}_q) \tag{3.18}$$

where the eigenvalue ω_q^2 can be determined by solving the problem with appropriate boundary conditions for $\overline{\xi}$. The force operator can be written explicitly in terms of $\overline{\xi}$:

$$\mathbf{F}(\overline{\xi}) = \frac{1}{4\pi}(\nabla \times \mathbf{B}) \times \mathbf{B}_1 + \frac{1}{4\pi}(\nabla \times \mathbf{B}_1) \times \mathbf{B} + \nabla(\overline{\xi} \cdot \nabla p + \gamma p \nabla \overline{\xi}) \tag{3.19}$$

This approach reveals that the force operator $\mathbf{F}(\overline{\xi})$ is self-adjoint if appropriate boundary conditions are considered. This property has significant implications for the study of plasma stability. Firstly,the eigenvalues ω_q^2 are real, implying that

instability (i.e., $\mathscr{I}m(\omega_q) > 0$) can only occur if $\omega_q^2 < 0$. Moreover, the eigenvectors $\overline{\xi}_q$ form a complete orthogonal set. This orthogonality ensures that an arbitrary initial perturbation will be dominated by the fastest growing mode, as opposed to a combination of different modes in a non-orthogonal case. The displacement vector of a normal mode, denoted as $\overline{\xi}(\mathbf{r})$ (with the subscript q dropped), is solely a function of the spatial variable $\mathbf{r}$. In the context of a tokamak equilibrium featuring a circular poloidal cross section, symmetries regarding the poloidal and toroidal angles, θ and φ, allow for the Fourier analysis of the perturbation:

$$\overline{\xi}(\mathbf{r}) = \overline{\xi}(r)\exp[i(m\theta + n\varphi)] \tag{3.20}$$

Here, m and n represent the poloidal and toroidal mode numbers, respectively. Geometric factors, such as toroidicity and cross-sectional elongation, as well as non-linear effects, may introduce interactions among perturbations characterized by different m and n, with important implications for plasma stability [9, 10].

In the context of Ideal MHD, thanks to the self adjointness of the force operator $\mathbf{F}(\overline{\xi})$, the stability analyses commonly make use of an *Energy Principle* [29]. According to this principle, an equilibrium is stable if and only if the variation of the potential energy integral, given by

$$\delta W = -\frac{1}{2}\int \overline{\xi}^* \cdot \mathbf{F}(\overline{\xi}) d^3x, \tag{3.21}$$

is positive for any physically acceptable displacement $\overline{\xi}$ that satisfies appropriate boundary conditions. The energy principle offers two key advantages over a full normal-mode analysis in determining the stability of an equilibrium. Firstly, one can hypothesize the form of an unstable perturbation, using it as a trial function $\overline{\xi}_{trial}$ to evaluate δW. If $\delta W(\overline{\xi}^*_{trial}, \overline{\xi}_{trial}) < 0$, the Energy principle ensures the equilibrium's instability, as there exists a physically acceptable displacement ($\overline{\xi}_{trial}$) for which δW is negative. The second advantage lies in the ability to search for the stationary points of δW by setting its variation with respect to $\overline{\xi}$ equal to zero. While this variational procedure is somewhat more challenging than the trial function approach, it is significantly less complex than a full normal-mode analysis. The energy principle has been extended in order to take into account equilibrium flows [30], derived in a more rigorous hamiltonian formalism in Refs. [31, 32] and, as discussed extensively in Sec. 3.2.1, extended to take into account the effect of energetic ions.

3.2 Hybrid kinetic MHD model

The presence of energetic particle populations introduces a unique set of instabilities associated with the resonance interaction between the periodic motions of these particles and the macroscopic modes of the thermal plasma. Examples of such instabilities include fishbone oscillations ([7],[8]) and Alfvén Eigenmodes ([9, 10, 33]). The ideal MHD model, due to its simplifications, falls short in addressing effects related to the presence of energetic particles. To investigate resonance interactions between macroscopic plasma modes and energetic particle populations, a different model, known as the *Hybrid Kinetic MHD*, must be considered. This hybrid kinetic MHD model utilizes the ideal MHD equations to handle the thermal plasma while a kinetic plasma description account for contributions from energetic particles. The limitations of the ideal MHD model in addressing the effects of superthermal particles stem from its fluid nature. The wave-particle resonance, which acts as a free energy source for fast ion-driven instability, is inherently a kinetic effect that necessitates a kinetic description of the plasma for accurate representation. Furthermore, the fluid closure utilized in the ideal MHD model loses validity in the presence of energetic particles. Even in the absence of wave-particle resonances, the conservation of the third adiabatic invariant, as described in Sec.2.1, introduces a non-local correction to the motion of fast particles. Consequently, defining fluid elements is no longer possible. Overall, when these particles exert a significant influence on the plasma, a fluid closure is no longer tenable.

The Hybrid Kinetic-MHD model equations are:

$$\frac{\partial \rho}{\partial t} + \nabla(\rho \mathbf{u}) = 0 \tag{3.22}$$

$$\rho \frac{d\mathbf{u}}{dt} = \frac{1}{c}\mathbf{J} \times \mathbf{B} - \nabla p_c - \nabla \cdot \overline{\mathbf{P}}_h \tag{3.23}$$

$$\frac{d}{dt}\left(\frac{p_c}{\rho^{\Gamma}}\right) = 0 \tag{3.24}$$

$$\nabla \times \mathbf{B} = \frac{4\pi}{c}\mathbf{J} \tag{3.25}$$

$$\frac{\partial \mathbf{B}}{\partial t} = \nabla \times (\mathbf{u} \times \mathbf{B}) \tag{3.26}$$

For the thermal plasma, we consider the same ideal MHD equations (Eqs. 3.9-3.14). The scalar pressure of the core plasma is denoted as p_c. The effects of

superthermal particles are incorporated in Eq. (3.23) through the "hot" particles pressure tensor, $\overline{\mathbf{P}}_h$, and are described using the kinetic model. Analogous to the CGL model assumption for pressure, the conservation of the magnetic moment applies to fast ions, and the pressure tensor is given by:

$$\overline{\mathbf{P}}_h = p_{\perp h}\overline{\mathbf{I}} + (p_{\parallel} - p_{\perp})_h \hat{e_{\parallel}}\hat{e_{\parallel}} \tag{3.27}$$

$$p_{\perp h} = m_h \int d^3v \frac{v_{\perp}^2}{2} f_h; \quad p_{\parallel h} = m_h \int d^3v v_{\parallel}^2 f_h \tag{3.28}$$

where $f_h(\mathbf{r},\mathbf{v},t)$ is the distribution function of the energetic particles described by the Vlasov equation:

$$\frac{\partial f_h}{\partial t} + \mathbf{v}\cdot\nabla f_h + \frac{q_h}{m_h}\left(\mathbf{E} + \frac{1}{c}\mathbf{v}\times\mathbf{B}\right)\cdot\frac{\partial f_h}{\partial \mathbf{v}} = 0 \tag{3.29}$$

that following the procedure outlined in Ch. 2, reduces to the collisionless drift-kinetic equation of Eq. (2.39). The model outlined in Eqs. (3.22-3.26) couples the bulk plasma and the superthermal particle component via the "hot" pressure tensor, leading to the so-called *Pressure Coupling Scheme* (PCS). Alternative couplings make use of the "hot" particle current $\mathbf{J}_h$, defining *Current Coupling Schemes* (CCS) [34]. The PCS considered here is not optimal under certain conditions, being non-hamiltonian [35]. However, it is the more convenient to use and its validity is ensured for the situations of interest for this work.

3.2.1 Fast ions δW

The linear stability of the plasma can be analyzed using a similar approach as described in Section 3.1.2 for the ideal MHD model. In the hybrid kinetic MHD model, an extended energy principle is formulated, taking into account the work done by the perturbation against the pressure from superthermal particles. The total δW will be the combination of the core plasma and the fast ions contributions:

$$\delta W = -\frac{1}{2}\int \overline{\xi}^*[\cdot\mathbf{F}_c(\overline{\xi}) + \mathbf{F}_{hot}(\overline{\xi})]d^3x, \tag{3.30}$$

The inclusion of the nonadiabatic term in the perturbed pressure tensor of energetic particles, as given by Eq (2.59), in the term $\mathbf{F}_{hot}$, disrupts the self-adjoint nature of the full force operator $\mathbf{F} = \mathbf{F}_c + \mathbf{F}_{hot}$. Consequently, an energy principle analogous

to that of ideal MHD cannot be straightforwardly derived, and normal mode analysis is required. Despite this complication, the stability in the presence of energetic particles can still be examined in the δW formalism. This is achieved by deriving the dispersion relation of the mode in terms of the following quadratic forms with a perturbative approach.

$$\delta I = -\delta W = -\delta W_c - \delta W_{hot} \tag{3.31}$$

$$\delta I = \frac{1}{2}\int d^3x \rho_m \overline{\xi}^* \cdot \frac{\partial^2 \overline{\xi}}{\partial t^2} \tag{3.32}$$

$$\delta W_c = -\frac{1}{2}\int d^3x \overline{\xi}^* \cdot \mathbf{F}_{core}(\overline{\xi}) \tag{3.33}$$

$$\delta W_{hot} = \frac{1}{2}\int d^3x \overline{\xi}^* \cdot (\nabla \cdot \overline{\mathbf{P}}_h^{(1)}) \tag{3.34}$$

The perturbative approach for the derivation of the dispersion relation is based on the use of the displacement vector obtained by the ideal-MHD normal mode analysis. The dispersion relation obtained from the quadratic forms must coincide at its lowest order with the ideal-MHD dispersion relation, obtained in the absence of energetic particles. In other words, this means that the zeroth-order terms of $\mathbf{F}$ represent a self-adjoint form related to a potential energy integral, whose minimization leads to the derivation of the ideal-MHD displacement vector. This can be obtained only considering $|\delta W_{hot}| \ll |\delta W_c|$. The nonadiabatic term in the perturbed pressure tensor of energetic particles introduces the mode-particle resonance contribution, resulting in a frequency-dependent imaginary part of δW. Given the condition $|\delta W_{hot}| \ll |\delta W_c|$, only this imaginary part significantly influences the stability in our analysis. In the following, our attention will be dedicated to the derivation of the imaginary component of δW_{hot}. This formulation of δW_{hot} follows a standard procedure, as outlined, for instance, in Ref. [36].

Since the general case of an anisotropic equilibrium pressure tensor introduces more real terms to δW_{hot} but does not affect its imaginary part, we will consider the simpler case of isotropic fast particle equilibrium pressure $\overline{\mathbf{P}}_{h,eq} = p_{h,eq}\overline{\mathbf{I}}$. The modification of fast ions to the equilibrium only accounts for a modification of the total scalar pressure as $p_{tot} = p_c + p_{h,eq}$. The perturbed fast particle pressure tensor instead is anisotropic and can be expressed as:

$$\overline{\mathbf{P}}_h^{(1)} = p_\perp^{(1)}\overline{\mathbf{I}} + (p_\parallel^{(1)} - p_\perp^{(1)})\hat{e}_\parallel\hat{e}_\parallel \tag{3.35}$$

with

$$\begin{pmatrix} p_{\perp}^{(1)} \\ p_{\parallel}^{(1)} \end{pmatrix} = \int d^3v \begin{pmatrix} \mu B \\ m v_{\parallel}^2 \end{pmatrix} f^{(1)} \tag{3.36}$$

where $f^{(1)}$ is the perturbed distribution function described by the linearized drift-kinetic equation in Eq. (2.48). Following the steps outlined in Ref. [36], it is possible to express δW_{hot} in terms of the perturbed Lagrangian of the particle motion:

$$\delta W_{hot} = -\frac{1}{2} \int d^3x d^3v \mathscr{L}^{(1)*} f^{(1)} \tag{3.37}$$

Exploiting the fact that $f^{(1)}$ in Eq. (2.48) has an adiabatic and a nonadiabatic part, we can split δW_{hot} into the same two terms:

$$\delta W_{hot} = \delta W_1 + \delta W_2(\omega) \tag{3.38}$$

We are particularly interested in the frequency-dependent nonadiabatic part $\delta W_2(\omega)$, which incorporates the mode-particle resonance contribution. Expressing the nonadiabatic term of δW_{hot} using Eq. (2.52), we obtain:

$$\delta W_2(\omega) = \frac{1}{2} i \int d^3x d^3v (\omega - n\omega_*) \frac{\partial F}{\partial E} \mathscr{L}^{(1)*} \int_{-\infty}^{t} \mathscr{L}^{(1)}(\tau) d\tau \tag{3.39}$$

The perturbed Lagrangian $\mathscr{L}^{(1)}$ can be expanded in harmonics of the bounce/passing periodicity, as shown in Eq. (2.56). The time integration of the Lagrangian reveals the resonant condition:

$$\delta W_2 = -\frac{1}{2} \int d^3x d^3v (\omega - n\omega_*) \frac{\partial F}{\partial E} \sum_{-\infty}^{+\infty}{}_l \Upsilon_l^* e^{il\omega_{b,t}\tau} \sum_{-\infty}^{+\infty}{}_p \frac{\Upsilon_p e^{-ip\omega_{b,t}\tau}}{\omega + p\omega_{b,t} + n\langle\varphi\rangle} \tag{3.40}$$

To proceed with the calculation, it is convenient to change the variables of integration using the transformation $(\mathbf{x},\mathbf{v}) \rightarrow (P_\varphi, \varphi, E, \tau, \mu, \alpha)$. The Jacobian of this transformation is a constant:

$$d^3x d^3v = \left(\frac{c}{Zem^2}\right) \sum_\sigma dP_\varphi d\varphi dE d\tau d\mu d\alpha \tag{3.41}$$

After this change of variables, δW_2 can be expressed as:

$$\delta W_2 = -\frac{1}{2}\left(\frac{c}{Zem^2}\right)\sum_{\sigma}\int dP_{\varphi}d\varphi dEd\tau d\mu d\alpha(\omega - n\omega_*)\frac{\partial F}{\partial E} \sum_{-\infty}^{+\infty}{}_l \Upsilon_l^* e^{il\omega_{b,t}\tau}\sum_{-\infty}^{+\infty}{}_p \frac{\Upsilon_p e^{-ip\omega_{b,t}\tau}}{\omega + p\omega_{b,t} + n\langle\varphi\rangle} \tag{3.42}$$

Carrying out the integration in τ, α and φ:

$$\int d\alpha = 2\pi \tag{3.43}$$

$$\int d\varphi = 2\pi \tag{3.44}$$

$$\int d\tau e^{i(l-p)\omega_{b,t}\tau} = \frac{2\pi}{\omega_{b,t}}\delta(l-p) \tag{3.45}$$

obtaining the following expression for δW_2:

$$\delta W_2 = -\frac{2\pi^2 c}{Zem^2}\sum_{\sigma}\int dP_{\varphi}dEd\mu\,\tau_t(\omega - n\omega_*)\frac{\partial F}{\partial E}\sum_{-\infty}^{+\infty}{}_p \frac{\left|\Upsilon_p\right|^2}{\omega + p\omega_{b,t} + n\langle\varphi\rangle} \tag{3.46}$$

In this study, our focus is on axisymmetric modes characterized by the toroidal mode number $n = 0$. In this particular case, the expression for δW_2 can be simplified, highlighting two peculiar characteristics of the fast ion resonance with $n = 0$ modes.

$$\delta W_2 = -\frac{2\pi^2 c}{Zem^2}\sum_{\sigma}\int dP_{\varphi}dEd\mu\,\tau_t\omega\frac{\partial F}{\partial E}\sum_{-\infty}^{+\infty}{}_p \frac{\left|\Upsilon_p\right|^2}{\omega + p\omega_{b,t}} \tag{3.47}$$

Firstly, as briefly mentioned in Chapter 2, the resonant condition reduces to $\omega + p\omega_{b,t}$. This implies that the mode must resonate with the passing or bounce orbits of the fast ions in the poloidal plane. It also means that the $p = 0$ harmonic, usually associated with the largest Fourier coefficient Υ_0, cannot contribute to the wave-particle resonant interaction. A second consequence of the $n = 0$ perturbation is that the ω^* term vanishes. This term is associated with the $\partial F/\partial P_{\varphi}$ derivative of the equilibrium distribution function and is the one providing the main drive for the destabilization of other types of fast ion modes, like Toroidal Alfvén Eigenmodes (TAEs). For

axisymmetric modes, the resonant interaction depend only on the velocity space derivative of the distribution function $\partial F/\partial E$.

3.2.2 Particle distribution function and Fokker-Plank equation

As discussed above, for the resonance with $n = 0$ modes, a crucial characteristic of the superthermal particles is the slope of their equilibrium distribution function in velocity space $\partial F/\partial E$. It is important to note that in Eq. (3.47), the derivative is taken at constant μ. Therefore, two contributions arise:

$$\left.\frac{\partial F}{\partial E}\right|_{\mu} = \left.\frac{\partial F}{\partial E}\right|_{\Lambda} - \frac{\Lambda}{E}\left.\frac{\partial F}{\partial \Lambda}\right|_{E} \tag{3.48}$$

Recalling the pitch angle defined as $\Lambda = \mu B/E$. The sign of $\partial F/\partial E|_{\mu}$ determines the sign of δW_2 and, as discussed in more detail later, the sign of the wave-particle resonant interaction, leading to either driving or damping of the mode.

Given that fast ions possess a superthermal energy, their equilibrium distribution function can vary significantly from a Maxwellian distribution. The equilibrium distribution function depends on the thermalization process of fast ions through collisions with the bulk plasma. This process is described by the Fokker-Planck equation:

$$\frac{\partial f}{\partial t} + \mathbf{v}_{gc} \cdot \nabla f = C(f) + S - L \tag{3.49}$$

Here, $\mathbf{v}_{gc} = \mathbf{v}_D + v_{\parallel}\hat{e}_{\parallel}$ represents the guiding center velocity, and $C(f)$, S, and L denote the collision, source, and loss terms.

In tokamak plasmas, energetic ions primarily collide with electrons until they reach a critical energy $E_c \approx 41T_e$, beyond which ion collisions become dominant, leading to rapid particle thermalization. For particles with energies greater than E_c, the collision operator describing the slowing down due to electron collisions can be expressed as:

$$C(f) = \frac{1}{\tau_{sd} v^2}\frac{\partial v^3 f}{\partial v} \tag{3.50}$$

Here, v represents the particle velocity, and τ_s is the slowing down time, which is the time required for a fast ion to reach the critical energy through electron collisions

and thermalize. It is defined as:

$$\tau_{sd} = \frac{\tau_{sp}}{3} \ln \left[1 + \left(\frac{E_b}{E_c} \right)^{3/2} \right] \tag{3.51}$$

with $E_b = m v_b^2/2$ birth energy of the energetic ion and the Spitzer time defined as:

$$\tau_{sp} \approx c_\tau \frac{T^{3/2}}{n_e} \tag{3.52}$$

where $c_\tau = 1.77 \cdot 10^{-2}$ if in Eq. (3.52) T is in keV, n_e in $10^{20} m^{-3}$ and τ_{se} in s [37]. The slowing down time is usually much smaller than the bounce/passing time of a poloidal plane orbit, with $\tau_{b,t}/\tau_{sd} \ll 1$. We expand the distribution function solution of Eq. (3.50) in powers of $\tau_{b,t}/\tau_{sd}$ as $f = f_0 + \tau_{b,t}/\tau_{sd} f_1 + ...$ To first order the Fokker-Plank equation reads:

$$\frac{\partial f_0}{\partial t} + \mathbf{v}_{gc} \cdot \nabla f_1 = \frac{1}{\tau_{sd} v^2} \frac{\partial v^3 f_0}{\partial v} + S - L \tag{3.53}$$

Taking the average over the bounce angle removes the f_1 term, as shown eg. in [38], and neglecting the underscore 0, the following simplified Fokker-Plank equation is obtained:

$$\frac{\partial f}{\partial t} = \frac{1}{\tau_{sd} v^2} \frac{\partial v^3 f}{\partial v} + S - L \tag{3.54}$$

3.3 Equilibrium distribution functions

In this section, we analyze different distribution functions by solving the simplified Fokker-Plank equation, Eq. (3.54). The results discussed in this section are based on our findings presented in Ref. [14]. Some detail of the calculations carried out in this section are discussed extensively in App. A. The source term is assumed to be monochromatic, with birth-velocity v_b:

$$S(v) = K \delta(v - v_b) \tag{3.55}$$

where $\delta(x)$ is a Dirac delta function, and the parameter K is related to the total number of energetic ions born per m^3 per second. For a D-T plasma with $n_D = n_T = n_e/2$, K can be determined by considering fusion-born alpha particles and integrating the

source of Eq. (3.55) over velocity:

$$K = \frac{n_e^2}{16\pi}\frac{1}{v_b^2}\langle\sigma v\rangle \tag{3.56}$$

The reaction rate $\langle\sigma v\rangle$ for D-T reactions averaged over Maxwellian distribution can be expressed as a function of T only [37]:

$$\begin{aligned}\langle\sigma v\rangle|_{DT} &= 3.7\cdot 10^{-18} * T^{-2/3} * \exp\left(-20T^{-1/3}\right)[m^3/s] \\ &\approx 8\cdot 10^{-23} * T^2\end{aligned} \tag{3.57}$$

with $\overline{\sigma v}|_{DT}$ in m^3/s and T in keV, leading to the following expression for the source term in Eq. (3.54):

$$S = c_1\frac{n_e^2}{v_b^2}T^2\delta(v - v_b) \tag{3.58}$$

where $c_1 = 8\cdot 10^{-23}/16\pi\ m^3 keV^{-2}/s$. A very simple loss term is considered, with velocity independent loss frequency ν_l:

$$L = \nu_l f \tag{3.59}$$

Defining $\hat{F} = v^3 f$, the simplified Fokker-Plank equation to be solved is:

$$\frac{\partial\hat{F}}{\partial t} - \frac{v}{\tau_{sd}}\frac{\partial\hat{F}}{\partial v} + \nu_l\hat{F} = v^3 S \tag{3.60}$$

3.3.1 Simple slowing down

The first case we will consider is the standard case of a *slowing down distribution* obtained, for example, in Refs.[39], [40] and [41]. The slowing down time is assumed constant, τ_{sd0}, while the source term is considered to be isotropic in velocity with $S = S_0\delta(v - v_b)$. The differential equation Eq. (A.15) can be solved using standard techniques. Looking for the steady-state solution, i.e., for our equilibrium distribution function of fast ions, we set $\partial\hat{F}/\partial t = 0$:

$$F(v) = \tau_{sd}S_0 v_b^{2-3l_0}\frac{H(v_b - v)}{v^{3-3l_0}} \tag{3.61}$$

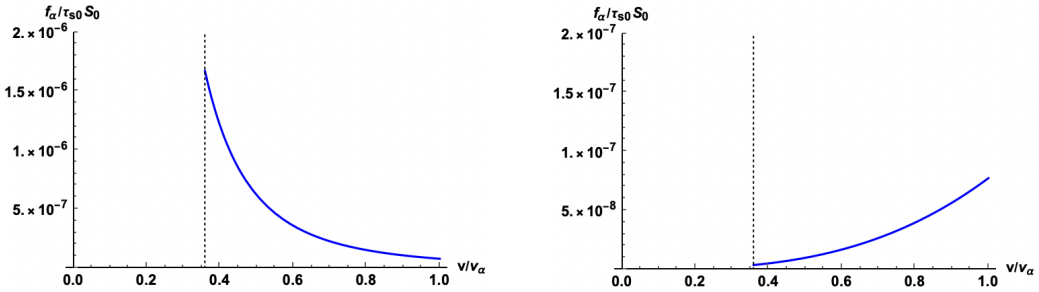

(a) (b)

Fig. 3.1 Steady state distribution functions as a function of normalized velocity, obtained for constant τ_{sd0} and source term. The distribution functions are plotted up to the critical velocity v_c, showed with vertical dotted line. In (a) the standard slowing down with no losses ($l_0 = 0$) is displayed. Figure (b) shows the slowing down solution for $l_0 = 2$.

where $l_0 = \nu_l \tau_{sd0}/3$. It is important to remark that this solution is valid for velocities larger than the critical velocity v_c, and corrections of the order of $(v_c/v)^3$ have been neglected. Due to the assumption of an isotropic source term, the resulting distribution is isotropic in velocity space, and therefore $\partial F/\partial\Lambda = 0$. The derivative of the distribution function with respect to velocity depends on the loss exponent l_0. When the losses exceed the threshold $\nu_l = 3/\tau_{s0}$, or $l_0 = 1$, most particles are lost before their complete slow down, and $\partial F/\partial v$ changes sign, as shown in Fig.3.1.

To introduce anisotropy effects, we can consider a source of particles characterized by a single direction in velocity space Λ_0, represented as $S = \hat{S}_0\delta(v - v_b)\delta(\Lambda - \Lambda_0)$. The normalization constant $\hat{S}_0$ is modified by the anisotropy and depends on the single pitch Λ_0, as detailed in Ch. 5. The resulting distribution function is the same as the one derived previously, but now includes an additional term to account for the anisotropy:

$$F(v,\Lambda) = \tau_{sd}\hat{S}_0 v_b^{2-3l_0}\frac{H(v_b - v)\delta(\Lambda - \Lambda_0)}{v^{3-3l_0}} \tag{3.62}$$

The slowing-down distribution with a single pitch angle, denoted as the "single-pitch" distribution in the following sections, exhibits a non-zero derivative with respect to the pitch angle, Λ. When taking the full derivative over the energy at constant μ, both contributions from the slowing-down part $1/v^{3-3l_0}$ and the term $\partial F/\partial\Lambda$ must be considered.

3.3.2 Sawtooth induced distribution function

The distribution function of energetic particles in velocity space can exhibit a steady-state solution with a positive slope with respect to energy, due to losses or velocity space anisotropies. However, achieving such condition transiently in a tokamak plasma is also possible. If the timescale for changes in the distribution function is significantly longer than the typical timescales of the phenomena under consideration, a snapshot of a time-dependent distribution function can be treated as the equilibrium distribution function F in Eq. (3.47).

Transient distribution functions with $\partial F/\partial E|_\mu > 0$ in tokamak plasmas can be obtained by modulating the power of Neutral Beam Injection (NBI) systems in plasmas, as discussed theoretically in [42] and experimentally in the DIII-D tokamak in [43]. Another possibility, explored in the following and suggested in [44], is that sawtooth oscillations may also influence the distribution function in the same way.

Sawtooth oscillations, a well-known form of MHD activity, result in periodic relaxation of pressure in the core region of the plasma, playing a crucial role in various fusion devices. On one hand, the presence of fast ions can stabilize sawtooth oscillations, potentially leading to "monster sawteeth" characterized by extended sawtooth periods and significant crashes [45]. On the other hand, the loss of core plasma confinement and the redistribution of pressure towards more peripheral plasma regions also impacts fast ions. Consequently, the radial redistribution of energetic ions during sawtooth crashes has been the subject of numerous works [46–48]. Several studies have demonstrated that fast ions with MeV energies may experience minimal spatial redistribution during sawtooth crashes, as initially discussed by Kolesnichenko et al. [49–51] and more recently confirmed by kinetic-MHD simulations conducted by Bierwage et al. [52]. Here, we make the assumption that fusion alpha particles with MeV energies experience no radial redistribution during sawtooth dynamics. Instead, our focus shifts to examining changes in the distribution function in velocity space for the energetic tail of isotropic fast particle distributions.

Two primary effects associated with the core temperature drop caused by sawtooth crashes significantly modify the fast ion population's velocity distribution function:

- The decrease in fusion yield after the core temperature crash for fusion born alpha particles, effectively modulating their source on the sawtooth period (τ_{saw}) timescale.
- The slowing down time of fast ions (τ_{sd}) grows during the sawtooth ramp, leading to an accumulation of particles at higher velocities generated in the later stages of the ramp.

By incorporating these effects into the simplified Fokker-Planck equation of Eq. (3.54), we obtain a time-dependent distribution function, periodic with a period of τ_{saw}. Depending on the ratio between the slowing down time and the sawtooth period ($\tau_{\text{sd}}/\tau_{\text{saw}}$), the derivative over velocity of the newly obtained distribution function may change sign.

Pressure evolution after crashes

Sawtooth oscillations, as observed in tokamak plasma discharges [53], are quasi-periodic phenomena occurring in the core region near the magnetic axis when the safety factor, q, drops below unity. This phenomenon involves two distinct stages: the slower sawtooth ramp, characterized by a gradual temperature rise influenced by heating and transport, and the much faster sawtooth crash, triggered by the onset of a kink instability dominated by toroidal and poloidal mode numbers $n = 1$ and $m = 1$. During the crash, core confinement is rapidly lost on a timescale much shorter than the transport time, resulting in the flattening of profiles up to a radius known as the "mixing radius" r_{mix}, which surpasses the $q = 1$ resonant surface radius, r_s. Various theoretical models, such as the ones of Refs. [54, 55], have been proposed to describe the relaxed profiles after the crash. The Kadomtsev model of Ref.[54] allows for analytic treatment in some cases. Given the following profile for the inverse of q before the crash, it is possible to derive the relaxed q and pressure profiles up to the mixing radius r_{mix} analytically.

$$q(r^2)^{-1}_{pre} = \frac{1}{q_0}\left(1 - \Delta q \frac{r^2}{r_s^2}\right) \tag{3.63}$$

where $\Delta q = 1 - q_0$ and $q(r_s) = 1$. Following the Kadomtsev relaxation model, as detailed in App. A, the mixing radius is $r_{\text{mix}} = \sqrt{2} r_s$, and the relaxed inverse q profile

reads:

$$q(r^2)^{-1}_{rel} = 1 - \frac{1}{4}\frac{\Delta q}{q_0}\frac{r^2}{r_s^2} \tag{3.64}$$

In the relaxed state, q is above unity everywhere except on the magnetic axis, where $q_{0,\mathrm{rel}} = 1$. Figure 5.2 provides an example of precrash and relaxed profiles up to the mixing radius.

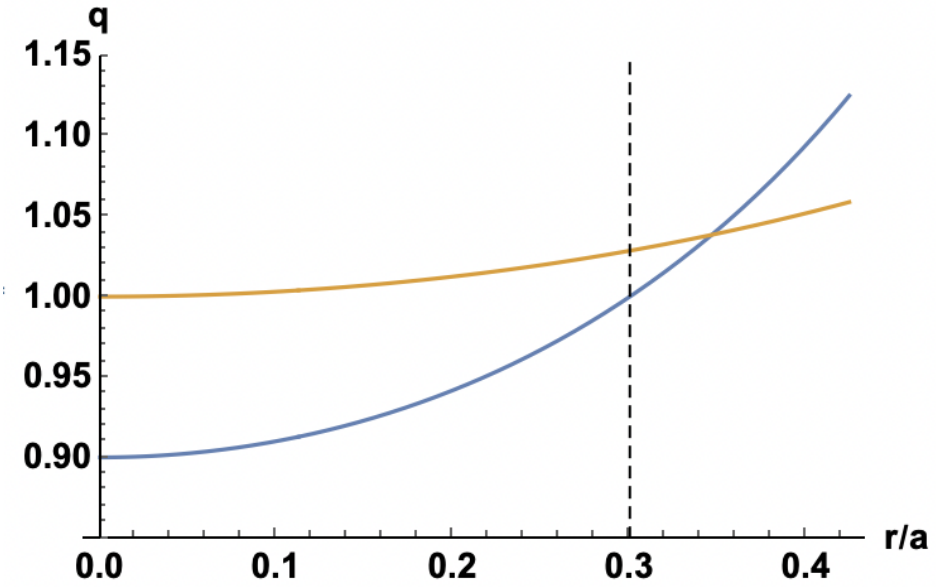

Fig. 3.2 Precrash (Blue) and relaxed (Orange) q profiles up to the mixing radius $r_{mix} = \sqrt{2}r_s$. The q=1 surface of the precrash profile is at $r_s/a = 0.3$ (dashed vertical line) and its value on axis is $q_0 = 0.9$.

The relaxed pressure can be determined through energy conservation arguments. The pre-crash pressure profile is assumed to be parabolic following:

$$p_{pre}(r^2) = p_0\left(1 - \frac{r^2}{r_p^2}\right), \tag{3.65}$$

with p_0 on-axis value and $r_p > r_{mix} = \sqrt{2}r_s$ describes up to which radius the parabolic assumption can be extended. Notice that for $r_p = r_{mix}$ the pressure goes to 0 at $r = r_{mix}$. For simplicity, a constant density profile unaffected by the sawtooth dynamics is assumed. As explained in App. A, this profile choice leads to a uniform relaxed profile up to the mixing radius. The sawtooth ramp phase is considered to be linear with time, representing triangular sawteeth. The temperature evolution within

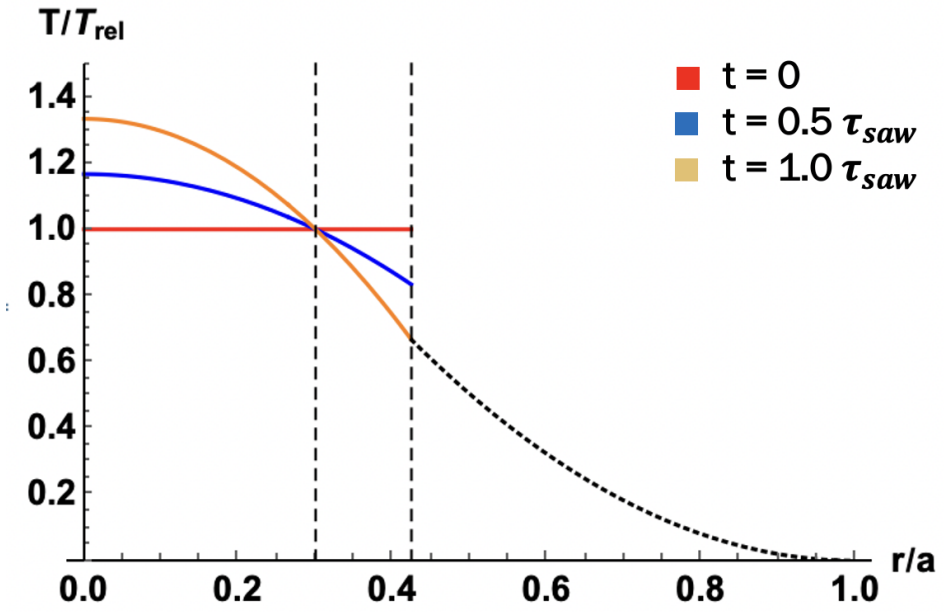

Fig. 3.3 Temperature profile normalized with the relaxed on-axis value $T_{0,rel}$, at different times during the sawtooth period. The $q = 1$ radius at $r_s/a = 0.3$ and the mixing radius at $r_{mix}/a = 0.3\sqrt{2}$ are shown with dashed vertical lines. The pressure scale length considered is $r_p/a = 0.6$, while outside the mixing radius the profile is time-independent. The relaxed temperature profile exhibits a jump at $r = r_{mix}$ that is rapidly smoothed out by temperature diffusion in the early part of the following sawtooth cycle.

the mixing radius during the first cycle ($0 \leq t \leq \tau_{saw}$) then follows:

$$T(r,t) = T_{0,rel}\left[1 + A(r)\frac{t}{\tau_{saw}}\right] \tag{3.66}$$

where $A(r) = (r_s^2 - r^2)/(r_p^2 - r_s^2)$. As depicted in Fig.3.3, with the chosen profiles for q and pre-crash pressure from Eqs.(3.63, 3.65), the relaxed temperature profile flattens to $T_{0,rel}$ up to the mixing radius. Just before the next crash, i.e., at $t = \tau_{saw}$, the central temperature peaks at $T_0 = T_{0,rel}\left[r_p^2/(r_p^2 - r_s^2)\right]$. In the region beyond the mixing radius, the profile is assumed to be unchanged with $T_{out}(r) = T_0(1 - r_{mix}^2/r_p^2)(r-a)^2/(r_{mix}-a)^2$. The Kadomtsev relaxation model introduces discontinuities in the q and T profiles at $r = r_{mix}$ after the crash. These discontinuities will decay rapidly if current and temperature diffusion are considered during the early part of the subsequent sawtooth ramp.

For standard sawtooth oscillations, the crash time τ_{crash} is significantly smaller than the sawtooth period. For simplicity, we assume an instantaneous crash ($\tau_{crash} \to 0$) with respect to the relevant timescales of interest. The temperature evolution during the sawtooth dynamics can be expressed as:

$$T(r,t) = T_{0,rel}\left[1 + A(r)\left(\frac{t}{\tau_{saw}} - \left\lfloor \frac{t}{\tau_{saw}} \right\rfloor\right)\right] \tag{3.67}$$

where $\lfloor t/\tau_{saw} \rfloor$ is the integer part of the quantity t/τ_{saw}. It is useful to define a piece-wise temperature evolution, during each sawtoooth cycle:

$$\begin{aligned} T_n(r,t) =& T_{0,rel}\left[1 + A(r)\left(\frac{t}{\tau_{saw}} - n\right)\right] \times \\ & \times H[(n+1)\tau_{saw} - t]H[t - n\tau_{saw}] \end{aligned} \tag{3.68}$$

where $H(x)$ is the Heaviside step function; the integer n labels the sawtooth cycles and is associated to the integer part of Eq. (3.67). An alternative expression for the temperature dynamics during multiple sawtooth cycles is:

$$T_{tot}(r,t) = \sum_{n=0}^{n_{max}} T_n(r,t) \tag{3.69}$$

where n_{max} labels the last sawtooth cycle. Notice that the expressions in Eq. (3.67) and Eq. (3.69) are completely equivalent for positive t, up to $t = n_{max}\tau_{saw}$.

In the following we will neglect the temperature dependence of E_c in the logarithm of Eq. (3.51), considering only the Spitzer time, τ_{sp}, variation with T. Following Eq. (3.66), also the slowing-down time will depend on time due to the sawtooth dynamic. Considering a density $n_e = 1 \cdot 10^{20} m^{-3}$, and a value of the relaxed temperature of 8 keV, the on-axis peak temperature is $T_0 \approx 10.7$ keV (for $r_p = 0.6, r_s = 0.3$). The corresponding slowing-down time will be varying between $0.33 \lesssim \tau_s[s] \lesssim 0.50$.

3.3.3 Source temperature modulation with average τ_{sd}

In this subsection, we explore the solution of Eq.(A.15) for a constant τ_{sd0} but a varying source term, following the temperature evolution given by Eq.(3.69). The assumption of instantaneous crashes allows us to analyze the solution within a single cycle, corresponding to a fixed n. The time-dependent source term during a cycle

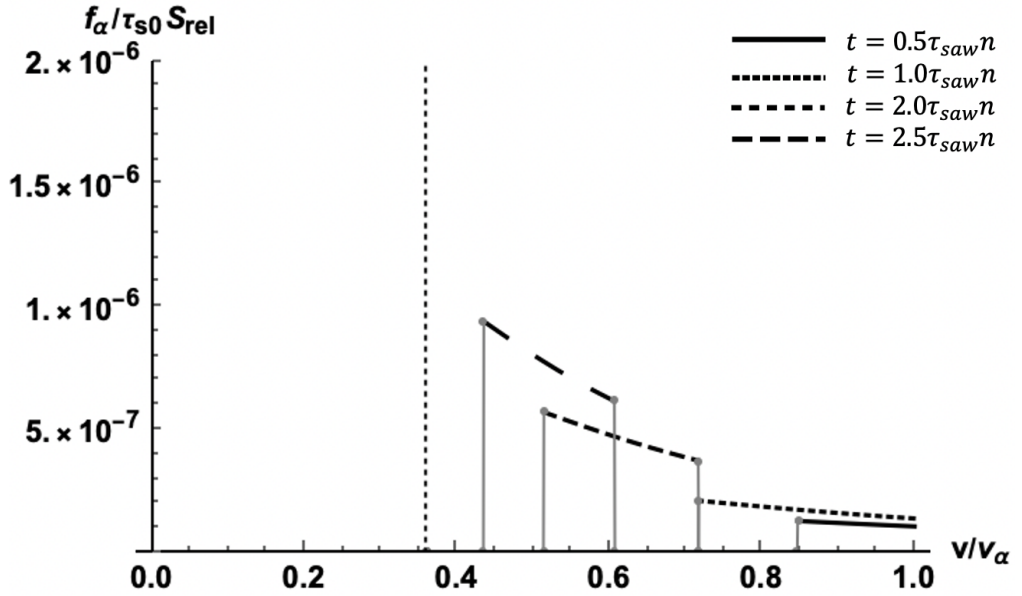

Fig. 3.4 Distribution function for particles born during the n-th cycle with time dependent source and constant τ_{sd}, plotted for different times as a function of normalized velocity for $r = 0$. The critical velocity v_c is showed with vertical dotted line. The minimum and maximum velocities reached by the n-th cycle particles at different times are highlighted. The loss term is $l_\alpha = 0$ and the ratio between slowing down and sawtooth period is $\tau_{sd0}/\tau_{saw} = 3$.

can be expressed as:

$$S_{\alpha,n}(r,t,v) = S_{rel}\left[1+A(r)\left(\frac{t}{\tau_{saw}}-n\right)\right]^2 \times H[(n+1)\tau_{saw}-t]H[t-n\tau_{saw}]\delta(v-v_b) \tag{3.70}$$

where $S_{rel} = c_S n_e^2 T_{0,rel}^2/v_b^2$ is the source term associated with the relaxed (flat profile) temperature. As detailed in App. A, the time dependent solution of Eq. (3.54) for particles born during the $n-th$ sawtooth cycle is:

$$\begin{aligned} &f_{\alpha,n}(r,t,v) = \tau_{sd0} v_b^{2-3l_\alpha} v^{-3+3l_\alpha} H\left[v_b - v\right] \times \\ &S_{rel}\left\{1+A(r)\left[\frac{t}{\tau_{saw}}+\frac{\tau_{sd0}}{\tau_{saw}}\log\left(\frac{v}{v_b}\right)-n\right]\right\}^2 \times \\ &H\left[v - v_b e^{(n\tau_{saw}-t)/\tau_{sd0}}\right] H\left[v_b e^{((n+1)\tau_{saw}-t)/\tau_{sd0}} - v\right] \end{aligned} \tag{3.71}$$

Figure 3.4 shows the distribution function of Eq. (3.71) at different times.

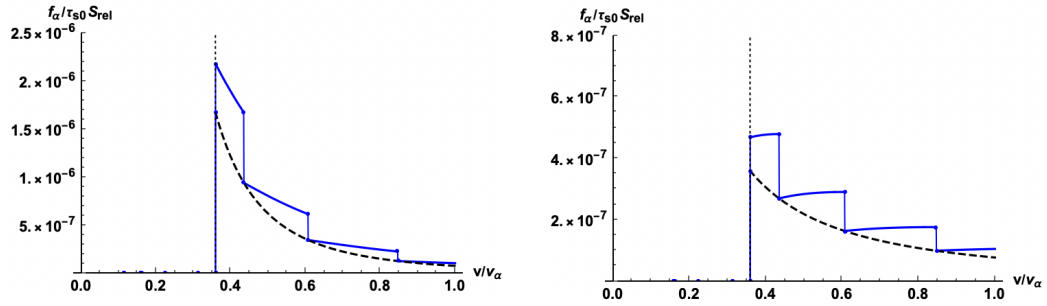

(a) (b)

Fig. 3.5 Time dependent distribution functions as a function of normalized velocity at time $t^* = 5.5\tau_{saw}$, obtained for constant τ_{sd} and varying source term. Distribution function plotted up to the critical velocity v_c, showed with vertical dotted line. In (a) the new time dependent distribution function (solid blue) and the slowing-down considering a constant source S_{rel} (dashed black) are plotted for $l_\alpha = 0$. Figure (b) shows the same two distributions for $l_\alpha = 0.5$. The ratio $\tau_{sd0}/\tau_{saw} = 3$.

The full solution over different cycles can be obtained by summing all the contributions coming from each n:

$$f_\alpha(r,t,v) = \sum_{n=0}^{n_{max}} f_{\alpha,n}(r,t,v). \tag{3.72}$$

After a slowing-down time, which is the duration for particles born during the first ($n = 0$) cycle to reach the critical velocity, the solution of Eq.(3.72) becomes periodic with a period of τ_{saw}. In Fig.3.5, a snapshot at $t = t^* = 5.5\tau_{saw}$ of the solution with $\tau_{sd0}/\tau_{saw} = 3$ is presented. At this time, all particles born during the first sawtooth period ($n = 0$) have already reached v_c, and only 4 steps are visible, associated with particles born during later sawtooth periods ($n = 1-4$). For a realistic choice of $\tau_{sd0}/\tau_{saw} = 3$, a positive slope is obtained only if the loss term is taken into account. In comparison with the simple slowing-down case, a positive slope can be obtained for values of $l_\alpha < 1$. Neglecting losses, $\partial f_\alpha/\partial v > 0$ can be obtained with source modulation only if $\tau_{sd0}/\tau_{saw} \sim 10$. The time dependence of the distribution function is depicted in Fig.3.6, where the same distribution function plotted in Fig.3.5b is displayed for $t^* = 5.1\tau_{saw}$, $5.5\tau_{saw}$, and $5.9\tau_{saw}$.

The source modulation occurring on the τ_{saw} timescale has a significant impact on the slope of the distribution function in velocity space. This effect strongly depends on the ratio between the slowing-down time and the modulation timescale τ_{sd0}/τ_{saw}. If the source modulation occurs on timescales longer than the slowing-down time

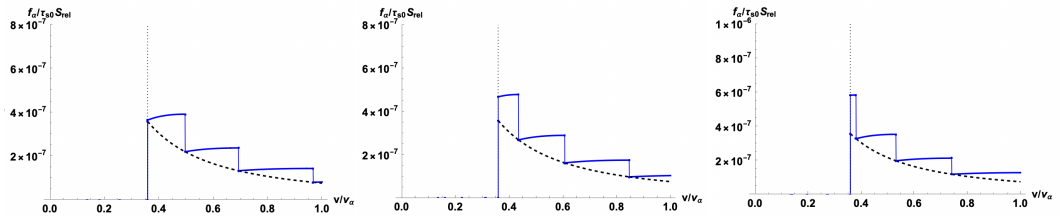

(a) (b) (c)

Fig. 3.6 Distribution function plotted for different times during the sawtooth ramp. The critical velocity v_c is showed with vertical dotted line. The loss exponent considered is $l_\alpha = 0.5$ and $\tau_{sd0}/\tau_{saw} = 3$. Solid blue line: time dependent distribution function; Dashed black line: slowing-down with constant source S_{rel}. The times displayed are $t^* = 5.1\tau_{saw}$ (a), $t^* = 5.5\tau_{saw}$ (b) and $t^* = 5.9\tau_{saw}$ (c)

($\tau_{sd0} < \tau_{saw}$), the effect becomes negligible. The situation described in this section can be considered analogous to the case of modulated Neutral Beam Injection (NBI) sources with a constant temperature background plasma. Within this analogy, the distribution function described by Eq. (3.71) is a pitch-angle averaged distribution function of NBI fast ions when their source follows a sawtooth-like waveform signal. A similar result was obtained for a pulsed source theoretically in [42] and verified experimentally in DIII-D [43].

3.3.4 Temperature modulation for τ_{sd} and constant source

In this sub-section, the effect of a non-constant slowing-down time is analyzed. A time independent source is assumed, $S_\alpha = S_0\delta(v - v_b)$, while the slowing-down time follows:

$$\tau_{sd}(r,t) = \tau_{sd,rel}\left[1 + A(r)\left(\frac{t}{\tau_{saw}} - \left\lfloor\frac{t}{\tau_{saw}}\right\rfloor\right)\right]^{3/2} \tag{3.73}$$

where $\tau_{sd,rel}$ is the slowing-down time in the relaxed, post-crash phase, where the on-axis temperature is lowest and the slowing-down time is shortest. Also in this scenario, we can track fast particles generated during different sawtooth cycles and eventually combine their contributions. However, due to the discontinuities in τ_{sd} associated with the temperature variation at the crashes, particular care is required, as discussed extensively in App. A. For the sake of simplicity, losses are neglected, i.e., $\nu_l = 0$.

The distribution function for particles born during the n-th sawtooth cycle is:

$$
\begin{aligned}
&f_{\alpha,n}(r,t,v) = S_0 \frac{v_b^2}{v^3} H\left[v_b - v\right] \times \\
&\tau_{sd,rel} \left\{ 1 + A(r) \left[\frac{\hat{t}_n(r,t,v)}{\tau_{saw}} - n \right] \right\}^{3/2} \times \\
&H\left[v - \hat{v}_{n,min}(r,t)\right] H\left[\hat{v}_{n,max}(r,t) - v\right]
\end{aligned}
\tag{3.74}
$$

Here, $\hat{t}_n(r,t,v)$ is a rather complicated function proportional to τ_{saw}, as defined in Eq.(A.47) of App.A. As illustrated for the source modulation case in Fig.3.4, particles born in each sawtooth cycle are associated with time-dependent minimum and maximum velocities. The same is true for varying τ_{sd}, and these velocities are $\hat{v}_{n,\min}$ and $\hat{v}_{n,\max}$, defined in Eqs.A.48 and A.49. Similar to the case with constant τ_{sd}, the full solution can be obtained by summing the contributions of each cycle:

$$
f_\alpha(r,t,v) = \sum_{n=0}^{n_{max}} f_{\alpha,n}(r,t,v) \tag{3.75}
$$

A snapshot of the full solution at time $t = t^* = 5.5\tau_{saw}$ is depicted in Fig. 3.7 for $\tau_{sd,rel}/\tau_{saw} = 3$. The distribution function becomes periodic, with period τ_{saw}, after the particles born during the first ($n = 0$) cycle have reached the critical velocity.

During each sawtooth ramp, the temperature increases linearly within the $q = 1$ radius. Particles born early in this process experience more pronounced slowing down due to collisions with the colder plasma, in contrast to those born later, who are less affected by collisions. This leads to an accumulation of particles at high energy born in the later stages of the ramp. Depending on the parameter $\tau_{sd,rel}/\tau_{saw}$, this effect can induce a change in the derivative $\partial f_\alpha(r,t,v)/\partial v$. However, similar to the source modulation case, this effect alone is insufficient to reverse the slope of the distribution function for values of $\tau_{sd,rel}/\tau_{saw} \lesssim 10$.

This effect is not limited to the case of fusion-born alphas. Indeed, the solution of Eq.(3.74) can be considered as a pitch-angle averaged distribution for a fast ion population injected with any constant source into a sawtoothing plasma.

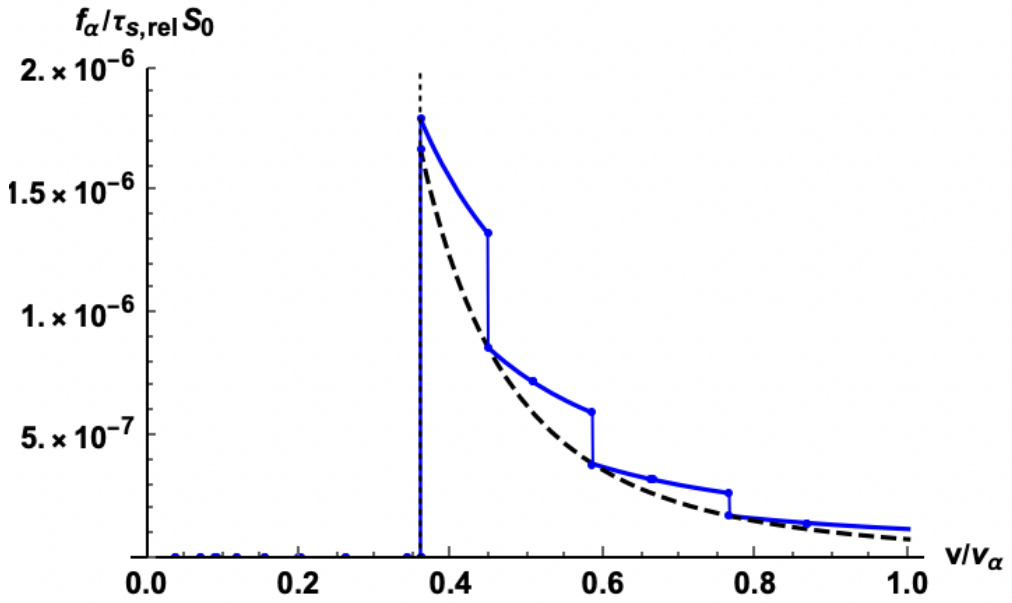

Fig. 3.7 Time dependent distribution function as a function of normalized velocity at time $t^* = 5.5\tau_{saw}$, obtained for varying τ_{sd} and constant source term. The distribution function is plotted up to the critical velocity showed with vertical dotted line. The time dependent distribution function (solid blue) is plotted for ratio $\tau_{sd,rel}/\tau_{saw} = 3$, together with the slowing-down obtained for a constant slowing-down time $\tau_{sd,rel}$ (dashed black).

3.3.5 Temperature modulation for both τ_{sd} and source

The combination of the effects discussed in subsecs.3.3.3 and 3.3.4 is considered here, representing the relevant scenario for alpha particles generated by fusion reactions in a sawtoothing plasma. The influence of the constant loss term is neglected, assuming $\nu_l = 0$. The particle source follows Eq.(3.70), and the slowing-down time varies according to Eq.(3.73). Similar to the previous situations, we initially focus on the solution for a single n-th cycle. Following the detailed procedure in App.A, the resulting distribution function is:

$$\begin{aligned} f_{\alpha,n}(r,t,v) &= S_{rel}\frac{v_b^2}{v^3}H\left[v_b - v\right]\times \\ &\tau_{sd,rel}\left\{1+A(r)\left[\frac{\hat{t}_n(r,t,v)}{\tau_{saw}} - n\right]\right\}^{7/2}\times \\ &H\left[v-\hat{v}_{n,min}(r,t)\right]H\left[\hat{v}_{n,max}(r,t)-v\right] \end{aligned} \tag{3.76}$$

The full solution is obtained again as the combination of the solutions associated to different ns, i.e. the summation of particles born during each n-th cycle:

$$f_\alpha(r,t,v) = \sum_{n=0}^{n_{max}} f_{\alpha,n}(r,t,v). \tag{3.77}$$

Figure 3.8 illustrates how the combination of the two effects enhances the slope change of the distribution function in velocity space, resulting from the periodic temperature evolution. A scenario with a piece-wise positive slope can be achieved with values of $\tau_{sd,rel}/\tau_{saw} \sim 3$, which is relevant for present-day tokamak experiments. In the limit of $\tau_{saw} \to \infty$, corresponding to a constant temperature, the slowing-down solution of Eq. (3.61) is recovered.

3.4 Concluding remarks

In this chapter, we have outlined the Magneto-Hydro-Dynamic models that will be employed in the subsequent chapters. A particular focus has been placed on the significant impact of superthermal ions and the necessity for a kinetic closure of the model. This discussion led to the formulation of the extended energy principle, which will be used to explore plasma stability in the presence of energetic ions.

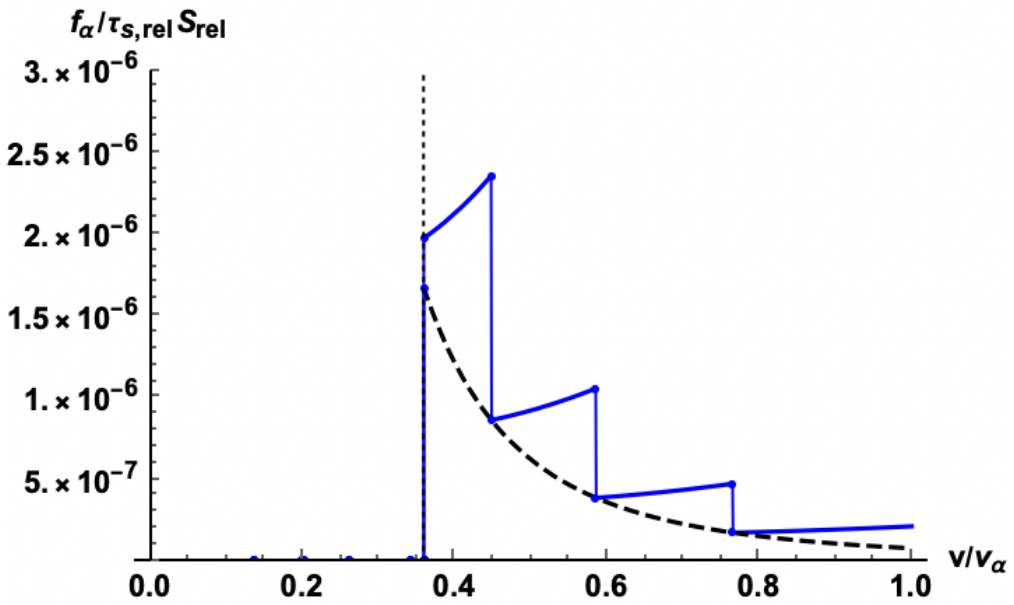

Fig. 3.8 Time dependent distribution function as a function of normalized velocity at time $t^* = 5.5\tau_{saw}$, obtained varying both τ_{sd} and source term. The distribution function is plotted up to the critical velocity showed with vertical dotted line. The new time dependent distribution function (solid blue) is shown for ratio $\tau_{sd0}/\tau_{saw} = 3$, together with the slowing down obtained for a constant slowing-down time $\tau_{sd,rel}$ (dashed black). The combination of the two effects lead to a distribution function with piecewise $\partial f/\partial v > 0$.

Additionally, we highlighted the crucial role played by the equilibrium distribution function in velocity space for $n = 0$ modes.

The chapter concluded with the derivation, using the simplified Fokker-Plank equation, of various distribution functions that could serve as a source of free energy for $n = 0$ modes resonating with energetic ions.

Fast-ion distribution function with positive slope in velocity space can be obtained through losses, velocity space anisotropy and due to two effects associated with temperature oscillations during the sawtooth dynamics, discussed in our work for the first time [14].

Chapter 4

Vertical modes

As previously mentioned, the primary focus of this work is to investigate the stability of axisymmetric toroidal modes characterized by the toroidal mode number $n = 0$. Specifically, our analysis aims to describe the interaction between $n = 0$ vertical displacement oscillations resulting from the stabilization of the ideal vertical instability and the presence of fast ions.

To achieve this goal, it is imperative to first establish a rigorous and comprehensive description of vertical stability within the ideal MHD model. This represents the basis for studying how the plasma stability is influenced by superthermal particles, following the procedure of Sec. 3.2.1. Therefore, this chapter is dedicated to the ideal MHD examination of vertical stability in tokamak plasmas, with the objective of deriving a dispersion relation that characterizes the oscillatory modes induced by the stabilization of the ideal vertical instability.

The content of this chapter is based on the results published in Ref. [15].

4.1 Plasma vertical stability - Heuristic

A simple heuristic model, which features currents flowing in three parallel rectilinear wires, helps us to understand the mechanism and timescales of the vertical instability. This well-known toy model has been discussed in the literature, and a straightforward derivation of the dispersion relation for the ideal wall scenario can be found in

references such as [56–58]. For the reader's convenience, this calculation is reported here, along with its extension to the case of a resistive wall.

Referring to Fig. 4.1, consider the *vertical* direction denoted by y. The currents flow along the z direction, mimicking the toroidal direction of a tokamak plasma. The two "external" currents, I_{Ext}, are equal and positive, fixed at $y = \pm l$, while the "plasma" current, I_p, can drift along the vertical direction. Vacuum surrounds the three wires. It's evident that $y = 0$ is an unstable equilibrium point for the plasma wire. Also depicted in Fig. 1 are magnetic X-points located at $y = \pm l_y < l$.

The equation of motion for the plasma wire is

$$\mu_m \ddot{y} = \frac{4 I_P I_{Ext}}{c^2} \frac{y}{l^2 - y^2}, \tag{4.1}$$

with μ_m the linear mass density, c the speed of light, and an over-dot denotes time derivative (c.g.s. units have been adopted). Neglecting self and mutual induction currents, I_P and I_{Ext} remain constant as the plasma wire is displaced. For small $y \ll l$, the solution of Eq. (4.1) is $y = y_0 \, \mathrm{e}^{\gamma_H t}$, where y_0 is an initial displacement, and $\gamma_H = (1/l)(4 I_P I_{Ext}/\mu_m c^2)^{1/2}$.

Instead of a plasma wire, consider a vertically elongated plasma with uniform current density extending up to an elliptical magnetic surface with a minor semi-axis a and a major semi-axis b. According to the analysis in Ref. [59], a relationship is established involving the currents I_P and I_{Ext} and the distance l: $I_{Ext}/I_P = [(b-a)/(b+a)][l^2/(a^2+b^2)]$. With this expression, γ_H depends solely on the plasma current I_P and the semi-axes a and b, being independent of I_{Ext} and l. Additionally, μ_m can be replaced by $\mu_m \to \pi a b \rho_m$, where ρ_m is the volume mass density. After straightforward algebra, and considering the limit of small ellipticity, $e_0 \ll 1$, where

$$e_0 = \frac{b^2 - a^2}{b^2 + a^2}, \tag{4.2}$$

the growth rate can be written as:

$$\gamma_H = {e_0}^{1/2} {\tau_A}^{-1}, \tag{4.3}$$

where ${\tau_A}^{-1} = {B_P}'/(4\pi\rho_m)^{1/2}$ is the inverse Alfvén time, and ${B_P}'$ is the radial derivative of the poloidal magnetic field on the magnetic axis. Note that, for a circular plasma cross-section, $e_0 = 0$ and the growth rate γ_H vanish. Considering typical

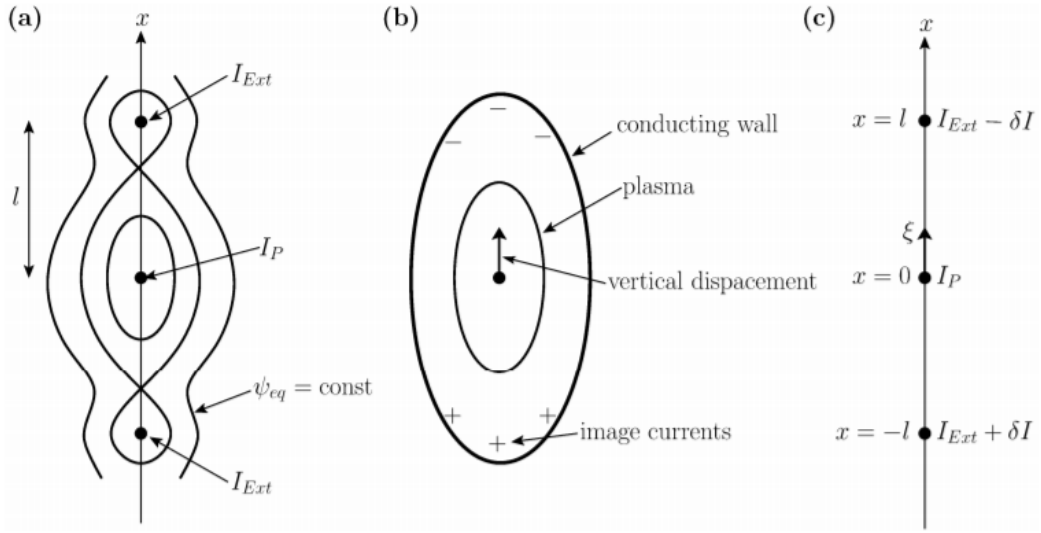

Fig. 4.1 Schematic diagram of the heuristic model for vertical instability.

values of present-day tokamak experiments, γ_H^{-1} is indeed a fast growth time of the order of a few microseconds.

A perfectly conducting wall can offer passive feedback stabilization of the vertical instability. The stabilization mechanism is described as follows: when the plasma undergoes displacement from its equilibrium position, image currents are induced at the wall. The direction of these currents is such that the resulting net force opposes the motion of the plasma wire. In the heuristic model, this effect can be modeled by assuming two currents of opposite sign, $\pm\delta I$, proportional to the displacement of the plasma column and localized at $y = \pm l$. Then,

$$L\delta\dot{I} = LDI_{Ext}\dot{y}/l, \tag{4.4}$$

where L is an effective inductance and D is a dimensionless proportionality constant, which, in the case of a tokamak plasma, can be determined in terms of the wall geometry. Taking the limit $y \ll l$, the equation of motion modified by the feedback currents becomes:

$$\mu_m c^2 \ddot{y} \approx 4 I_P I_{Ext} (1 - D) y/l^2 \tag{4.5}$$

The vertical instability is thus suppressed for $D > 1$. In the actual tokamak case, this corresponds to a criterion related to the plasma boundary-wall distance. When the feedback currents succesfully stabilize the plasma wire, Eq. (4.5) implies that it

oscillates vertically with frequency

$$\omega = \pm\omega_H = \pm\sqrt{D-1}\,\gamma_H. \tag{4.6}$$

These two solutions with frequency $\omega = \pm\omega_H$ are a first indication of what we dub "vertical displacement oscillatory modes", or VDOM.

For the more realistic case of a resistive wall, equation (4.4) is modified into

$$R\delta I + L\delta\dot{I} = LDI_{Ext}\dot{y}/l. \tag{4.7}$$

After straightforward algebra, and again in the limit $y \ll l$, we find

$$\mu_m c^2\,\dddot{y} = 4I_P I_{Ext}\dot{y}/l^2 - 4I_P\dot{\delta I}/l. \tag{4.8}$$

Eliminating $\dot{\delta I}$, we obtain the third-order differential equation for y:

$$\dddot{y} + \frac{1}{\tau_R}\ddot{y} + \omega_H^2\dot{y} - \frac{1}{\tau_R}\frac{\omega_H^2}{D-1}y = 0 \tag{4.9}$$

where $\tau_R = L/R$ is the resistive wall penetration time.

We consider the limit $D > 1$, where the ideal vertical instability is suppressed. Looking for solutions of the type $y(t) \sim y_0 e^{\gamma t}$, a cubic dispersion relation for complex γ is obtained:

$$\gamma^3 + \frac{1}{\tau_R}\gamma^2 + \omega_H^2\gamma - \frac{1}{\tau_R}\frac{\omega_H^2}{D-1} = 0, \tag{4.10}$$

where ω_H is defined in Eq. (4.6). In the regime of low wall resistivity, where $\omega_H\tau_R \gg 1$, the two VDOM oscillatory roots observed in the ideal wall scenario are damped. If we set $\gamma = -i\omega$, these damped modes exhibit a complex frequency:

$$\omega = \pm\omega_H - \frac{iD}{2(D-1)\tau_R}. \tag{4.11}$$

A third root is obtained, corresponding to a resistive instability with growth rate

$$\gamma = \frac{1}{(D-1)\tau_R} \equiv \gamma_R. \tag{4.12}$$

For this non-rotating, unstable mode, the inverse growth rate scales with τ_R. Given typical tokamak parameters, the growth time is of the order of a few milliseconds.

To mitigate the growth of the resistive wall instability, active feedback control involving currents external to the tokamak vacuum chamber can be used [60–63]. It is important to note that as long as the VDOM remains damped, it is not expected to impact the active stabilization system applied to this $n = 0$ resistive wall mode.

In the following the study of the ideal-MHD normal mode problem applied to $n = 0$ perturbations results in a more general dispersion relation. In the limit of small ellipticity, this general dispersion relation reduces to the heuristic model result of (4.10), confirming its validity.

4.2 Vertical modes

The analysis in this section is reported in our publications, as referenced in Refs. [15, 64, 57, 65]. The vertical instability is appropriately modeled using the reduced ideal-MHD model [66] derived from the Eqs. (3.9-3.14), which is well-established for normal-mode analysis. For axisymmetric modes, the influence of toroidal effects is negligible, and thus, the analysis adopts the "straight tokamak" approximation. The magnetic field is $\mathbf{B} = \mathbf{e}_z \times \nabla\psi + B_z \mathbf{e}_z$, where $\mathbf{e}_z$ is the unit vector along the ignorable z-direction, which mimics the toroidal coordinate, and B_z is constant. The plasma flow is $\mathbf{v} = \mathbf{e}_z \times \nabla\varphi + v_z \mathbf{e}_z$. In the standard low-$\beta$ limit for a tokamak plasma, the fields B_z and v_z decouple from the fields ψ and φ. Therefore, the magnetic flux function, ψ, and the stream function, φ, obey the model equations [66]:

$$\frac{\partial \psi}{\partial t} + [\varphi, \psi] = 0, \tag{4.13}$$

$$\frac{\partial}{\partial t} \nabla \cdot (\rho \nabla\varphi) + [\rho, (\nabla\varphi)^2] + [\varphi, \rho] U + [\varphi, U] = [\psi, J]\,. \tag{4.14}$$

In these equations, all quantities are dimensionless, brackets are defined as $[\chi, \eta] = \mathbf{e}_z \cdot \nabla\chi \times \nabla\eta$, $J = \nabla^2\psi$ is the normalized current density, and $U = \nabla^2\varphi$ is the normalized flow vorticity. Space and time are normalized as $\hat{r} = r/r_0$, where $r_0 = ab/[(a^2 + b^2)/2]^{1/2}$ is a convenient equilibrium scale length, and $\hat{t} = t/\tau_A$, where τ_A is the poloidal Alfvén time defined below Eq. (4.3). The dimensionless fields are normalized as $\hat{\psi} = \psi/(B_p{}' r_0^2)$, $\hat{\varphi} = (\tau_A/{r_0}^2)\varphi$; the plasma density is normalized to its on-axis value, $\hat{\rho} = \rho_m/\rho_{m0}$, and the current density is $\hat{J} = (4\pi/cB_p{}')J_z$. In order

to simplify the notation, over-hats are actually dropped in Eqs. (4.13) and (4.14), and in the following.

At equilibrium, fields are stationary, and, by assumption, the equilibrium plasma velocity is neglected. The current density, J_{eq}, is assumed to be uniform up to an elliptical boundary with minor semi-axis a and major semi-axis b. Beyond this boundary, in the vacuum region, the current density drops to zero. It is important to note that the elliptical boundary must correspond to a magnetic flux surface, located within the region delimited by the magnetic separatrix. In elliptical coordinates (μ,θ), where $x = A\sinh(\mu)\cos(\theta)$ and $y = A\cosh(\mu)\sin(\theta)$, with $A = \sqrt{b^2-a^2}$, the elliptical boundary corresponds to $\mu = \mu_b$, such that $a = A\sinh\mu_b$ and $b = A\cosh\mu_b$. The equilibrium current density is $J_{eq}(\mu) = 2H(\mu_b - \mu)$, where $H(x)$ is the Heaviside unit step function.

Inside the elliptical boundary, where $\mu < \mu_b$ and $\psi = \psi^-_{eq}$, the solution of $\nabla^2\psi^-_{eq} = 2$ can be easily written in terms of Cartesian components, following the analysis of Ref.[59]:

$$\psi^-_{eq}(x,y) = \frac{1}{2}\left(\frac{x^2}{b^2} + \frac{y^2}{a^2}\right). \tag{4.15}$$

In the vacuum region outside the elliptical boundary, where $\mu > \mu_b$, the equilibrium flux $\psi_{eq} = \psi^+_{eq}$ satisfies $\nabla^2\psi^+_{eq} = 0$. The superscripts "$-$" and "$+$" indicate the plasma and vacuum regions, respectively. Assuming no equilibrium current sheets, the continuity of ψ_{eq} and its derivative along the normal to the boundary must be maintained across the boundary. The relevant analytic solution is

$$\psi^+_{eq}(\mu,\theta) = \frac{1}{2} + \alpha^2\left\{\mu - \mu_b + \frac{e_0}{2}\sinh\left[2(\mu-\mu_b)\right]\cos(2\theta)\right\} \tag{4.16}$$

with $\alpha^2 = ab/r_0^2$ and e_0 the ellipticity parameter defined in Eq. (4.2). Magnetic flux surfaces $\psi_{eq}(\mu,\theta) = \text{const}$ exhibit a magnetic separatrix at $\psi_{eq}(\mu,\theta) = \psi_X = \mu_b\,\alpha^2$, with X-points located at $\mu = \mu_X = 2\mu_b$ and $\theta = \theta_X = \pi/2 \pm n\pi$.

Also the equilibrium plasma density profile is assumed to be uniform up to the elliptical boundary $\mu = \mu_b$, with $\rho_{eq} = H(\mu_b - \mu)$. This model equilibrium describes a plasma that terminates well before the magnetic separatrix. The equilibrium magnetic X-points lie either outside the plasma containment chamber, or in the vacuum region.

The choice of this specific equilibrium is justified by two main reasons. Firstly, we aim to conduct a fully analytic treatment of the normal-mode problem, which is more convenient with a relatively simple equilibrium. Secondly, based on prior investigations of the vertical stability problem, the effects associated with gradients of the equilibrium plasma current density are expected to play a minor role. It's worth noting that the equilibrium used in this article aligns with that employed in Ref. [67].

For stability considerations, set $\psi(\mu,\theta,t) = \psi_{eq}(\mu,\theta) + \tilde{\psi}(\mu,\theta)\,\mathrm{e}^{\gamma t}$ and $\varphi(\mu,\theta,t) = \tilde{\varphi}(\mu,\theta)\,\mathrm{e}^{\gamma t}$, where the over-tilde denotes small perturbed quantities and $\gamma = -i\omega$. The linearized version of Eqs. (4.13) and (4.14) is

$$\gamma\tilde{\psi} + \left[\tilde{\varphi}, \psi_{eq}\right] = 0, \tag{4.17}$$

$$\gamma\nabla\cdot(\rho_{eq}\nabla\tilde{\varphi}) = \left[\tilde{\psi}, J_{eq}\right] + \left[\psi_{eq}, \tilde{J}\right]. \tag{4.18}$$

In the region $\mu < \mu_b$, the stream function corresponding to a rigid vertical shift is represented in elliptical coordinates by

$$\tilde{\varphi}(\mu,\theta) = \gamma\xi\, a\frac{\sinh\mu}{\sinh\mu_b}\cos\theta. \tag{4.19}$$

where ξ is the vertical displacement of the plasma column. From the flux freezing condition (5.4) we obtain the corresponding perturbed magnetic flux:

$$\tilde{\psi}^{-}(\mu,\theta) = -\frac{\xi}{b}\frac{\cosh\mu}{\cosh\mu_b}\sin\theta \tag{4.20}$$

Since $\tilde{U}$, $\tilde{J}$, $\nabla\rho_{eq}$ and ∇J_{eq} all vanish inside the elliptical boundary, Eq. (4.18) is trivially satisfied. Note that in elliptical coordinates, $\nabla^2\chi = h^{-2}(\partial^2\chi/\partial\mu^2 + \partial^2\chi/\partial\theta^2)$, where $h = 1/|\nabla\mu| = 1/|\nabla\theta|$ is a scale factor, with $h^2 = A^2(\cosh 2\mu + \cos 2\theta)/2$.

When an ideal or resistive wall is present, the rigid-shift solutions (4.19) and (4.20) for the stream function and the perturbed flux in the plasma region remain valid. In the vacuum region, the perturbed flux satisfies $\nabla^2\tilde{\psi}^{+} = 0$, and its solution can be represented as

$$\tilde{\psi}^{+}(\mu,\theta) = -\frac{\xi_\infty}{b}\exp\left[-(\mu-\mu_b)\right]\sin\theta + \frac{\xi_{ext}}{b}\frac{\cosh\mu}{\cosh\mu_b}\sin\theta. \tag{4.21}$$

In this expression, ξ_∞ represents the amplitude of the rigid vertical displacement in the scenario where the wall is moved to infinity. The term proportional to ξ_{ext} accounts for the contribution to the perturbed flux arising from image currents generated on the wall when it is at a finite distance from the plasma boundary. Flux continuity at the plasma boundary implies that $\xi = \xi_\infty - \xi_{ext}$, resulting in the reduction of the actual vertical displacement ξ compared to the no-wall case by the amount ξ_{ext}. Consequently, a perturbed current sheet forms at the plasma boundary:

$$\tilde{J}(\mu,\theta) = \tilde{j}_b(\theta)\delta(\mu-\mu_b) = \frac{1}{h^2}\left(\frac{\partial\tilde{\psi}^+}{\partial\mu} - \frac{\partial\tilde{\psi}^-}{\partial\mu}\right)\Bigg|_{\mu_b}\delta(\mu-\mu_b), \tag{4.22}$$

where $\delta(x)$ is the Dirac delta function. A staightforward calculation yields the ellipitical-angle modulation of the current sheet:

$$\tilde{j}_b(\theta) = \frac{2(a+b)}{b^2(a^2+b^2)}\frac{\xi_\infty \sin\theta}{1+e_0\cos 2\theta}. \tag{4.23}$$

Note that $\tilde{j}_b(\theta)$ depends only on ξ_∞ and not on ξ_{ext}: the current sheet at the plasma boundary does not depend on the wall.

4.2.1 Dispersion relation

In this subsection, utilizing quadratic forms, we derive a dispersion relation for $n = 0$ vertical modes, dependent on geometric parameters, a and b, and a function, $D_w(\gamma)$, determined by the wall's geometry and resistivity. This function becomes independent of γ in the ideal wall limit.

To accomplish this, we introduce the auxiliary stream function $\tilde{\varphi}^\dagger$, which matches the complex-conjugate stream function within the plasma volume (up to $\mu = \mu_b + \varepsilon$, including the perturbed current sheet at the plasma boundary). Beyond this region, in the vacuum, $\tilde{\varphi}^\dagger$ is set to zero. Multiplying the perturbed plasma equation of motion (4.18) by $\tilde{\varphi}^\dagger/2\gamma^*$ and integrating over the entire volume up to infinity, we obtain through standard manipulations:

$$-\gamma^2\frac{1}{2}\int_\Omega d^3x\rho_{eq}\xi\cdot\xi^* = -\frac{1}{2}\int_\Omega d^3x\xi^*\cdot\left[(\tilde{\mathbf{J}}\times\mathbf{B}_{eq}) + (\mathbf{J}_{eq}\times\tilde{\mathbf{B}})\right] \tag{4.24}$$

where $\xi = \mathbf{e}_z \times \nabla\tilde{\varphi}/\gamma$ is the displacement vector and Ω denotes the plasma volume. Thus, the dispersion relation can be written as

$$-\gamma^2 = \delta W/\delta I, \tag{4.25}$$

where

$$\delta I = \frac{1}{2}\int_\Omega \rho_{eq}\xi\cdot\xi^* d^3x \tag{4.26}$$

and

$$\delta W = -\frac{1}{2}\int_\Omega \xi^*\cdot F(\xi) d^3x, \tag{4.27}$$

with $F(\xi) = \left[(\tilde{\mathbf{J}}\times\mathbf{B}_{eq}) + (\mathbf{J}_{eq}\times\tilde{\mathbf{B}})\right]$ the force density operator in the low β limit. Straightforward algebra, using $d^3x = h^2 d\theta d\mu dz$, leads to

$$\delta I = \frac{1}{2}\int_\Omega d^3x\rho_{eq}\frac{\nabla\tilde{\varphi}\cdot\nabla\tilde{\varphi}^*}{|\gamma|^2} = \frac{\pi}{2}abL_z\xi^2, \tag{4.28}$$

where L_z is the length of the straight tokamak. Without loss of generality, we can assume ξ to be real, representing the amplitude of the vertical displacement discussed in the previous section. The perturbed energy integral is then given by:

$$\delta W = \frac{1}{2}\int_\Omega d^3x\left(\mathbf{e}_z\times\frac{\nabla\tilde{\varphi}^*}{\gamma^*}\right)\cdot(\tilde{J}\nabla\psi_{eq} + J_{eq}\nabla\tilde{\psi}). \tag{4.29}$$

The last term can be further manipulated, utilizing the results for the perturbed stream function and the perturbed magnetic flux obtained above. The potential energy integral δW can be expressed as the sum of two terms. The first term is:

$$\begin{aligned}&\frac{1}{2}\int_\Omega d^3x\tilde{J}\nabla\psi_{eq}\cdot(\mathbf{e}_z\times\frac{\nabla\varphi^*}{\gamma^*}) = \\ &\frac{L_z}{2}\int_0^{2\pi}d\theta\int_0^{\mu_b+\varepsilon}d\mu h^2\tilde{j}_b(\theta)\delta(\mu-\mu_b)\nabla\psi_{eq}\cdot(\mathbf{e}_z\times\frac{\nabla\varphi^\dagger}{\gamma^*}) = \frac{\pi}{2}\frac{a+b}{b^3}L_z\xi_\infty\xi.\end{aligned} \tag{4.30}$$

The second term can be expressed as

$$\begin{aligned}&\frac{1}{2}\int_\Omega d^3xJ_{eq}\nabla\tilde{\psi}\cdot(\mathbf{e}_z\times\frac{\nabla\varphi^*}{\gamma^*}) = \\ &\frac{L_z}{2}\int_0^{2\pi}d\theta\int_0^{\mu_b+\varepsilon}d\mu h^2 J_{eq}\nabla\tilde{\psi}^-\cdot(\mathbf{e}_z\times\frac{\nabla\varphi^*}{\gamma^*}) = -\frac{\pi}{2}\frac{a^2+b^2}{ab^3}L_z\xi^2.\end{aligned} \tag{4.31}$$

It is convenient to introduce the quantity

$$D_w = \frac{\xi_{ext}}{\hat{e}_0 \xi_\infty}, \tag{4.32}$$

where $\hat{e}_0 = e_0 b/(a+b)$. Then, combining Eqs. (4.30), (4.31) and (4.32), remembering that $\xi = \xi_\infty - \xi_{ext}$, we obtain

$$\delta W = -\frac{\pi}{2} L_z \frac{1-a/b}{ab} \frac{1-D_w}{1-\hat{e}_0 D_w} \xi^2. \tag{4.33}$$

Thus, Eq. (4.25) yields the dispersion relation:

$$\gamma^2 = \frac{1-a/b}{a^2 b^2} \frac{1-D_w}{1-\hat{e}_0 D_w}. \tag{4.34}$$

This dispersion relation is "general," meaning that it is applicable to the three cases of interest: the no-wall limit, the ideal wall case, and the resistive wall case. Wall effects are incorporated in Eq. (4.34) through the single stability parameter, D_w. In Eq. (4.34), parameters a and b are normalized to the scale length r_0 defined below Eq.(4.14). Reintroducing dimensions, the dispersion relation(4.34) takes the form:

$$(\gamma \tau_A)^2 = \frac{r_0^4}{a^2 b^2} \left(1 - \frac{a}{b}\right) \frac{1-D_w}{1-\hat{e}_0 D_w} \tag{4.35}$$

Thus, the stability of the mode is described by the quantity D_w, determined once the location and nature (ideal or resistive) of the wall are established. As demonstrated in the following subsections, for a perfectly conducting wall, D_w is a real, γ-independent quantity that reduces to the parameter D introduced in the heuristic model of Sec. 4.1. In this scenario, the relevant dispersion relation is quadratic in γ, and the sign of γ^2, dependent on the sign of $1 - D_w$, dictates the stability of vertical displacements in the ideal-MHD limit. However, if a resistive wall is considered, then $D_w = D_w(\gamma)$, and the dispersion relation becomes cubic in γ, as discussed in Subsec. 4.2.4.

4.2.2 Wall at infinity

The initial case under investigation is the no-wall limit, or equivalently, the scenario where the wall is positioned at infinity. In this situation, $\xi_{ext} = 0$, resulting in $D_w = 0$.

The vertical mode is unstable, featuring γ^2 as a positive real value (for $b > a$), which diminishes to zero in the circular limit, $a = b$. The growth rate of the mode is given by:

$$\gamma = \frac{r_0^2}{ab}\left(1-\frac{a}{b}\right)^{1/2}\tau_A^{-1} \equiv \gamma_\infty \tag{4.36}$$

γ^2 can also be written in terms of the ellipticity parameter,

$$\gamma^2 = (1-e_0)(1+e_0-\sqrt{1-e_0^2})\tau_A^{-2} \equiv \gamma_\infty^2. \tag{4.37}$$

It's noteworthy that this result holds for arbitrary values of e_0 within the interval $0 \le e_0 \le 1$. In the small ellipticity limit, γ_∞ converges to γ_H in Eq. (4.3), and the mode growth rate coincides with the heuristic result from Sec. 4.1.

4.2.3 Passive feedback stabilization: Ideal wall

Consider the scenario where the wall is described by an elliptical coordinate surface, given by $\mu = \mu_w$, and is confocal to the elliptical plasma boundary located at $\mu = \mu_b$, where $\mu_w \ge \mu_b$. If the wall is ideal, the perturbed flux in Eq. (4.21) must vanish at $\mu = \mu_w$, leading to the condition:

$$\frac{\xi_{ext}}{\xi_\infty} = \frac{e^{-(\mu_w-\mu_b)}\cosh\mu_b}{\cosh\mu_w} = \frac{1+\exp(2\mu_b)}{1+\exp(2\mu_w)}. \tag{4.38}$$

Now, let us use

$$a_w = A\sinh\mu_w, \qquad b_w = A\cosh\mu_w, \tag{4.39}$$

$$a = A\sinh\mu_b, \qquad b = A\cosh\mu_b, \tag{4.40}$$

where $A = \sqrt{b_w^2 - a_w^2} = \sqrt{b^2-a^2}$, with b_w and a_w the major and minor semi-axes of the elliptical wall, respectively. It follows that

$$e^{2\mu_b} = \frac{b+a}{b-a}, \tag{4.41}$$

$$e^{2\mu_w} = \frac{b_w+a_w}{b_w-a_w}, \tag{4.42}$$

Using Eqs. (4.38)-(4.42) and the definition of D_w in Eq. (4.32), we obtain

$$D_w = \frac{b^2 + a^2}{(b-a)^2} \frac{b_w - a_w}{b_w} \equiv D. \tag{4.43}$$

It's worth noting that as the wall is moved further away from the plasma boundary, it tends to become more "circular" due to the assumption of confocality with the elliptical plasma boundary. Consequently, as $b_w/b \to \infty$, we have $b_w \to a_w$ and $D \to 0$. If not for an extra term in the denominator of Eq. (4.34) proportional to $\hat{e}_0$, which becomes negligible for small ellipticity, the dispersion relation (4.34) with $D_w = D$ closely aligns with the heuristic dispersion relation obtained in Sec. 2. When $D > 1$, γ^2 is negative, and the vertical mode oscillates with a real frequency:

$$\omega = \pm\omega_0 = \pm \left[\frac{D-1}{1-\hat{e}_0 D}\right]^{1/2} \gamma_\infty, \tag{4.44}$$

which reduces to ω_H defined in Eq. (4.6) in the limit of small ellipticity. The quadratic nature of the dispersion relation indicates that, in the limit of $D > 1$, only the Vertical Displacement Oscillatory Modes (VDOM) solutions can be identified. Consequently, an ideal elliptical wall, confocal with the elliptical plasma boundary, can passively stabilize the vertical instability when $D_w = D > 1$. The maximum value of D occurs when the wall and the plasma boundary coincide, $\mu_w = \mu_b$, yielding $D = D_{\max} = (a+b)/(e_0 b)$. As an example, consider $a_w = a$, $b_w = b$, and $b/a = 1.8$, leading to $D_{\max} \approx 2.9$. It's noteworthy that as $\mu_w \to \mu_b$, the vertical oscillatory modes has a frequency approximately given by $\omega \approx \pm[(D_{\max}-1)/1-\hat{e}_0 D_{\max}]^{-1/2}\gamma_\infty$. At the same time, the amplitude of the displacement, $\xi = \xi_\infty - \xi_{\text{ext}}$, tends to zero as $\xi_{\text{ext}} \to \xi_\infty$. As the wall is moved farther from the plasma boundary, the value of D monotonically decreases, and a purely oscillatory solution persists as long as D remains greater than unity.

It can be verified through Eqs.(4.38)-(4.42) that the critical stability threshold, $D = 1$, is reached when $\mu_w = 2\mu_b$, signifying that the elliptical wall intersects the X-points. Consequently, our model suggests that values of $D < 1$, where passive feedback stabilization is not feasible, occur when the X-points are situated within the volume bounded by the wall. This outcome aligns with the findings of Laval et al.[67], derived from the ideal-MHD energy principle. However, this conclusion is specific to the case of confocal wall and plasma boundaries. For different wall shapes that closely match the plasma boundary, passive feedback stabilization due

to the ideal wall may not demand the X-points to be positioned beyond the wall. Moreover, in actual tokamak plasmas, additional coils and/or short-circuited plates within the vacuum chamber can contribute to passive feedback stabilization [63, 62]. Lastly, as demonstrated in Refs. [57, 65], if the plasma extends to the magnetic separatrix, typical for a divertor tokamak plasma, axisymmetric plasma currents linked to vertical displacement perturbations are induced near the magnetic X-points. Consequently, these currents can also play a role in the passive feedback stabilization of the vertical instability.

4.2.4 Passive feedback stabilization: Resistive wall

Finally, we consider the more realistic scenario of a resistive wall. In this case, the perturbed magnetic flux is not constrained to be zero at the wall and can diffuse across the resistive wall on the timescale of wall resistivity. We can distinguish three different regions: inside the elliptical boundary, $\mu \leq \mu_b$, where the perturbed flux $\tilde{\psi}$ is given by $\tilde{\psi}^-$ as defined in Eq. (4.20). In the vacuum region between the plasma boundary and the wall, $\mu_b \leq \mu \leq \mu_w$, where $\tilde{\psi}$ is given by $\tilde{\psi}^+$ as defined in Eq. (4.21). In the vacuum outside the wall, where $\tilde{\psi} = \tilde{\psi}_{out}$ is the solution of $\nabla^2 \tilde{\psi}_{out} = 0$ that decays to zero at infinity. Focusing on vertical displacements with elliptical mode number $m = 1$, the relevant solution for the third region is given by:

$$\tilde{\psi}_{out}(\mu, \theta) = \psi_0 e^{-(\mu - \mu_w)} \sin\theta \qquad \text{for } \mu \geq \mu_w + \delta_w, \tag{4.45}$$

where δ_w is a small parameter representing the average width of the thin wall.

Two conditions at the wall determine the parameters ψ_0 and D_w. The first condition is the continuity of flux at the wall, expressed as $\tilde{\psi}^+(\mu_w, \theta) = \tilde{\psi}_{out}(\mu_w, \theta)$, which yields:

$$\psi_0 = -\frac{\xi_\infty}{b} e^{-(\mu_w - \mu_b)} + \frac{\xi_{ext}}{b} \frac{\cosh\mu_w}{\cosh\mu_b}. \tag{4.46}$$

The second condition is related to the current flowing along the wall. Considering the resistive Ohm's law for the perturbed magnetic flux within the wall, expressed as $\partial \psi w / \partial t = (\eta c^2 / 4\pi) \nabla^2 \psi w$, where η is the wall resistivity, after proper normalization, we get:

$$\nabla^2 \tilde{\psi}_w = \frac{\gamma}{\varepsilon_\eta} \tilde{\psi}_w \tag{4.47}$$

where $\varepsilon_\eta = (\eta \tau_A c^2)/(4\pi r_0^2)$ is the inverse of the relevant dimensionless Lundquist number. If the wall is relatively thin, we can neglect the dependence on μ of the perturbed flux at the right-hand side of Eq.(4.47). This approximation is similar to the standard constant-ψ approximation used in magnetic reconnection theory. Let $\tilde{\psi} = \hat{\psi}(\mu)\sin\theta$. We assume the ordering $\partial_\mu^2 \hat{\psi} \sim \hat{\psi}/(\mu_w \delta_w) \gg \hat{\psi}$. Then, Eq.(4.47) can be approximated as:

$$\frac{d^2\hat{\psi}}{d\mu^2} = h^2 \frac{\gamma}{\varepsilon_\eta}\psi_0. \tag{4.48}$$

Integrating across the thin wall,

$$\int_{\mu_w}^{\mu_w+\delta_w} \frac{d^2\hat{\psi}}{d\mu^2} d\mu = \int_{\mu_w}^{\mu_w+\delta_w} h^2 \frac{\gamma}{\varepsilon_\eta}\psi_0 d\mu. \tag{4.49}$$

The scale factor h is defined below Eq. (4.20). In a more precise sense, h has dependencies on both μ and θ. However, under the assumption of small wall ellipticity, which is considered in the subsequent analysis, the modulation of h along the wall in the θ direction is negligible. Therefore, we can make the approximation $h(\mu_w, \theta) \approx b_w$. Performing the integration, the result is:

$$\left(\frac{d\hat{\psi}_{out}}{d\mu} - \frac{d\hat{\psi}^+}{d\mu}\right)\Bigg|_{\mu_w} = \frac{\gamma \delta_w b_w^2}{\varepsilon_\eta}\psi_0, \tag{4.50}$$

or equivalently

$$-\frac{\xi_\infty}{b} e^{-(\mu_w - \mu_b)} - \frac{\xi_{ext}}{b}\frac{\sinh\mu_w}{\cosh\mu_b} = \left(1 + \frac{\gamma\delta_w b_w^2}{\varepsilon_\eta}\right)\psi_0. \tag{4.51}$$

Eqs. (4.46) and (4.51) are two equations that can be used to determine the two parameters, $\psi_0 \propto \xi_\infty$, and $\xi_{ext}/\xi_\infty \propto D_w$, cf. (4.32). After straightforward algebra, we obtain

$$D_w(\gamma) = D\frac{\gamma\tau_\eta}{1+\gamma\tau_\eta}, \tag{4.52}$$

and

$$\psi_0 = -\frac{\xi_\infty}{b}\frac{b_w}{(a+b)}\frac{e_0 D}{(1+\gamma\tau_\eta)}. \tag{4.53}$$

In these equations D is the one defined in Eq. (4.38). The term $\tau_\eta = [b_w^3/(a_w + b_w)]\delta_w/\varepsilon_\eta$ represents the resistive wall time, normalized by the relevant Alfvén time. Notably, the stability parameter D_w exhibits dependence on γ due to the finite wall

resistivity. As τ_η tends to infinity in the ideal wall limit, $D_w(\gamma)$ reduces to D, the parameter discussed in subsection 4.2.3. Additionally, Eq.(4.53) indicates that the perturbed flux at the wall tends to zero in the ideal wall limit, as expected.

Substituting $D_w(\gamma)$ in Eq. (4.34), one obtains the dispersion relation for vertical displacements in the case of feedback stabilization via a resistive wall:

$$\gamma^3 + \gamma^2 \frac{1}{\tau_\eta} \frac{1}{1-\hat{e}_0 D} + \gamma\omega_0^2 + \omega_0^2 \frac{1}{\tau_\eta} \frac{1}{1-D} = 0 \tag{4.54}$$

with ω_0 defined in Eq. (4.44). The agreement between Eq.(4.54) and the heuristic dispersion relation from Sec. 4.1, specifically Eq.(4.10), is notable. This agreement holds particularly well in the limit of small ellipticity, where the term $\hat{e}_0 D$ becomes negligible, and ω_0 reduces to ω_H as shown in Eq. (4.6).

In the realistic limit where $\omega_0 \tau_\eta \gg 1$, the three roots of this cubic dispersion relation can be easily determined. For $D > 1$, the solutions are two damped oscillatory roots and an unstable growing solution, given by:

$$\omega = \pm\omega_0 - i \frac{1}{2\tau_\eta} \frac{D(1-\hat{e}_0)}{(D-1)(1-\hat{e}_0 D)} \tag{4.55}$$

$$\gamma = \frac{1}{(D-1)\tau_\eta} \tag{4.56}$$

The two weakly damped oscillatory roots found in Eq.(4.55) correspond to the two VDOM, oscillating with a frequency slightly below the poloidal Alfvén frequency. The presence of a resistive wall introduces a small damping rate on the order of the inverse resistive wall time. The third root, as given by Eq.(4.56), represents an unstable mode that grows on the resistive wall time-scale. Typical values for the resistive wall time in tokamak devices are on the order of a few milliseconds. As previously mentioned in Section 4.1, due to its slow growth, this non-rotating, unstable mode is typically suppressed using active feedback control systems [63].

4.2.5 Dispersion relation close to marginal stability

In this subsection we focus on the result of Eq.4.56, which presents the linear growth rate for the standard $n = 0$ resistive wall mode. The results discussed in the following have been published in Ref. [16]. During the linear instability phase, away from

the marginal stability boundary, the vertical displacement grows on the resistive wall time, $\tau_{\eta w}$. However, for the derivation of the parameter D_w, we assume that the current induced on the wall can diffuse and become nearly uniform across the wall within the mode growth time. The time it takes for the induced current to diffuse across the wall of thickness δ_w can be estimated as $\tau_{\text{diff}} \sim \delta_w^2/\mathscr{D}m$, where $\mathscr{D}_m = \eta c^2/4\pi$ represents the resistive diffusion coefficient. The induced current achieves near uniformity across the wall if $\tau\text{diff} \ll \gamma^{-1} \sim \tau\eta w$. This condition is automatically fulfilled in the relevant limit $\delta_w \ll a_w$.

At ideal-MHD marginal stability, when $D = 1$ and the third term of the dispersion relation (4.54) vanishes, a dominant balance for the unstable root emerges involving the first and last terms of Eq. (4.54). This balance yields:

$$\gamma \approx \frac{\gamma_\infty}{(1-\hat{e}0)^{1/3}(\gamma\infty\tau_{\eta w})^{1/3}} = \frac{(a_w/\delta_w)^{1/3}\gamma_\infty}{(1-\hat{e}0)^{1/3}(\gamma\infty\tau_\eta)^{1/3}} \tag{4.57}$$

The growth rate in this regime scales as the one-third power of the wall resistivity. It is considerably larger than the growth rate (4.56) of the standard $n = 0$ resistive wall mode (in the limit where D is positive and $D - 1 = O(1)$). The perturbed current density achieves uniformity across the wall if $\delta_w \leq \delta_{diff} \sim (\mathscr{D}m/\gamma)^{1/2} \sim [(\delta_w/a_w)^{1/6}/(\gamma\infty\tau_\eta)^{1/3}]a_w$. This leads to the following inequality for the wall thickness:

$$\delta_w/a_w \leq (\gamma_\infty\tau_\eta)^{-2/5}. \tag{4.58}$$

In these estimates, we have assumed $a_w \sim b_w$. If the inequality (4.58) is not satisfied, the induced perturbed current on the wall by the vertical plasma motion does not achieve uniformity across the wall. Instead, a skin current forms, characterized by a width δ_s that is smaller than the wall width δ_w. In such a scenario, our derivation of the cubic dispersion relation (4.54) needs to be reconsidered.

We can proceed similarly to the previous subsection, but now the integral in Eq. (4.49) extends to the interval between μ_w and $\mu_w + (\delta\mu)s$, where $(\delta\mu)s = \delta s/a_w$, denoted by the subscript "s" for "skin". The derivation of the parameter D_w follows the same procedure, resulting in a form similar to Eq. (4.52), but with the crucial difference that $\tau\eta w$ should be replaced by

$$\tau_{\eta s} = (\delta_s/a_w)\tau_\eta. \tag{4.59}$$

While δ_w represents the physical width of the wall and is a given parameter, δ_s depends on the mode growth rate, hence its value can only be determined after solving the dispersion relation. A reasonable estimate for the skin depth is $\delta_s = (\mathscr{D}m/\gamma)^{1/2}$. Thus, we obtain the dispersion relation (4.54), with $\tau\eta w$ replaced by $\tau_{\eta s} = \alpha_0(\tau_\eta/\gamma)^{1/2}$, where $\alpha_0^2 = [(1+\kappa_w^2)\kappa_w]/[2(1+\kappa_w)]$ represents a wall geometrical factor, and $\kappa_w = b_w/a_w$:

$$\gamma^3 + \frac{\gamma^2}{\alpha_0(1-\hat{e}0D)(\tau\eta/\gamma)^{1/2}} + \gamma\gamma_\infty^2\frac{D-1}{1-\hat{e}_0 D} - \quad -\frac{\gamma_\infty^2}{\alpha_0(1-\hat{e}0D)(\tau\eta/\gamma)^{1/2}} = 0.$$

The relevant dispersion relation is no longer cubic in γ. However, the relevant unstable root in the limit $D = 1$ and $\gamma_\infty\tau_{\eta s} \gg 1$ can be obtained by balancing the first and the last term of Eq. (**??**):

$$\gamma \approx \frac{\gamma_\infty}{[\alpha_0(1-\hat{e}_0)]^{2/5}(\gamma_\infty\tau_\eta)^{1/5}}. \tag{4.60}$$

Thus, a growth rate that scales with the one-fifth power of the wall resistivity and independent of the wall thickness δ_w is obtained when inequality (4.58) is not satisfied. The growth rate (4.60) exceeds the growth rate (4.57). The two growth rates match, as expected, when $\delta_w/a_w \sim (\gamma_\infty\tau_\eta)^{-2/5}$. In these asymptotic relations, we have assumed α_0 and $(1-\hat{e}_0)$ to be of the order of unity.

In regimes away from marginal stability, the resistive wall vertical displacement grows with a characteristic time of approximately $\tau_{\eta w} = (\delta_w/a_w)\tau_\eta$ (cf. Eq. (4.56)). For typical parameter values such as $\tau_\eta \sim 0.1$s and $\delta_w/a_w \sim 10^{-2}$, the resistive growth time is on the order of $\tau_{\eta w} \sim 1$ ms. This duration is significantly longer compared to the ideal-MHD growth time. Near ideal-MHD marginal stability, $D \approx 1$, the resistive wall vertical displacement can grow much faster. Let us first estimate the growth rate in the thin wall limit. With the parameter values declared above, $\gamma_\infty\tau_{\eta w} \sim 10^3$ and, using the growth rate in Eq. (4.57), $\gamma^{-1} \sim 10\mu$s. The thin wall limit, Eq. (4.58), is marginally satisfied for the value of $\delta_w/a_w \sim 10^{-2}$ declared above, since $(\gamma_\infty\tau_\eta)^{-2/5} \sim 10^{-2}$. The inverse growth rate in the regime where skin currents are induced on the wall, i.e., using the growth rate in Eq. (4.60), also gives $\gamma^{-1} \sim 10\mu$s. In Fig. 4.2, we present a numerical solution of the dispersion relation (4.54) focusing on the unstable root. The plot ranges from $D = 0.9$ to 1.1. Whether the thin wall limit, or the induced skin current regime, apply in real tokamak

experiments depends on a more accurate evaluation of the parameters δ_w/a_w and $\gamma_\infty \tau_\eta$.

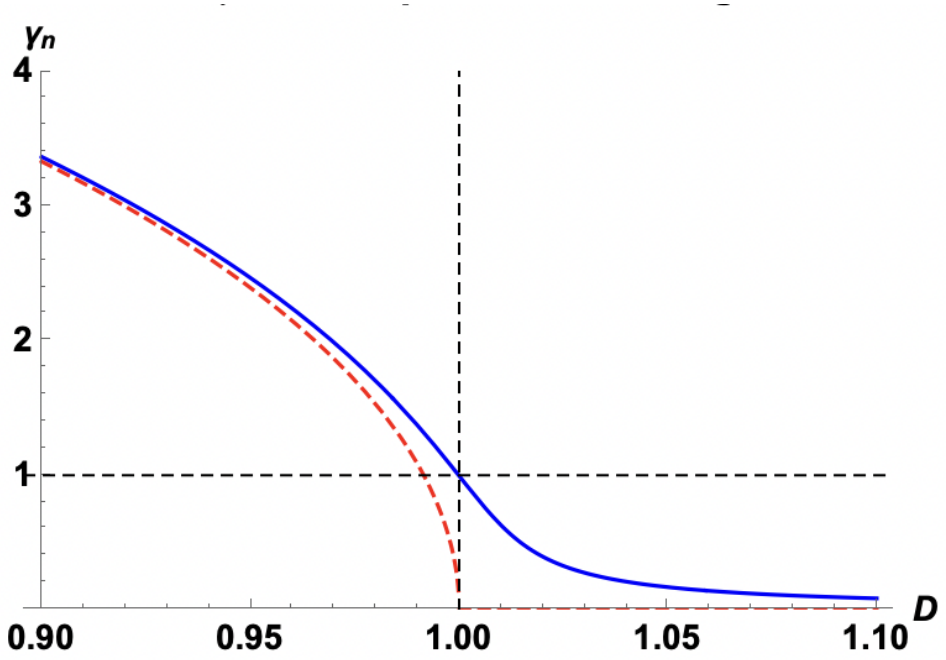

Fig. 4.2 Growth rate γ_n, normalized to the thin wall limit growth rate in Eq. (4.57), as function of the ideal wall parameter D close to ideal marginal stability. The blue curve shows the numerical solution of the full cubic dispersion relation (Eq. 4.54), while the dashed red line represents the ideal wall solution.

4.3 Oscillatory modes: VDOM

In this section, we aim to underscore the key characteristics of the oscillatory Vertical Displacement Oscillatory Modes (VDOM), which represent the primary focus of this study and have received relatively little attention in the context of the vertical stability dispersion relation in the past.

VDOM manifest as axisymmetric modes in a toroidal tokamak plasma, characterized by a toroidal mode number $n = 0$. These modes induce an up–down motion of the entire plasma column and are predominantly composed of Fourier components with an elliptical mode number $m = 1$. Due to the symmetry of the up–down motion, the perturbed streamfunction exhibits even symmetry with respect to the elliptical angle θ (with $\theta = 0$ corresponding to the horizontal direction), while the perturbed

magnetic flux displays odd symmetry with respect to θ. Our derivation is obtained in the reduced ideal-MHD model and made use of a 'straight-tokamak' equilibrium assumption, which considers a simplified elliptical plasma boundary and a uniform current density profile.

The method of quadratic forms, coupled with the normal-mode solution describing the mode structure, proves to be a convenient approach for deriving the relevant dispersion relation. The obtained dispersion relation involves a parameter denoted as $D_w(\gamma)$, which is a function of the complex mode eigenvalue $\gamma = -i\omega$ in the case of plasma confined by a resistive wall, as indicated in Eq.(4.52). Notably, D_w reduces to a constant parameter D in the ideal wall limit, as evident from Eq.(4.43). Moreover, in the scenario where the wall is moved to infinity (no-wall case), D tends to 0. Consequently, the relevant dispersion relation assumes a quadratic form in γ for the ideal wall case, including the no-wall limit. In contrast, for the case of a resistive wall, the dispersion relation becomes cubic in γ, introducing an additional root compared to the ideal wall scenario.

Two roots are present both for the ideal and resistive wall cases. They are associated to vertical plasma modes, referred to as VDOM, that exhibit purely oscillatory behavior in the presence of an ideal wall, provided the parameter $D > 1$. This condition gives a limit on the distance of the ideal wall from the plasma for a given ellipticity. Additionally, these oscillatory modes are weakly damped when wall resistivity is considered, as described in Eq. (4.55). Figure 4.3 illustrates the dispersion relation for the case of an ideal wall surrounding the plasma, showing the growth rate (or frequency) as a function of plasma elongation $\kappa = b/a$ for various wall positions. The regions with positive $(\omega\tau_A)^2$ correspond to stable VDOM, where $D > 1$ is satisfied.

4.4 Concluding remarks

In this chapter, a new theoretical description of plasma stability against vertical displacements in the Ideal MHD limit has been presented. The focus is on the stable branch of the cubic dispersion relation obtained when considering a resistive wall that provides passive feedback stabilization for the vertical instability. While previous works primarily addressed the purely growing $n = 0$ resistive wall mode, which requires active feedback systems for stabilization, relatively little attention has been

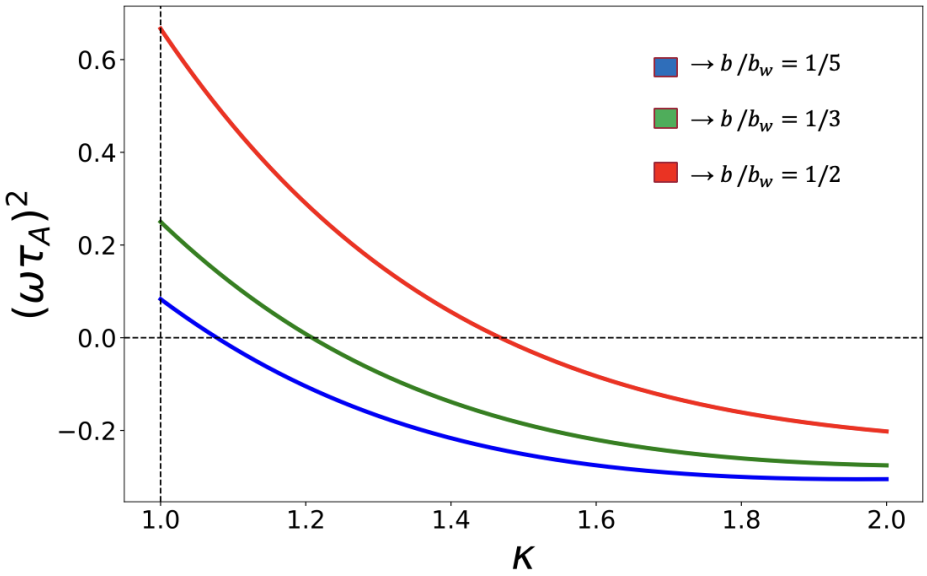

Fig. 4.3 Normalized frequency as a function of the plasma elongation $\kappa = b/a$ for different positions of a confocal ideal wall surrounding the plasma.

given to the stable branch resulting from the ideal vertical instability stabilization. This branch describes stable oscillatory roots, but the investigation in the following will explore the potential destabilization of these stable plasma modes in the presence of energetic ions, suggesting the emergence of a new, interesting, fast ion-driven mode.

Chapter 5

Fast ion drive of n=0 VDOM

The analysis of Ch. 4 showed that Vertical Displacement Oscillatory Modes (VDOM) are natural oscillations of a tokamak plasma in the vertical direction. We established that in the ideal MHD limit, these oscillatory modes exhibit an Alfvénic frequency of oscillation and are damped on the resistive wall timescale, as indicated in Eq. 4.55. In this chapter, our focus shifts to the impact of superthermal particles on the stability of these modes, specifically energetic ions with energies in the MeV range. These ions have bounce or transit frequencies of their orbit in the poloidal plane that are comparable to the VDOM frequency, $\omega_0 \sim \omega_{b,t}$. Wave-particle resonance between these $n = 0$ modes and the superthermal particles can take place.

This chapter, based on the published results of Ref. [17], provides an analytical description of the destabilization of $n = 0$ VDOM due to resonant interactions with fast ions.

5.1 Hybrid kinetic MHD model for vertical modes

The study of the resonant interaction is based on the hybrid kinetic MHD framework described in Sec. 3.2. The effect of superthermal ions on the stability of the VDOM can be studied with the extended energy principle outlined in Sec. 3.2.1. We proceed considering the same model and equilibrium of the previous chapter with the addiction of the fast ion pressure tensor in order to build the quadratic forms constituting δW. The model equations are reported here for convenience.

The two field reduced model in *straight tokamak* approximation used in the previous chapter is considered. The magnetic field is $\mathbf{B} = \mathbf{e}_z \times \nabla\psi + B_z \mathbf{e}_z$, where $\mathbf{e}_z$ is the unit vector along the ignorable z-direction, which mimics the toroidal coordinate, and B_z is constant. The plasma flow is $\mathbf{v} = \mathbf{e}_z \times \nabla\varphi + v_z \mathbf{e}_z$. Equations (4.13,4.14) can be modified with the additional pressure term describing fast ion contributions.

$$\frac{\partial \psi}{\partial t} + [\varphi, \psi] = 0, \tag{5.1}$$

$$\frac{\partial}{\partial t} \nabla \cdot (\rho \nabla \varphi) + [\rho, (\nabla\varphi)^2] + [\varphi, \rho] U + [\varphi, U] = [\psi, J] - e_z \cdot \nabla \times \nabla \cdot \overline{\mathbf{P}}_h. \tag{5.2}$$

where $[\chi, \eta] = \mathbf{e}_z \cdot \nabla\chi \times \nabla\eta$, $J = \nabla^2\psi$ is the current density, and $U = \nabla^2\varphi$ is the flow vorticity. The fast particles pressure tensor is defined as

$$\overline{\mathbf{P}}_h = p_{\perp h}\bar{\mathbf{I}} + (p_\parallel - p_\perp)_h \hat{e_\parallel}\hat{e_\parallel} \tag{5.3}$$

where $e_\parallel = B/B$, $p_{\perp h}$ and $p_{\parallel h}$ are moments of the fast ions distribution function, which obeys the collisionless drift-kinetic equation of Eq. (2.39). The same normalization of Ch. 4 is adopted.

An isotropic fast ions pressure is assumed at equilibrium ($p_{\parallel h,eq} = p_{\perp h,eq} \rightarrow \overline{\mathbf{P}}_{h,eq} = p_{h,eq}\bar{\mathbf{I}}$. The superthermal ions only affect the equilibrium modifying the total scalar pressure as $p_{tot} = p_c + p_{h,eq}$.

To first order in perturbed quantities,

$$\gamma\tilde{\psi} + \left[\tilde{\varphi}, \psi_{eq}\right] = 0, \tag{5.4}$$

$$\gamma \nabla \cdot (\rho_{eq} \nabla \tilde{\varphi}) = [\tilde{\psi}, J_{eq}] + [\psi_{eq}, \tilde{J}] - e_z \cdot \nabla \times \nabla \cdot \tilde{\overline{\mathbf{P}}}_h \tag{5.5}$$

The quadratic forms can be built multiplying the perturbed plasma equation of motion of Eq. (5.5) by $\tilde{\varphi}^\dagger / 2\gamma^*$ and integrate it over the whole volume extending to infinity. The expression for the dispersion relation is:

$$-\gamma^2 \delta I = \delta W_{MHD} + \delta W_{fast}, \tag{5.6}$$

where δI and δW_{MHD} are respectively defined in Eqs. (4.26) and (4.27). The quadratic form associated with the fast ions is

$$\delta W_{fast} = \int_{\mathscr{V}} d^3x \xi^* \cdot \nabla \cdot \tilde{\bar{\mathbf{P}}}_h / 2 \tag{5.7}$$

. The integral extends over the plasma volume $\mathscr{V}$ and the displacement vector is $\xi = e_z \times \nabla \tilde{\varphi} / \gamma$.

The perturbative approach allows us to consider the extended energy principle. We introduce the small expansion parameter, $\varepsilon_h = n_h / n_c \ll 1$, i.e., the ratio between energetic particle and core plasma densities. Notice that this allows for the fast ion pressure to be of the same order of the core plasma pressure, $\beta_h / \beta_c \sim 1$. In this limit, $|\delta W_{MHD}| \gg |\delta W_{fast}|$. The cubic dispersion relation, Eq. (4.54), is recovered to zeroth order in ε_h. Following the procedure described in Ch.3, we are interested only in the imaginary part of δW_{fast}. The real part of δW_{fast} gives rise to $\mathscr{O}(\varepsilon_h)$ corrections to the VDOM oscillation frequency that can be neglected. The imaginary part of δW_{fast} contributes to the mode growth rate, competing with the damping term γ_η. The imaginary part of δW_{fast} for resonances with $n = 0$ VDOM is derived in Eq. (3.47), and reported here for convenience:

$$\delta W_2 = -\frac{2\pi^2 c}{Zem^2} \sum_\sigma \int dP_\varphi dE d\mu \, \tau_t \omega \frac{\partial F}{\partial E} \sum_{-\infty}^{+\infty} {}^p \frac{\left|\Upsilon_p\right|^2}{\omega + p\omega_{b,t}} \tag{5.8}$$

The following dispersion relation for the oscillatory modes modified by fast ions can be considered:

$$\omega^2 = \omega_0^2 - 2i\omega_0\gamma_\eta + i\omega_0^2\lambda_h + \mathscr{O}(\gamma^2/\omega_0^2), \tag{5.9}$$

where $\lambda_h = \mathscr{I}m(\delta \hat{W}_{h,nad})$ is the properly normalized imaginary part of the fast ion quadratic form. Leading order solutions for the real and imaginary parts of the mode frequency are $\omega = \pm\omega_0 + i\gamma_{tot}$, where $\gamma_{tot} = \omega_0\lambda_h/2 - \gamma_\eta$, highlighting the competition between fast ion drive and resistive wall damping. The wave-particle resonant interaction effect on the stability of the $n = 0$ VDOM is described through the parameter λ_h. A positive λ_h describes a resonant interaction in which the energy exchange is from the particles to the wave. A stabilty threshold can thus be derived, describing the parameters required for the mode to be destabilized by the fast ion contribution. Clearly, a detailed analysis of λ_h, and thus of δW_2 is necessary.

The resonant condition highlighted in the denominator of Eq. (5.8) is $\omega + p\omega_{b,t} = 0$. Note that the $p = 0$ harmonic is non resonant. Bounce and passing frequencies are derived in Sec.2.1.3 and are both proportional to the particle velocity v. We can write $\omega_\Omega = v h_\Omega(r,\Lambda)/(R_0 q)$, where the safety factor $q = rB_\phi/(R_0 B_p)$ is approximately constant and the dimensionless function h_Ω is a combinations of elliptic integrals, different for bounce and trapped orbits ($\Omega = b,t$). The imaginary part of δW_{fast} arise from the integration in velocity around this pole, following the so-called *Landau contour*. The Cauchy principal part of the integral, yielding a real contribution can be neglected. We consider the "thin-orbit" approximation, where the radial excursion of both passing and trapped orbits from a reference magnetic surface is negligibly small allowing us to approximate:

$$P_\varphi \simeq \frac{Ze}{c}\frac{B_0}{2q}r^2 \tag{5.10}$$

$$\rightarrow dP_\varphi = \frac{Ze}{c}\frac{B_0}{q}rdr \tag{5.11}$$

The resulting expression for λ_h is:

$$\lambda_h = \zeta_2 \sum_{p=1}^{+\infty} \int rdrd\Lambda \frac{(v_p^*)^3}{h_\Omega}\frac{\partial F}{\partial E}\bigg|_{v=v_p^*} \left|\Upsilon_p\right|^2 \bigg|_{v=v_p^*} \tag{5.12}$$

where $\zeta = (8R_0\pi^4)/(\mathscr{V}\rho_c\xi^2\omega_0^2)$, ρ_c is the core mass density and $v_p^* = \omega_0 R_0 q/\left[p h_\Omega(r,\Lambda)\right]$ is the resonant velocity. The pitch angle variable $\Lambda = B_0\mu_\perp/E$ ranges from $0 \leq \Lambda \leq 1-\varepsilon$ for passing orbits, to $1-\varepsilon \leq \Lambda \leq 1+\varepsilon$ for trapped orbits. From this expression becomes evident that the sign of λ_h depends only on the derivative of the fast particles equilibrium distribution function with respect to energy. A resonant interaction providing a free energy to the modes requires $\partial F/\partial E > 0$, giving rise to a positive λ_h.

5.1.1 Fourier coefficients

Here we now focus our attention on the Fourier coefficients Υ_p, describing the contribution of the different harmonics of the orbit periodicity to the resonance. Under specific conditions, as outlined, for instance, in [68], the full summation over p can be evaluated, enabling a comprehensive analysis of the complete non-adiabatic response of the particles. In this discussion, we focus on examining the contribution

from dominant harmonics related to the most important Fourier coefficients Υ_p to describe the particles' non-adiabatic response. The Fourier coefficients have been defined in Eq. (2.57) as:

$$\Upsilon_p(E,\mu,P_\varphi;\sigma) = \oint \frac{d\tau}{\tau_{b/t}} \tilde{\mathscr{L}}^{(1)} exp(ip\omega_{b,t}\tau) \tag{5.13}$$

where the loop integral is over a closed banana/transit orbit. Following the procedure of Ref.[36], the perturbed Lagrangian can be rewritten for MHD perturbations as $\tilde{\mathscr{L}} \approx E(2-\Lambda)\xi\cdot\kappa$, with r the radial variable and κ the curvature vector.

To leading order in the parameter ε_h, the displacement vector ξ corresponds to the rigid-shift vertical displacement, which is orthogonal to the main direction of toroidal curvature. The perturbed Lagrangian is proportional to the scalar product $\xi\cdot\kappa$, thus toroidal curvature contributions to λ_h are negligibly small. The perturbed Lagrangian can be expressed as $\tilde{\mathscr{L}} \approx \varepsilon^2 E(2-\Lambda)\xi\sin(\theta)/r$ with $\varepsilon = r/R_0$, where R_0 is the tokamak major radius, and θ is the standard poloidal angle.

We will demonstrate that passing particles primary contribution comes from the $p=1$ harmonic, while for trapped particles both the $p=1$ and $p=2$ harmonics contribute significantly to the resonance. Other harmonics can instead be considered negligible. This outcome is derived in the thin-orbit limit, where r remains approximately constant along the particle orbit. The perturbed Lagrangian then becomes time-dependent only through the poloidal angle θ. Consequently, we can express Υ_p as

$$\Upsilon_p = \varepsilon^2 E(2-\Lambda)(\xi/r)X_p, \tag{5.14}$$

where $X_p = \langle \sin(\theta)\exp(ip\omega_\Omega\tau)\rangle$, with $\langle\rangle$ denoting orbit averaging.

Consider the transit frequency of passing particles,

$$\omega_t = \left[\pi v\kappa\sqrt{\varepsilon/2}\right] / \left[R_0 q \mathscr{K}(1/\kappa^2)\right],$$

where $\mathscr{K}(x)$ is the complete elliptic integral of the first kind, and $\kappa^2 = 1/2 + (1-\Lambda)/(2\varepsilon)$ (for passing orbits, $\kappa \geq 1$). We observe that

$$\omega_t\tau = \left[\pi\mathscr{F}(\theta/2|1/\kappa^2)\right] / \left[\mathscr{K}(1/\kappa^2)\right] \approx \theta,$$

with $\mathscr{F}(\phi|x^2)$ denoting the incomplete elliptic integral of the first kind. The last equality holds for the majority of κ values, except for cases where κ is very close to unity, corresponding to the barely passing limit. This limit, and particularly the particle response near the passing-trapped boundary, demands careful consideration, as outlined in [68]. Nevertheless, given that this limit corresponds to $\omega_t \to 0$, these particles are non-resonant when focusing on the dominant Υ_p coefficients. Consequently, their contribution to λ_h can be safely neglected. In this way, X_p reduces to: $i(1/4\mathscr{K}(1/\kappa^2))\int_0^{2\pi} d\theta\,[\sin(\theta)\sin(p\theta)]/\sqrt{1-\sin^2(\theta/2)/\kappa^2}$, and, in the asymptotic limit $\kappa \gg 1$, $X_p \approx i(1/2\pi)\int_0^{2\pi} d\theta \sin(\theta)\sin(p\theta)$. It is evident that the only harmonic contributing in this limit is $p = 1$, while the average is zero for all other p values. Figure 5.1 depicts $|X_p|^2$ for the first two harmonics as functions of κ, showing that even considering other κ values, the contribution of passing particles for harmonics with $p > 1$ is indeed negligible.

For trapped particles, $0 \leq \kappa \leq 1$, the bounce frequency is

$$\omega_b = \pi v\sqrt{\varepsilon/2}/\left[2R_0 q\mathscr{K}(\kappa^2)\right].$$

Then,

$$\omega_b\tau = (\pi/2)\mathscr{F}(\zeta|\kappa^2)/\mathscr{K}(\kappa^2),$$

where $\sin(\theta/2) = \kappa\sin(\zeta)$. As for the case of passing particles, we consider κ values far from the passing-trapped limit $\kappa = 1$, where the bounce frequency drops to 0. It is then possible to approximate $\omega_b\tau \approx \zeta$. Therefore, one obtains $X_p = \kappa/\mathscr{K}(\kappa^2)\int_{-\pi/2}^{\pi/2} d\zeta \sin(\zeta)\sin(p\zeta)$. This quantity is zero for both barely trapped ($\kappa = 1$) and deeply trapped ($\kappa = 0$) limits, as shown also in Fig. 5.1. All even-p harmonics yield a non-zero X_p; however, values of X_p with $p \geq 4$ are negligibly small. For odd-p values, X_p averages exactly to 0, with the only exception of $p = 1$. Therefore, we focus only on the $p = 1$ and $p = 2$ harmonics. In Fig. 5.1, values of $|X_p|^2$ for the $p = 1$ and $p = 2$ harmonics are plotted as functions of κ.

The reason why deeply trapped particles ($\kappa = 0$) and barely trapped/passing particles ($\kappa = 1$) do not contribute to Υ_p and, consequently, to λ_h is straightforward. For $n = 0$ vertical displacements, $\xi \cdot \kappa \sim \sin\theta$. Deeply trapped particles are concentrated near $\theta = 0$, while barely trapped particles spend most of their time near $\theta = \pi$. Therefore, the orbit-averaged value of the scalar product $\xi \cdot \kappa$ becomes zero in both these limits. Both trapped and passing particles have their orbit frequencies described

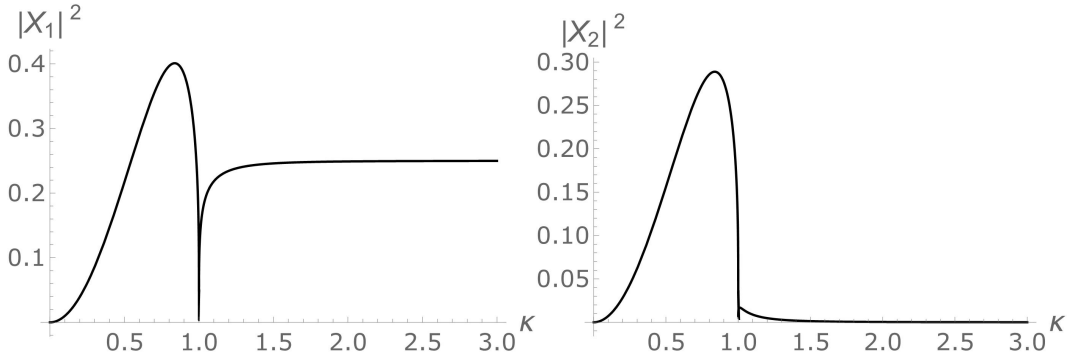

(a) First harmonic p=1 (b) Second harmonic p=2

Fig. 5.1 Plots of $|X_p|^2 = |\langle \sin(\theta) \exp(ip\omega_\Omega \tau)\rangle|^2$ as a function of κ for $p = 1$ and $p = 2$ harmonics.

analytically in the small aspect ratio limit, considering circular magnetic flux surfaces as discussed in Chapter 2. The bounce and transit orbits can be described taking into account higher order corrections in ε, as detailed in Ref.[22], and/or plasma shaping, such as elongation and triangularity, as reported in Ref.[69]. While these corrections could provide a more comprehensive description of the Fourier coefficients Υ_p, they are omitted in the present analysis for consistency with other approximations made and the proof-of-principle nature of the study.

5.2 Fast ion distribution function

The choice of the equilibrium distribution function allows us to determine the effect of superthermal particles on the $n = 0$ VDOM stability. The particular condition of $\partial F/\partial E|_\mu > 0$ is required for the mode destabilization. As discussed in Sec. 3.3, this situation can be achieved under different conditions, that will be studied separately in the following.

5.2.1 Slowing-down with losses

We consider the first simplified model with a monochromatic source term at velocity v_b, and a velocity-independent loss frequency, ν_l obtained in Eq. (3.61). Assuming a

uniform radial distribution of fast ions up to $r = r_h$, the distribution function is:

$$F(r,v) = \tau_{s0} S_0 v_b^{2-3l_0} \frac{H(v_b - v)}{v^{3-3l_0}} H(r_h - r) \tag{5.15}$$

The normalization constant $\tau_{s0}S_0$ can be generally rewritten for any kind of fast ions in terms of the fast particle density n_h with $\int d^3v F = n_h$. The derivative over the energy is trivially rewritten as $\partial F/\partial E = 1/(m_h v)\partial F/\partial v$, with energetic ions mass m_h. After straightforward algebra, substituting the distribution function derivative and Eq. (5.14) in Eq. (5.12), we obtain

$$\lambda_h = \frac{9\pi l_0(l_0-1)q^2}{a^2 R_0^2} \frac{n_h m_h}{n_c m_c} \sum_{p=1,2} \left(\frac{v_{p0}^*}{v_b}\right)^{3l_0} \frac{1}{p^2} \times$$
$$\int dr d\Lambda \frac{r^3(2-\Lambda)^2 |X_p|^2}{h_\Omega(r,\Lambda)^{3l_0+3}} H(r_h - r) H(v_b - v_p^*) \tag{5.16}$$

where n_c is the core plasma density, m_c is the core ion mass, and $v_{p0}^* = \omega_0 R_0 q/p$ is the resonant velocity of passing particles with $\Lambda = 0$. We can write $\lambda_h = (n_h/n_c)(m_h/m_c)(q^2a^2/R_0^2)\lambda$, where $\lambda(l_0, r_h/a, v_{p0}^*/v_b)$ is a dimensionless factor that depends on three parameters. Inserting this expression for λ_h in Eq. (5.9), the instability threshold can be cast in the form

$$\frac{n_h}{n_c} \geq \left(\frac{n_h}{n_c}\right)_{crit} = \frac{m_c}{m_h} \frac{R_0^2}{q^2 a^2} \frac{2\gamma_\eta}{\lambda \omega_0}. \tag{5.17}$$

To gain further insight into realistic numerical values for the critical density threshold, we consider the parameters of the JET experiments discussed in Ref.[3], where saturated $n = 0$ oscillations were observed, and MeV fast ions were produced by a combination of ICRH and NBI. Some parameters are experimentally well-known, e.g., $R_0 = 3$m, $a = 0.9$m, elongation $b/a \approx 1.3$, which corresponds to $e_0 \approx 0.3$, toroidal magnetic field $B_T = 2.2T$, $q \approx 1$, and Deuterium main ion species, yielding an inverse poloidal Alfvén time $\tau_A^{-1} \approx 2 \times 10^{-6}\text{s}^{-1}$. The experimentally observed $n = 0$ oscillation frequency is in the range $f_0 = \omega_0/2\pi \approx 300kHz$, which compares well with the theoretically predicted value of the frequency ω_0, defined below Eq.(4.54), if we assume realistic values for the geometrical factor, $D \approx 3$. Fast ions in the mentioned JET experiments are also mostly Deuterium, thus we take $m_h/m_c = 1$. We assume $r_h/a = 0.5$ and $l_0 \approx 2$. The remaining parameter to be

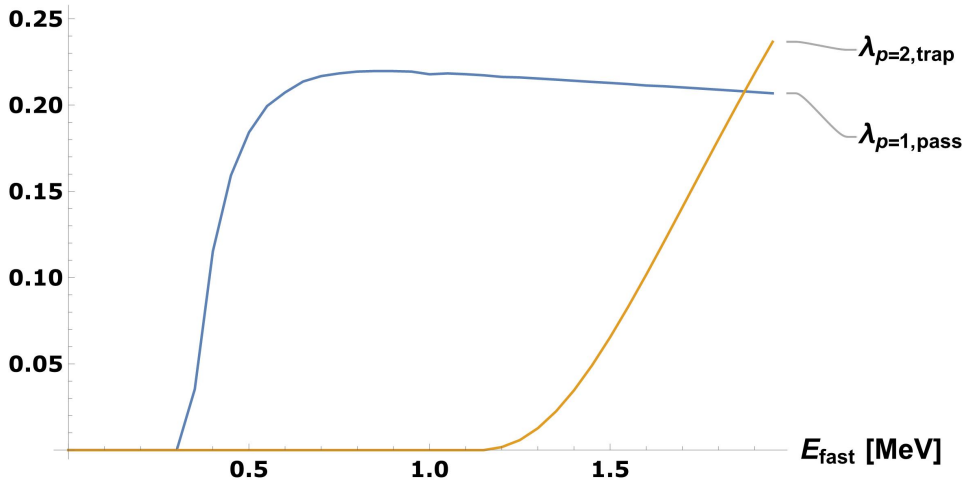

Fig. 5.2 Coefficients $\lambda_{p=1,pass}$ and $\lambda_{p=2,trap}$ as function of fast ion birth energy E_b.

evaluated, $v^*_{p0}/v_b = \omega_0 R_0 q/(p v_b)$, depends on the fast ion birth energy, $E_b = m_h v_b^2/2$. Realistic JET estimates indicate values of E_b in the MeV range. Having fixed all the parameters just mentioned, we plot in Fig. (5.2) the contributions to λ_h coming from the different harmonics, as functions of E_b. We can see that the $p = 1$ harmonic associated with passing particles is the leading contribution for fast ion energies up to ~ 1.5 MeV. At higher energies, the $p = 2$ harmonic of trapped particles can also give a significant contribution. On the other hand, for the considered parameters, the trapped particles $p = 1$ harmonic gives a non-zero contribution only for a birth energy $E_b \geq 5MeV$. Let us write $\lambda = \lambda_{p=1,pass} + \lambda_{p=2,trap}$. The overall value of the parameter λ is estimated to be of the order of 3×10^{-1} for the JET experiments of interest, for $E_b = 1.5MeV$.

The damping rate resulting from the resistive wall is estimated to be on the order of $\gamma_\eta \sim 3 \times 10^2\ s^{-1}$. Consequently, the critical instability threshold for the JET experiments can be approximated as $(n_h/n_c)_{crit} \sim 1 \times 10^{-2}$.

5.2.2 Anisotropic slowing-down

The single pitch angle slowing down distribution function of Eq. (5.18) is now considered in order to study the drive due to velocity space anisotropy. The anisotropy in velocity space introduces a competition between the derivative of the slowing down part of the distribution function, which is always negative, and the one from the anisotropy. To highlight this competition, we neglect the losses, taking $l_0 = 0$.

As for the previous isotropic case, a uniform radial distribution of fast ions up to $r = r_h$ is assumed:

$$F(r,v,\Lambda) = \tau_{sd}\hat{S}_0(\Lambda_0)v_b^2\frac{H(v_b-v)\delta(\Lambda-\Lambda_0)}{v^3}H(r_h-r) \tag{5.18}$$

The normalization coefficient $\hat{S}_0$ in this case is dependent on the single pinch Λ_0 and can be derived considering the orbit averaged fast ion density defined as:

$$n_h = \oint \frac{d\theta}{2\pi}\int d^3v F(r,v,\Lambda) \tag{5.19}$$

where the velocity volume element can be written in the formalism of Ch. 2 as:

$$d^3v = v_\perp dv_\perp d\alpha dv_\parallel = \pi\sum_\sigma \frac{v^2}{(1-\Lambda/h)^{1/2}}dvd\Lambda/h \tag{5.20}$$

The integration can be performed following similar steps as the one described in Sec. 2.1 for passing and trapped ions, i.e. for $\Lambda_0 \leq 1-\varepsilon$ and $1-\varepsilon \leq \Lambda_0 \leq 1+\varepsilon$. The resulting normalization coefficients then are:

$$\hat{S}_{0,\Omega}(r,\Lambda_0) = n_h\sqrt{\varepsilon}\frac{1}{2\sqrt{2}log(v_b/v_c)}s_\Omega(r) \tag{5.21}$$

$$s_t(r) = \kappa_0/\mathscr{K}(1/\kappa_0^2) \quad s_b(r) = 1/\mathscr{K}(\kappa_0^2) \tag{5.22}$$

where $\mathscr{K}(x)$ is the complete elliptic integral of the first kind, the parameter $\kappa_0 = 1/2+(\Lambda_0-1)/(2\varepsilon)$ and v_c is the critical velocity at which the fast-ions thermalize with the core plasma. The full derivative of the distribution function over energy reads:

$$\left.\frac{\partial F}{\partial E}\right|_\mu = -\frac{3}{m_h}\frac{F(r,v,\Lambda)}{v^2} - \tau_{sd}\hat{S}_{0,\Omega}(r,\Lambda_0)v_b^2\frac{2\Lambda}{m_h}\frac{H(v_b-v)}{v^5}\frac{\partial}{\partial\Lambda}\delta(\Lambda-\Lambda_0) \tag{5.23}$$

The first term is always negative coming from the *slowing-down* part of the distribution function. Its contribution to λ_h can be obtained from Eq. (5.12) integrating over

Λ using the delta function properties:

$$\lambda_{h,sl} = -\frac{3\pi^2 q^2}{2\sqrt{2}a^2 R_0^2 log(v_b/v_c)} \frac{m_h n_h}{m_c n_c} \sum_p \frac{1}{p^2} \times \int dr \frac{r^3 \sqrt{\varepsilon}(2-\Lambda_0)^2 |X_p|^2}{h_\Omega(r,\Lambda_0)^3} s_\Omega(r) H(r_h - r) H(v_b - v_p^*) \tag{5.24}$$

Being always negative, it has always a stabilizing effect on the mode. The second term of Eq. (5.23) is associated with the velocity space anisotropy. Its contribution to λ_h can be expressed starting again from the integral expression of Eq. (5.12). The delta function property

$$\int dx f(x) \frac{\partial}{\partial x} \delta(x - x_0) = -\int dx \delta(x - x_0) \frac{\partial}{\partial x} f(x) \tag{5.25}$$

can be used to integrate in Λ.

$$\lambda_{h,ani} = \frac{\pi^2 q^2}{\sqrt{2}a^2 R_0^2 log(v_b/v_c)} \frac{m_h n_h}{m_c n_c} \sum_p \frac{1}{p^2} \times \int dr r^3 \sqrt{\varepsilon} G_\Omega(r,\Lambda_0) s_\Omega(r) H(r_h - r) H(v_b - v_p^*) \tag{5.26}$$

where the functions $G_\Omega = \partial \left[\Lambda(2-\Lambda)^2 |X_p|^2 / h_\Omega(r,\Lambda_0)^3)\right] / \partial\Lambda$ are different for transit and bounce orbits, and can be written as:

$$G_t = \frac{2\sqrt{2}}{\pi^3} \frac{(2-\Lambda)}{\varepsilon^{3/2}} \frac{\mathscr{K}(1/\kappa^2)^3}{\kappa^3} \left\{ (2-3\Lambda)|X_p|^2 + \frac{\Lambda(2-\Lambda)}{2\varepsilon\kappa} \times \left[-|X_p| \frac{\partial |X_p|}{\partial \kappa} + \frac{3}{2} \frac{\kappa \mathscr{E}(1/\kappa^2)}{(\kappa^2) - 1 \mathscr{K}(1/\kappa^2)} |X_p|^2 \right] \right\} \tag{5.27}$$

$$G_b = \frac{16\sqrt{2}}{\pi^3} \frac{(2-\Lambda)}{\varepsilon^{3/2}} \mathscr{K}(\kappa^2)^3 \left\{ (2-3\Lambda)|X_p|^2 + \frac{\Lambda(2-\Lambda)}{2\varepsilon\kappa} \times \left[-|X_p| \frac{\partial |X_p|}{\partial \kappa} + \frac{3}{2} \frac{(\kappa^2-1)\mathscr{K}(\kappa^2) - \mathscr{E}(\kappa^2)}{\kappa(\kappa^2)\mathscr{K}(\kappa^2)} |X_p|^2 \right] \right\} \tag{5.28}$$

where $\mathscr{E}(x)$ is the complete elliptic integral of the second kind. This second contribution to λ_h can be either positive or negative depending on the value of Λ_0 and on the parameters considered. Therefore the total interaction $\lambda_h = \lambda_{h,sl} + \lambda_{h,ani}$ is the result of the competition between the two terms. Similarly to the previous

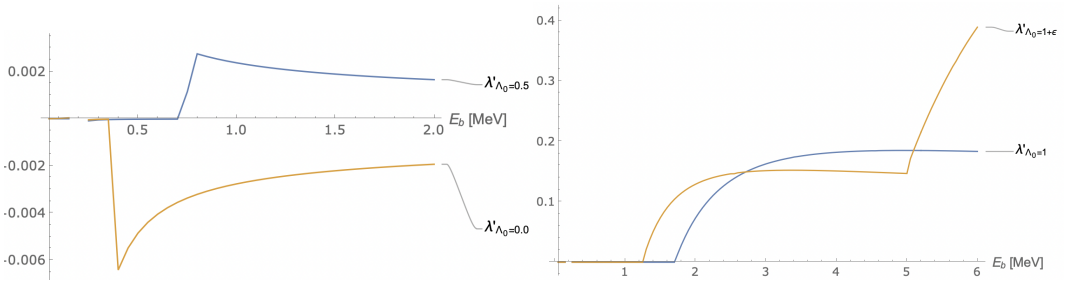

(a) (b)

Fig. 5.3 Dimensionless factor λ' as a function of E_b. For passing particles $\Lambda_0 = 0$ and $\Lambda_0 = 0.5$ are plotted (a) up to $E_b = 2MeV$. Trapped particles are plotted for values of $\Lambda_0 = 1$ and $\Lambda_0 = 1+\varepsilon$ up to $E_b = 6MeV$.

subsection, we can write $\lambda_h = (n_h/n_c)(m_h/m_c)(q^2a^2/R_0^2)\lambda'$, with dimensionless factor $\lambda'(\Lambda_0, r_h/a, v^*_{p0}/v_b)$ that depends on the model parameters. With the same parameters related to the JET case discussed in subsection 5.2.1, we can study how the total $\lambda' = \lambda'_{ani} + \lambda'_{sl}$ behaves as a function of E_b and Λ_0. Firstly, in Fig. 5.3 we show the total λ' for different values of Λ_0, as a function of the birth energy. One can see how for $\Lambda_0 = 0$ λ' is always negative, corresponding to a stabilizing resonant interaction for any birth energy. For trapped particles we can note how for a birth energy $E_b \lesssim 1.2MeV$ there is no resonance for $p = 1,2$. Then the second harmonic starts to resonate up to $E_b \sim 5MeV$. For larger birth energies also the first harmonic stars to give a non-zero contribution.

A threshold in Λ_0 can be obtained in order to have $\lambda' > 0$. Figure 5.4, shows how λ' varies as a function of Λ_0 for $E_b = 1Mev$ and $E_b = 2Mev$: the condition $\lambda_h > 0$ requires $\Lambda_0 > 0.4$, the same threshold found for EGAMS considering the same distribution function in [70].

5.3 Concluding remarks

This chapter extends the analytic model introduced in Chapter 4, which describes Vertical Displacement Oscillatory Modes (VDOM), to incorporate kinetic effects from superthermal ions. The focus is on investigating how the presence of energetic ions could potentially destabilize VDOM in tokamak plasmas, considering different equilibrium distribution functions. The results presented in this section show how a new kind of fast-ion-driven mode can arise in tokamak plasmas due to the resonant

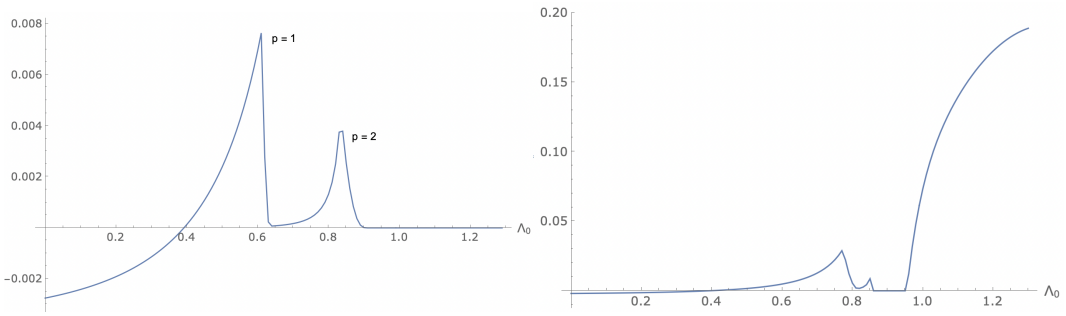

(a) (b)

Fig. 5.4 Dimensionless factor λ' as a function of the single pitch Λ_0. In (a) the birth energy considered is $E_b = 1MeV$, while in (b) $E_b = 2MeV$.

interaction of VDOM with MeV energetic ions. Despite the simplicity of the model, the results presented in this chapter suggest that VDOM destabilized by fast ions could be a plausible explanation for the observed $n = 0$ modes destabilized by MeV ions in recent JET discharges.

Chapter 6

NIMROD Linear Simulations

The analytic results presented in the previous chapters represent the building blocks of our theory describing the VDOM and their possible destabilization in presence of superthermal ions. In order to gain the fundamental understanding of the physical mechanisms associated with these axisymmetric modes of the plasma, simplifying assumptions have been considered. In this chapter we will show, thanks to numerical simulations using the MHD NIMROD code [71], that the main characteristics obtained with our very simplified model persist considering realistic experimental situations. The NIMROD code is employed to study the extended MHD stability of the plasma. However, in this chapter the superthermal ions effects are not present, since work is in progress to extend the capabilities of the NIMROD code to simulate the cases described in Ch. 5. Nevertheless, here we aim to describe mode frequency and mode structure in real tokamak geometry and with experimental plasma profiles. We will thus focus on the characteristic of the normal modes that may be driven unstable if a suitable distribution function of fast ion is included in the plasma.

The results reported in this chapter have been published in [18] and [2].

6.1 Extended MHD nimrod code

The simulations described in this chapter advance the linearized single-fluid resistive MHD equations (6.1)-(6.4) in toroidal geometry using the 3D initial value code NIMROD [71]:

$$\frac{\partial n}{\partial t} + \nabla \cdot (n\mathbf{v}) = \nabla \cdot \mathscr{D} \nabla n \tag{6.1}$$

$$mn\left(\frac{\partial}{\partial t} + \mathbf{v} \cdot \nabla\right)\mathbf{v} = \frac{1}{\mu_0}(\nabla \times \mathbf{B}) \times \mathbf{B} - \\ - \nabla p + \nabla \cdot \nu\rho\nabla\mathbf{v} \tag{6.2}$$

$$\frac{3}{2}\left(\frac{\partial}{\partial t} + \mathbf{v} \cdot \nabla\right) T = -nT\nabla \cdot \mathbf{v} \tag{6.3}$$

$$\frac{\partial \mathbf{B}}{\partial t} = -\nabla \times [\eta_e (\nabla \times \mathbf{B}) - \mathbf{v} \times \mathbf{B}] + \\ + \kappa_{divb} \nabla\nabla \cdot \mathbf{B}. \tag{6.4}$$

In these equations, n and m are respectively particle density and ion mass. The total pressure of electrons and ions is p, $\mathbf{v}$ is the center-of-mass plasma velocity, T is the plasma temperature and $\mathbf{B}$ is the magnetic field. Explicit diffusive terms are included in the model: the density diffusivity $\mathscr{D}$, kinetic viscosity ν, electrical diffusivity coefficient η_e (=resistivity over the vacuum permeability μ_0), and κ_{divb} is a diffusivity coefficient used to control the $\nabla \cdot \mathbf{B}$ error in the induction equation. The code employs high-order quadrilateral finite elements for modelling the poloidal plane and pseudo-spectral techniques for the periodic axisymmetric direction. NIMROD can efficiently advance both linear and nonlinear extended-MHD equations, with implicit or semi-implicit time-advance methods to address the temporal stiffness associated with multiple time scales. In this chapter, we restrict ourselves to the case of linear stability studied throughout the whole thesis.

Here we outline key characteristics of the simulations discussed in the following sections, emphasizing significant distinctions from the analytic model presented in Ch. 4. Unlike the analytic model, NIMROD does not support a vacuum model; instead, it employs a "halo" plasma model to simulate the analytic vacuum. The "halo" plasma is a cold region with low density and high resistivity (η_{halo}), exhibiting a few orders of magnitude difference from the hot core plasma. The simulation boundary in NIMROD serves as the representation of the wall and is assumed to be

an ideal conducting wall. In NIMROD, the ideal conducting wall is implemented with vanishing normal components of the perturbed magnetic field at the simulation boundary.

The first results of our numerical analysis are described in Sec. 6.2. Here we verify the analytic theory reproducing the straight tokamak equilibrium of Ch. 4 in NIMROD. The dispersion relation as a function of plasma-wall distance and elongation of Eq. 4.54 is recovered numerically. Thanks to this result, in Sec.6.3 a recent JET discharge is analyzed with the NIMROD code in order to study the VDOM in realistic tokamak conditions. For this investigation, JET shot #102371 was selected. This discharge is part of a series of JET deuterium plasmas produced during the experimental campaign RT 22-09 on March 2023. The aim of these discharges was the investigation of $n = 0$ modes with Alfvén frequencies that have been succesfully observed.

6.2 Verification of the analytic results with straight tokamak simulations

In this section, we present the benchmark comparison between the analytic theory results of Ch. 4 and NIMROD numerical simulations.

In most simulations presented, the grid resolution is (mx,my)=(360,360) with polynomial degree = 3 and the timestep $\Delta t = 0.5\tau_A$. The different diffusion parameters used in the model have been minimized in the "hot" plasma region, to reduce dissipation and mimic an ideal MHD plasma, to allow a comparison with the analytic treatment of VDOM based on the ideal MHD model. For simplicity of NIMROD implementation, the analytic straight tokamak is represented by a Cartesian rectangular domain in the poloidal plane and a single toroidal $n = 0$ mode in the axisymmetric z-direction. This differs from the confocal elliptical wall in the analytic model. Instead, the four sides of the rectangular simulation domain are constrained by imposing the confocal condition, $b_w^2 - a_w^2 = b^2 - a^2$, so that the half-height, b_w, and the half width, a_w, of the rectangular boundary match the major and minor axes of a confocal elliptical boundary. The rectangular simulation domain circumscribes the analytic confocal ellipse and as such, for equal values of the parameter b/b_w, the simulation domain is larger than the analytic one.

Figure 6.1 well summarizes the results of this numerical analysis. The simulation growth rates/frequencies are plotted (Dots) together with the analytic dispersion relation (green line) of Eq. 4.54 for an ideal wall. Both the stable oscillatory case and the ideal vertical instability can be resolved in our simulations. The zero crossing in the analytic theory curve signifies the transition between a mode that is purely oscillatory and one that is purely growing. This transition occurs when b_w equals b_X, where b_X represents the vertical distance of the X-points from the magnetic axis. In essence, the onset of marginal stability, characterized by $\omega^2 = 0$, happens when the confocal elliptical wall intersects the X-points. For small values of b/b_w, the growth rate ($\gamma = -i\omega$) diminishes as the wall approaches the plasma (with increasing b/b_w). As the wall gets closer to the X-point, the mode reaches marginal stability. Beyond this point, for $b/b_w > b/b_X$, the mode becomes purely oscillatory as the wall moves inside the X-points, i.e., when the X-points lie outside the simulation domain.

In the simulations, the transition from the unstable growing mode to the stable oscillatory mode does not precisely coincide with the interception of the rectangular wall with the X-points, as expected from the analytic results. It is noteworthy that the numerical points are slightly below the analytic curve, particularly at larger values of b/b_w where the wall is in closer proximity to the plasma boundary. This deviation is attributed to the rectangular simulation domain, which, at equal values of the parameter b/b_w, has a larger area compared to the equivalent confocal elliptical boundary in the analytic model. Consequently, the rectangular wall is, on average, a bit farther away, leading to a slightly weaker stabilizing effect. As a result, the growth rate found numerically is somewhat larger (i.e., smaller negative ω^2) than the analytic prediction.

Focusing our attention to the simulation results for stable VDOM, we emphasize the mode structure obtained with the straight tokamak simplified equilibrium. As the conducting wall is brought closer to the plasma, the mode undergoes a transition from an unstable state to the stable oscillatory mode described analytically in Ch. 4 and in [15]. We examine in detail one such stable oscillatory case. Figure 6.2a plots the time history of perturbed fields: velocity ($\tilde{v}_y$), magnetic field ($\tilde{B}_x$), density ($\tilde{n}$), temperature ($\tilde{T}$), showing the oscillatory behaviour of the perturbations. The normalized oscillation frequency is $\omega\tau_A = 0.31$. In Fig. 6.2b the mode structure is represented, plotting midplane profiles (at $y = 0$) of perturbed vertical momentum per unit mass, $n_0\tilde{v}_y$, at several times during a single period, for $\kappa = 1.4$ and $b/b_w = 0.55$. The single oscillation period is denoted by the yellow bar in the time history of

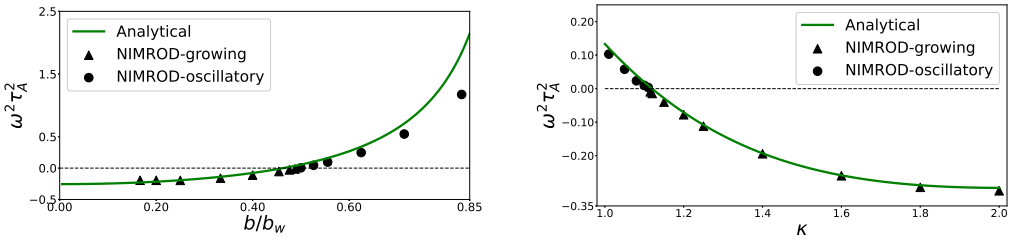

(a) *wall* (b) κ

Fig. 6.1 Confocal wall scan ($b_w^2 - a_w^2 = b^2 - a^2$) plots the square of the normalized frequency vs. wall parameter b/b_w for κ = 1.4 (left panel) and κ scan with wall parameter fixed at $b/b_w = 0.25$ (right panel), showing agreement between NIMROD and analytic theory. Positive values (circles) indicate oscillating modes. Negative values (triangles) indicate growing modes. The zero crossing of the analytic theory curve (green line) occurs for $b/b_w = b/b_X$, where the domain boundary intersects the X-points.

Fig. 6.2a. The perturbed momentum profile on the midplane shows that the $n = 0$ oscillation is mostly confined within the hot plasma, with a perturbed mass flow that well approximates the rigid-shift vertical oscillation found in analytic work. Note that the plasma extends to $x/b = a/b \approx 0.7$.

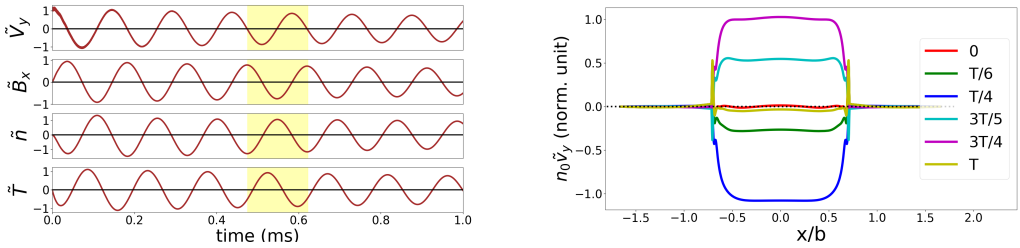

(a) time history of perturbed fields (b) midplane profiles of $n_0 \times \tilde{v}_y$

Fig. 6.2 Time history of perturbed fields: velocity($\tilde{v}_y$), magnetic field($\tilde{B}_x$), density($\tilde{n}$), temperature($\tilde{T}$); midplane profiles of vertical momentum per unit mass at several times during a single oscillation period (denoted by the yellow bar in the time history); κ=1.4 and b/b_w=0.55. The plasma motion is well approximated by a vertical rigid shift.

6.3 JET simulations

6.3.1 Experimental Observations: GAE and VDOM

Excitation of high frequency $n = 0$ modes have been reported in JET [3, 44]. Reference [3] proposed Global Alfvén Eigenmodes (GAE) [13] as explanation for the observed $n = 0$ modes. The modes were driven unstable by resonant interaction with energetic ions with energies in the MeV range, produced by auxiliary heating (combined NBI and ICRH) or by fusion reactions. While GAE remain a distinct possibility for the interpretation of the mentioned JET observations, the fast-ion-driven VDOM described analytically in Chapters 4 and 5 represent a valid alternative. GAE and VDOM are two different types of normal modes of a magnetically confined plasma, the former being internal modes, which can exist for different values of the toroidal mode number n, with frequency close to the minimum of the Alfvén continuum spectrum, while the latter are $n = 0$ external modes interacting with currents induced on the wall of the confining vacuum chamber by the vertical motion of the plasma. Other differences between the two modes involve their different spatial structure and their different sensitivity to details of safety factor q profile, plasma ellipticity, and plasma-wall distance. Given the apparent ease with which these modes can be destabilized by fusion alpha particles, both VDOM and GAE are likely to play an important role in future tokamak experiments where burning fusion plasmas will be produced. The main characteristics for a comparison between GAE and VDOM are summarized in Table 6.1.

6.3.2 NIMROD simulations of VDOM in JET

In this section we aim to a more realistic assessment of the nature of VDOM with the help of NIMROD simulations. The results presented in the following report linear NIMROD simulations using the EFIT [72, 73] reconstructed equilibrium of JET shot #102371 at time $t = 51.00$s. The equilibrium pressure and safety factor provided by EFIT are shown in Figs. 6.3a and 6.3b, respectively. Figure 6.3c shows our best fit of the equilibrium electron density profile. The on-axis value of the electron density is $n_0 = 5.2 \times 10^{19}$ m^{-3}. The experimentally measured value of the effective charge, $Z_{eff} = 1.75$, was also used to evaluate the plasma mass density. The plasma in the open field line region is represented using a "halo" plasma model, with low

Table 6.1 Comparison between VDOM and GAE.

VDOM	GAE
- External mode. - Global, odd parity with respect to poloidal angle. - Nearly rigid shift, up-down vertical motion, radial structure weakly dependent on q profile. - Alfvénic frequency dependent on plasma elongation and plasma-wall distance, weakly dependent on q profile details.	- Internal mode. - Global, even parity with respect to poloidal angle. - Poloidal flow peaking near minimum of $n = 0$ Alfvén continuum, radial structure depends on q profile. - Alfvénic frequency close to the minimum of the $n = 0$ Alfvén continuum.

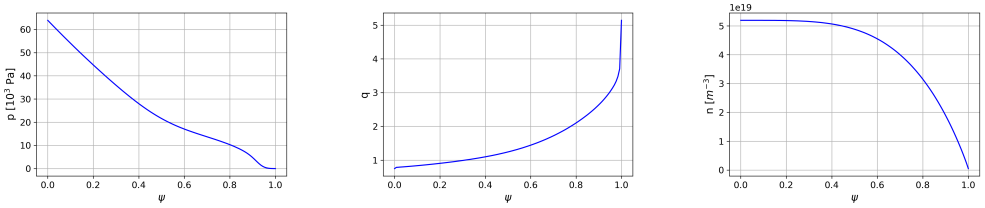

(a) (b) (c)

Fig. 6.3 EFIT equilibrium pressure profile (6.3a), and safety factor (6.3b); best fit of the experimental electron density profile (6.3c), as functions of normalized flux. The separatrix is at $\psi = 1$.

density and high resistivity. In particular, the plasma density profile is uniform in the open field line region with a value of $n_{halo} = 5 \times 10^{17} m^{-3}$. The different diffusion parameters used in the model have been minimized in the "hot" plasma region, to reduce dissipation and mimic an ideal MHD plasma, to allow a comparison with the analytic treatment of VDOM based on the ideal MHD model. In the following simulations, the grid resolution is (mx,my)=(60,90) with polynomial degree = 3 and the timestep $\Delta t = 10^{-7} s$.

The simulations presented in this Section describe the plasma response to an initial perturbation in velocity corresponding to a rigid vertical shift of the plasma, dubbed "vertical push" in the following. The oscillatory behaviour of all relevant perturbed fields follows the initial vertical push. Figure 6.4 shows the behaviour of

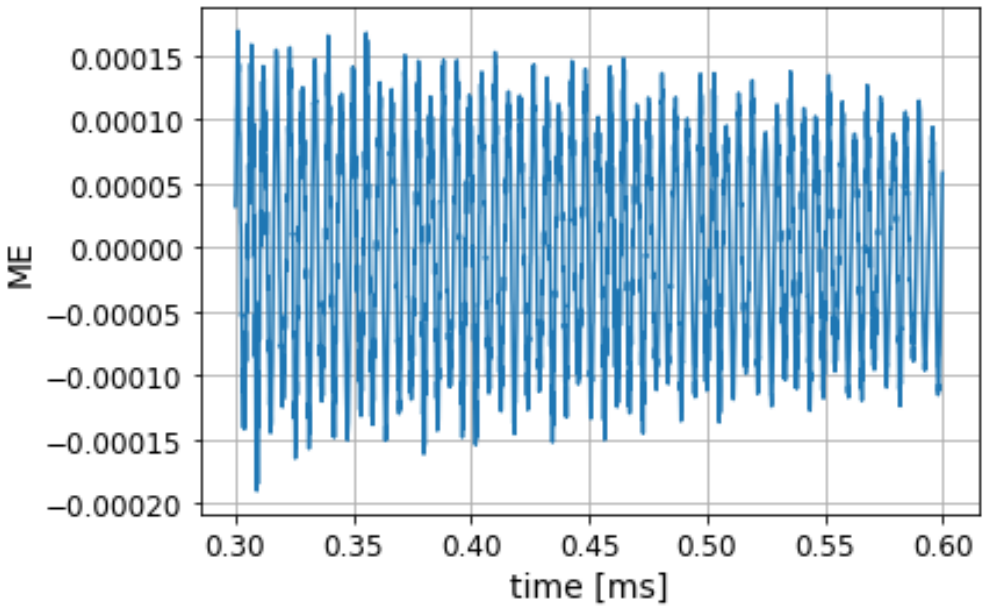

Fig. 6.4 Oscillatory behaviour of the magnetic energy in response to a "vertical push", in the time interval between $t = 0.3$ ms and $t = 0.6$ ms.

the magnetic energy as a function of time. Weak damping of the oscillatory behaviour is observed. The careful choice of initial perturbation is necessary, because VDOM are stable modes, and therefore different initial conditions lead to a mix of different oscillatory modes. The resulting interference would cause a rapid decay of all modes, including the VDOM. This problem is overcome in the next Section, where a different method to drive the perturbation is examined.

Figure 6.5 shows contour plots of tangential and normal components, with respect to the equilibrium flux surfaces, of the perturbed magnetic field. Fig. 6.6 shows the contour plots of perturbed pressure. Both plots are taken at time $t = 0.5ms$ in the simulation, corresponding to a minimum of the magnetic energy oscillation. An $m = 1$ mode structure is evident in the perturbed fields; the pressure perturbation shows the up-down feature characteristic of VDOM.

Fast Fourier Transform (FFT) has been employed to analyze the temporal behaviour of the plasma response. The whole linear simulation time of $1ms$ has been considered to compute the discrete Fourier Transform (DFT) with the efficient FFT algorithm [74]. The FFT signal of the magnetic energy time trace is shown in Fig. 6.7. A dominant peak in the FFT signal can be identified at frequency $f_{low} = 184$ kHz, while a secondary peak indicates the presence of a second subdominant mode at

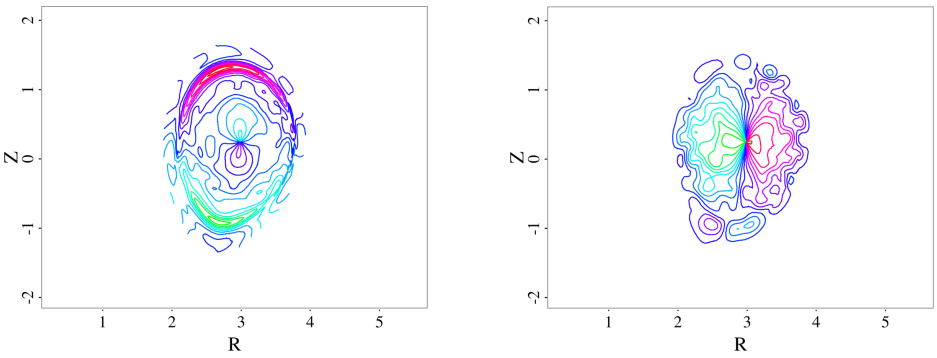

(a) (b)

Fig. 6.5 Magnetic field perturbation in response to a "vertical push". (a) Tangential, and (b) normal B-components with respect to the equilibrium flux surfaces. A main m=1 structure, expected for the VDOM, can be identified.

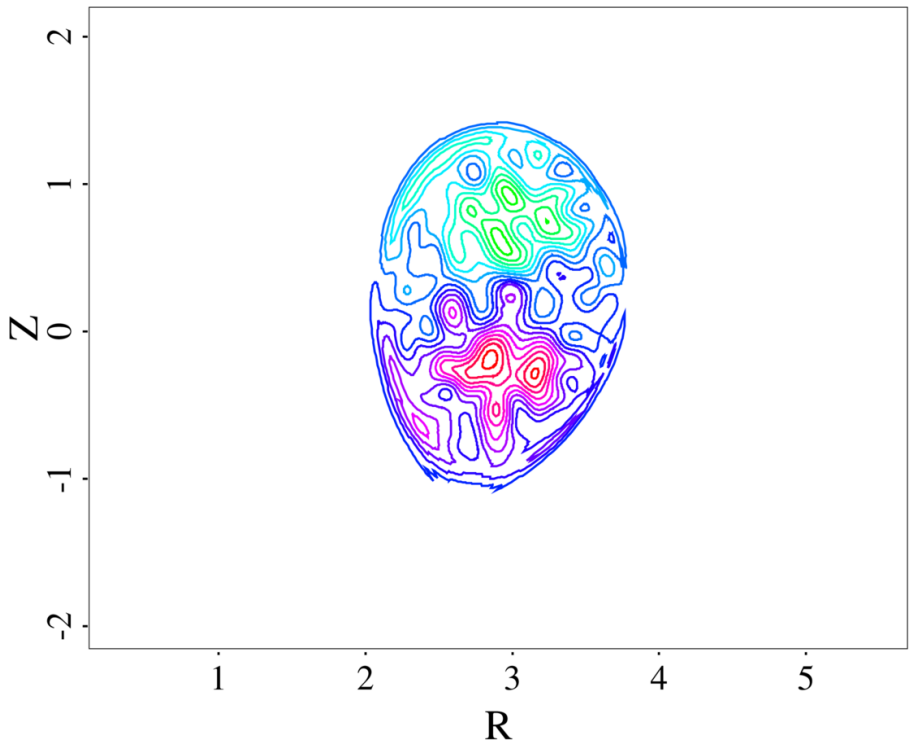

Fig. 6.6 Pressure perturbation, $\tilde{p}$, in response to a "vertical push", showing the up-down structure characteristic of the VDOM.

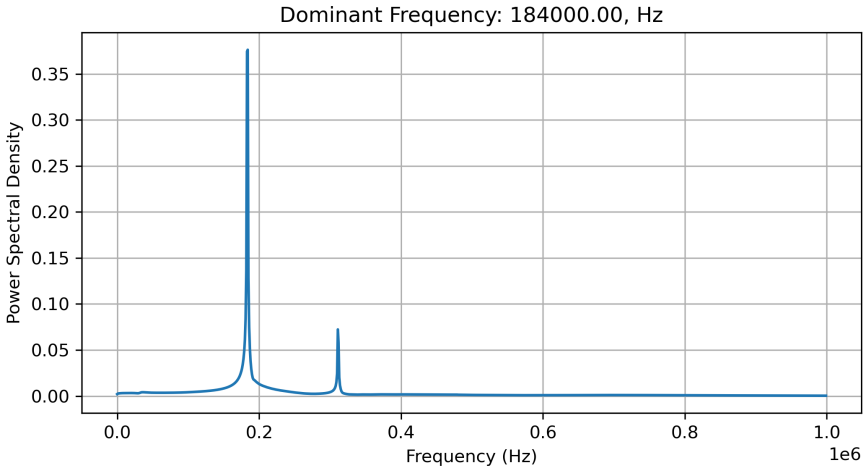

Fig. 6.7 FFT signal (absolute value) of the oscillating magnetic energy in simulation ("vertical push"). Two peaks can be identified: a dominant one at $184kHz$, and a secondary one at $311kHz$.

frequency $f_{high} = 311$ kHz. This indicates the presence of two Alfvén-frequency normal modes with $n = 0$ that are both excited in response to the initial vertical push. The simultaneous presence of the two modes gives rise to interference. The space and time dependence of the plasma response cannot be separated in this case. As the two modes are damped in time at different rates, the contour plots of Figs. 6.5 and 6.6 change in time, and the coherent mode structure is lost.

6.3.3 Wall position scan

In the following, scans of the wall position and the density profiles reveal similarities and different behaviours of the two modes.

As discussed in Ch. 4, the VDOM frequency depends on the distance between the plasma and the wall. A scan of the wall position highlights the different behaviour of the two modes. The frequency as a function of the distance between the separatrix and the wall, δ_W, is plotted in Fig. 6.8. As the wall is pushed further away from the plasma boundary to $\delta_W \approx 0.23$ m, the frequency of the higher-frequency mode is almost unaffected, while the frequency of the lower-frequency mode changes by more than 10%, its oscillation frequency varying from $189kHz$ to $170kHz$. The actual shape of the JET wall in the simulation yields equivalent results to the simplified wall

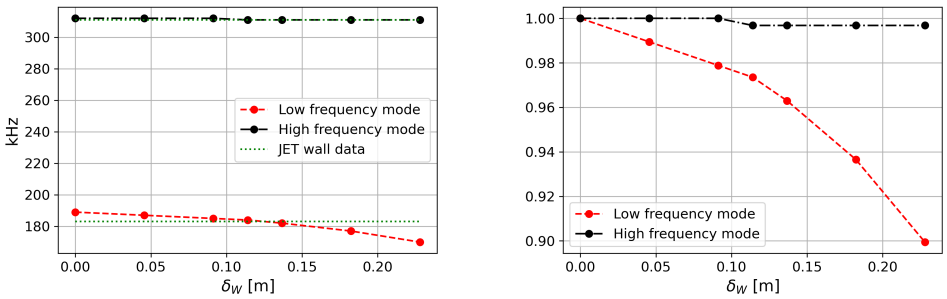

(a) (b)

Fig. 6.8 Frequency of high and low frequency modes as function δ_W. The dashed green line in Fig. 6.8a corresponds to the actual JET wall distance and shape. Figure 6.8b plots the two frequencies normalized to their maximum values, indicating percentage variations.

at a plasma-wall distance $\delta_W \approx 0.11$ m, as indicated by the green line, representing the actual wall results, in Fig. 6.8a.

The wall scan suggests that the lower-frequency mode is a VDOM. The higher-frequency mode can be identified as a Global Alfvén Eigenmode (GAE). However, further analysis is needed before this conclusion can be reached.

6.3.4 Density profile scan

The frequency of Alfvén modes scales as the inverse of the square root of the plasma density. Here, we consider the effect of changing the density profile in NIMROD simulations, effectively changing the volume-averaged plasma density. Figure 6.9 illustrates the various density profiles considered in the density scan. Throughout all profiles, the on-axis and halo region density values are kept constant at $n_0 = 5.2 \times 10^{19}$ and $n_{halo} = 5.0 \times 10^{17}$. The profiles follow $n(\psi) = (n_0 - n_{halo})(1 - \psi^{p_1})^{p_2} + n_{halo}$. By adjusting the parameter p_1 while keeping $p_2 = 0.96$ constant, we vary the volume-averaged density.

Figure 6.10 shows that the frequency of the two $n = 0$ modes follows the same decreasing trend with increasing density. As represented in Fig. 6.10b, the normalized frequency is proportional to $1/\sqrt{n}$, as expected for Alfvénic oscillations.

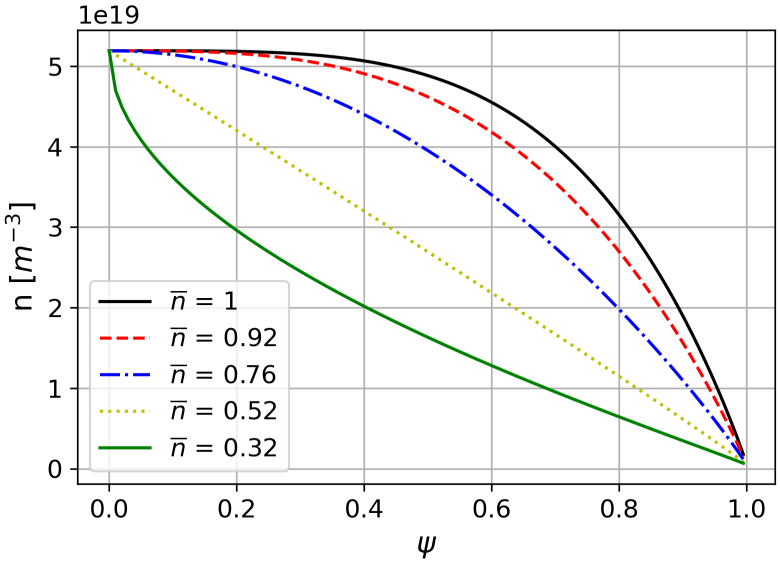

Fig. 6.9 Density profiles as functions of normalized flux. Each profile is associated to its volume averaged value, $\overline{n}$, normalized to the one of the experimental best fit (solid black curve, same as in Fig. 6.3c).

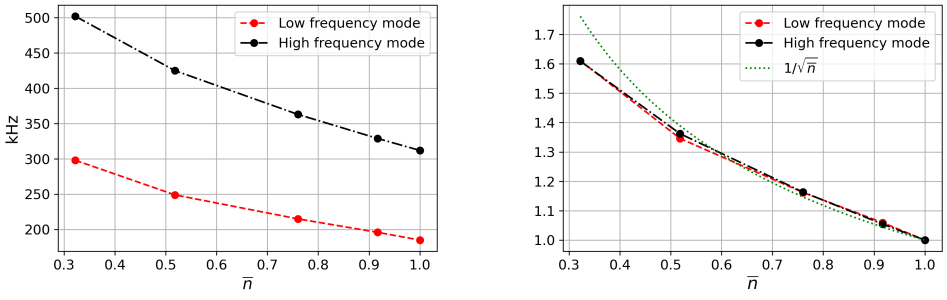

(a) (b)

Fig. 6.10 Frequency of high and low frequency modes as a function of the normalized volume averaged density, $\overline{n}$: (a) plots the two frequencies in kHz; (b) plots the two frequencies normalized to their values at $\overline{n} = 1$; the $1/\sqrt{n}$ dependence is shown by the dashed green line.

6.4 Driven Oscillator Perturbation

To study the two oscillatory modes found in Sec. 6.3 separately, an alternate perturbation is implemented in the NIMROD code. Instead of an initial "vertical push", the temperature evolution equation has been modified to include a time-dependent oscillatory term:

$$\frac{3}{2}\left(\frac{\partial}{\partial t}+\mathbf{v}\cdot\nabla\right)T=-nT\nabla\cdot\mathbf{v}+$$
$$+A\sin(2\pi f_0 t)\exp\left[\frac{(r-r_0)^2+(z-z_0)^2}{\Delta_0^2}\right] \tag{6.5}$$

where f_0 is the driven oscillation frequency for the temperature, and A is the amplitude of the driving term. A Gaussian function with width Δ_0 localizes the oscillator perturbation in space around r_0, z_0 in the poloidal plane. This forced oscillation for the temperature mimics the injection of a wave from an external antenna. Scanning the oscillator frequency, it is then possible to look for resonances in the plasma response associated with plasma normal modes. All other fields have zero initial perturbation.

These simulations use $r_0 = 2.8m$, $z_0 = 1.71m$ and $\Delta_0 = 0.5m$. The oscillator is localized to the open field line region. The amplitude A determines the amplitude of the saturated normal modes.

6.4.1 Low frequency mode

With the same simulation parameter of Sec. 6.3, we perform a scan in the oscillator frequency, f_0, in the neighborhood of the low frequency signal identified by FFT. Figure 6.11 shows the amplitude of the saturated oscillations for the normal component of the perturbed magnetic field, normalized to the off-resonance minimum amplitude value (blue dot at $f_0 = 190kHz$). For values of f_0 close to 183 kHz, the saturated value increases by more than an order of magnitude. The mode frequency and damping can be evaluated assuming the following resonance condition for a generic quantity Y:

$$Y=\frac{C}{(\omega_0-\omega)-i\gamma} \tag{6.6}$$

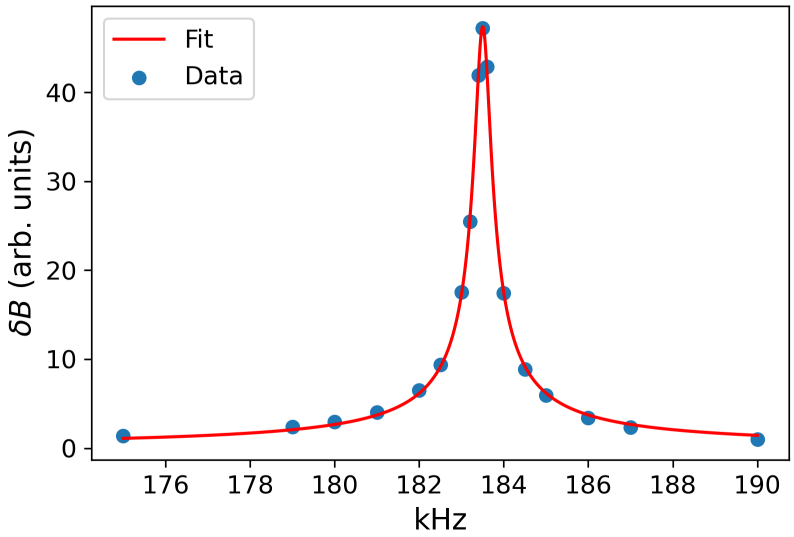

Fig. 6.11 Normalized amplitude of the normal component of the perturbed magnetic field as a function of oscillator frequency f_0 in the neighbourhood of f_{low}. Blue dots, corresponding to numerical results, are fitted by the red curve assuming the resonant condition (6.7), with $\omega_0 = 1153 \times 10^3$, $\gamma = -1.240 \times 10^3$ and $C = 58.72$.

where C is a constant, $\omega_0 = 2\pi f_0$, with ω_0 the frequency of the forcing term, ω is the frequency of the normal mode, and γ is its damping rate. The amplitude can be fit with a Lorentzian function:

$$|Y| = \frac{C}{\sqrt{(\omega_0 - \omega)^2 + \gamma^2}} \tag{6.7}$$

where ω and γ are related to the maximum and the width of the Lorentzian.

Fig. 6.11 shows the resonance peak is found for mode frequency $f = 183.5kHz$; the damping rate is $\gamma = -1240s^{-1}$. The frequency corresponds to the main peak of the FFT signal in Fig. 6.7.

Figures 6.12 and 6.13 show the time traces of the magnetic energy for resonant and off-resonant oscillator frequencies, respectively. When the oscillator resonates with the mode, a growing oscillatory pattern is obtained. The envelope of the oscillation initially grows and then saturates in time at $t > 4.0$ ms. For the off-resonant cases, we observe a clear beating between the oscillator frequency f_0 and the mode frequency f, with beating frequency $f_b = |f - f_0|$. For $t > 4.0$ ms,

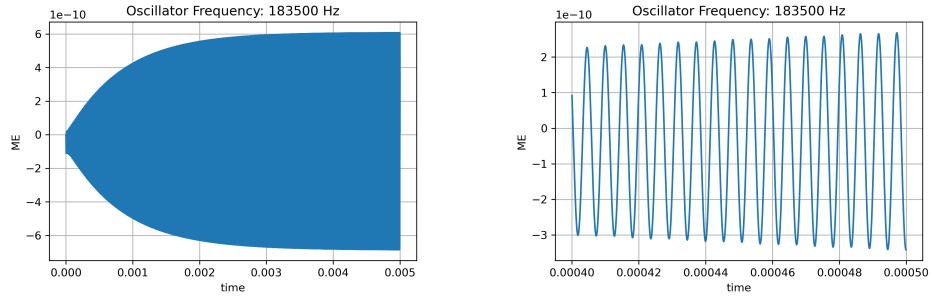

(a) (b)

Fig. 6.12 (a) Magnetic energy time trace for forced oscillator frequency at resonance, $f_0 = 183.5kHz$; (b) same as in the previous panel, zoomed in the time interval between $t = 0.4$ ms and $t = 0.5$ ms. In (a) only the envelope of the fast oscillatory behaviour is evident, due to the time range of the plot.

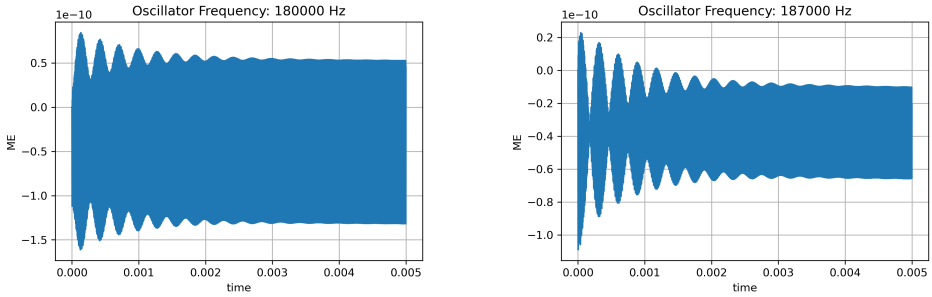

(a) (b)

Fig. 6.13 Magnetic energy time traces for two off-resonant frequencies of the forced oscillator: (a) $f_0 = 180kHz$; (b) $f_0 = 187kHz$.

the beating dies away, leaving only a constant amplitude oscillation at the forcing frequency f_0.

The level of dissipation in the system affects the damping of the mode, and consequently, it determines the width and the amplitude of the resonant peak in the plasma response, as shown in Fig. 6.14. An increase of the viscosity parameter by 20 times leads to a damping rate $\gamma = -11.8 \times 10^3 s^{-1}$. For an increase of the viscosity parameter by 20 times, the fitting parameters for Eq. 6.7 are: $\omega_0 = 1154 \times 10^3$, $\gamma = -11.79 \times 10^3$ and $C = 48.20$, showing a γ increase of ~ 10 times.

Selecting carefully the oscillator perturbation frequency f_0 it is then possible to study separately the structure of the two modes found in Sec. 6.3. This requires the forced oscillator frequency to be resonant with the mode, i.e. close to the peak

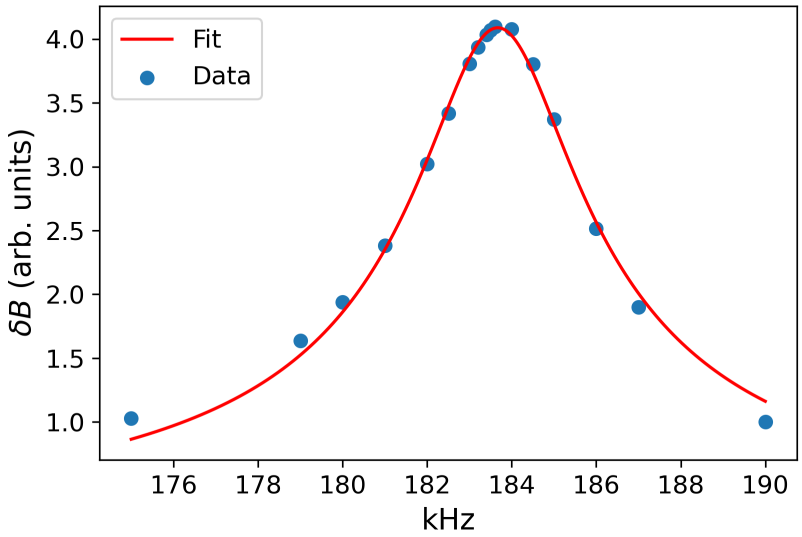

Fig. 6.14 Same as in Fig. 6.11, but for a viscosity value 20 times larger.

described by the fitting Lorentzian of Eq. 6.7, thus maximizing the plasma response. Under these conditions, choosing $f_0 = 183.5kHz$ for the low frequency mode, a m=1 mode structure in the magnetic perturbation develops, and an up-down symmetric perturbation in pressure is established, as shown in Figs. 6.15 and 6.16, which are characteristic of the VDOM described in Ch. 4. The mode structure appears to be more core localized with respect to the theoretical description, because both plasma density and current density profiles used in the simulations are peaked, while analytic theory assumed flat profiles for the sake of simplicity.

Finally, the perturbed velocity vector plot of Fig. 6.17 shows a nearly rigid vertical plasma displacement in the region where the mode is localized.

To analyze the structure of the low frequency mode in more detail, Fig. 6.18 plots the perturbed momentum in the vertical direction along horizontal and vertical slices; from the magnetic axis to the plasma edge. The normalized distances along these slices are denoted by x and y in the figure. Along the horizontal slice, the perturbed momentum is the poloidal flow multiplied by the plasma density, $n\tilde{V}_\theta$. The perturbed momentum exhibits a nearly rigid shift structure in the core region, changing sign as the plasma edge is approached. In analytic theory, as discussed in Ch. 4, the return flow is a thin layer localized at the plasma boundary, as a consequence of the step-function profiles for plasma mass and current densities and of the incompressibility of

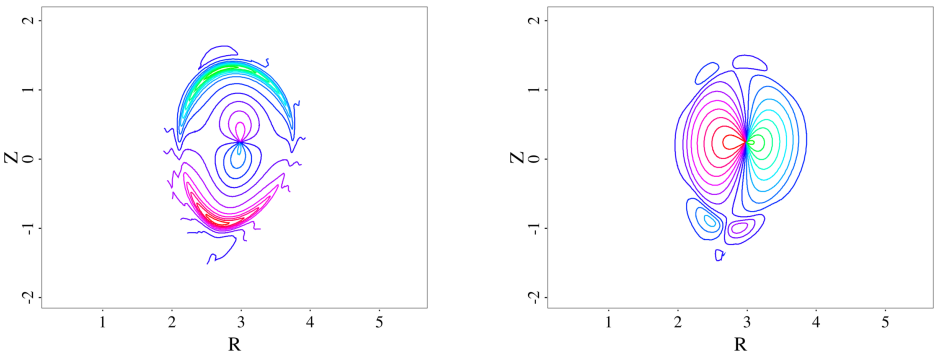

Fig. 6.15 Perturbed magnetic field components at $t = 4.4$ ms for forced oscillator frequency at resonance, $f_0 = 183.5kHz$. (a) Tangential, and (b) normal B-components with respect to the equilibrium flux surfaces.

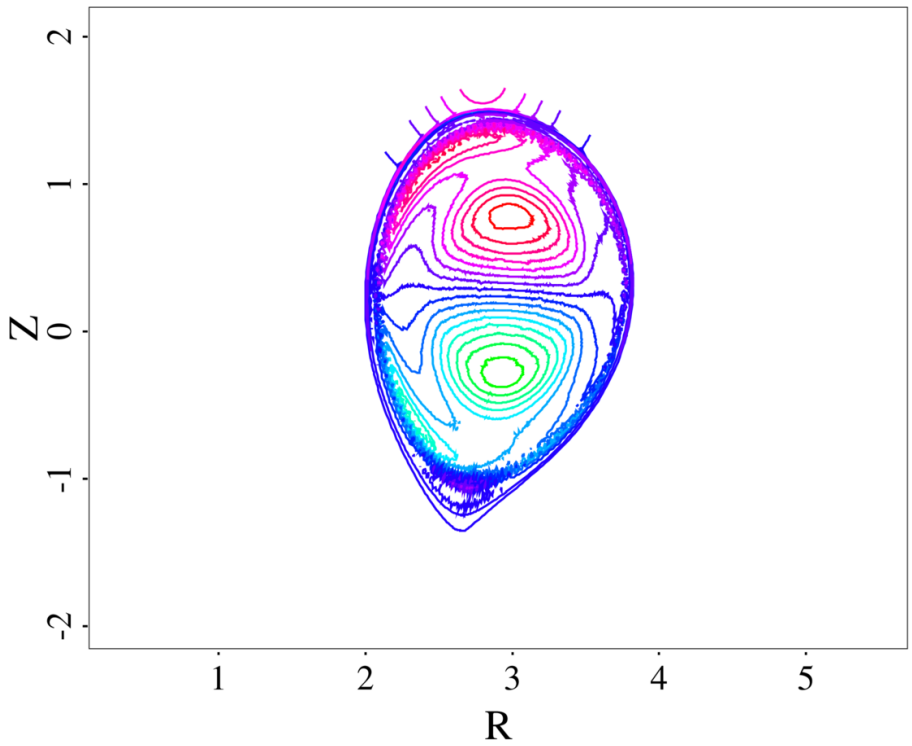

Fig. 6.16 Perturbed pressure at $t = 4.4$ ms for forced oscillator frequency at resonance, $f_0 = 183.5kHz$.

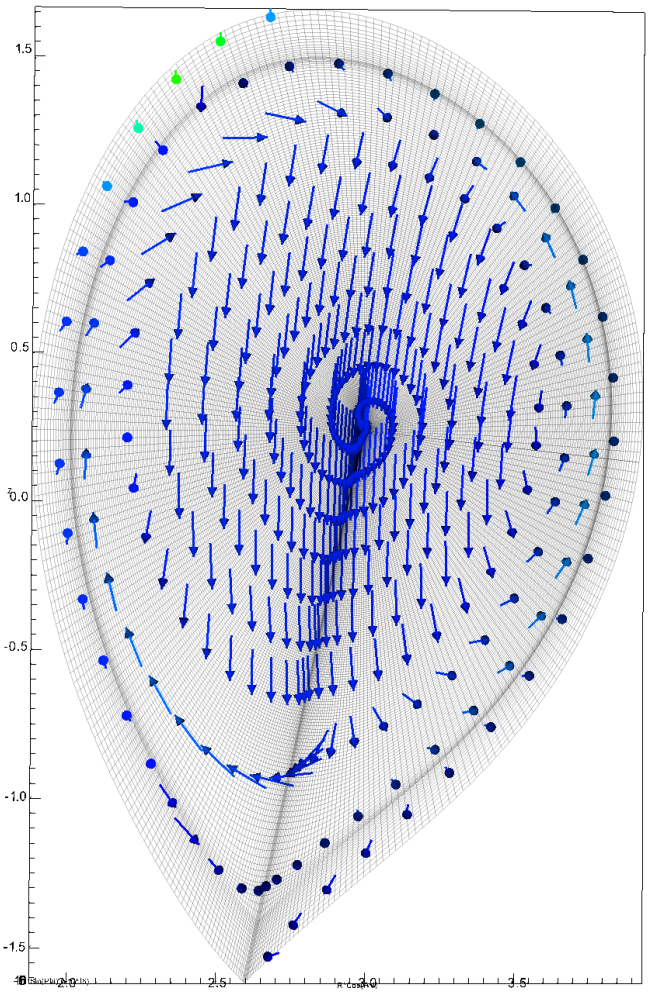

Fig. 6.17 Vector plot of $\tilde{\mathbf{v}}$ at $t = 4.4ms$ for forced oscillator frequency at resonance, $f_0 = 183.5kHz$.

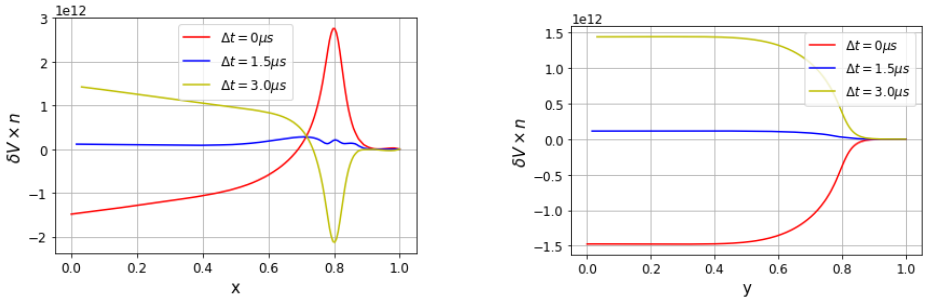

(a) (b)

Fig. 6.18 Vertical component of the perturbed momentum, plotted in (a) along a horizontal slice, and in (b) along a vertical slice, for different times during one oscillation.

the perturbation $\nabla \cdot v = 0$. In our simulations, the return flow exhibits a finite spatial extent inside the plasma. This behavior is consistent with the condition $\nabla \cdot v = 0$. The region in which the return flow propagates is affected by the finite gradient of the density profile in the plasma, deviating from the assumption of a uniform profile of the theoretical model. A more in-depth analysis of this feature is planned for a future study. Along the vertical slice, Fig. 6.18b, the vertical component of the perturbed momentum is the radial flow multiplied by the plasma density, $n_0 \tilde{V}_r$, which is nearly constant in the plasma core and decreases monotonically to zero at the plasma edge.

The mode structure obtained for the low frequency mode exhibits the important characteristics associated with the VDOM, as highlighted later in Table 6.1. The non-uniform plasma and current density profiles considered in the numerical simulation have an important impact on the mode structure. However, a global nearly rigid shift is maintained in the plasma core, while a return flow is localized around the plasma edge. The lower mode frequency depends on the plasma-wall distance, as shown by Fig. 6.8, and scales inversely with the square root of the plasma density, as shown by Fig. 6.10. These results allow us to conclude that the low-frequency mode is indeed a Vertical Displacement Oscillatory Mode. This is the first time that the VDOM is identified in a simulation using realistic tokamak parameters.

6.4.2 High frequency mode

The same analysis is now repeated for the higher-frequency mode, scanning the forced oscillator frequency in the neighbourhood of f_{high}. Figure 6.19 shows the amplitude of the saturated oscillations for the normal component of the perturbed

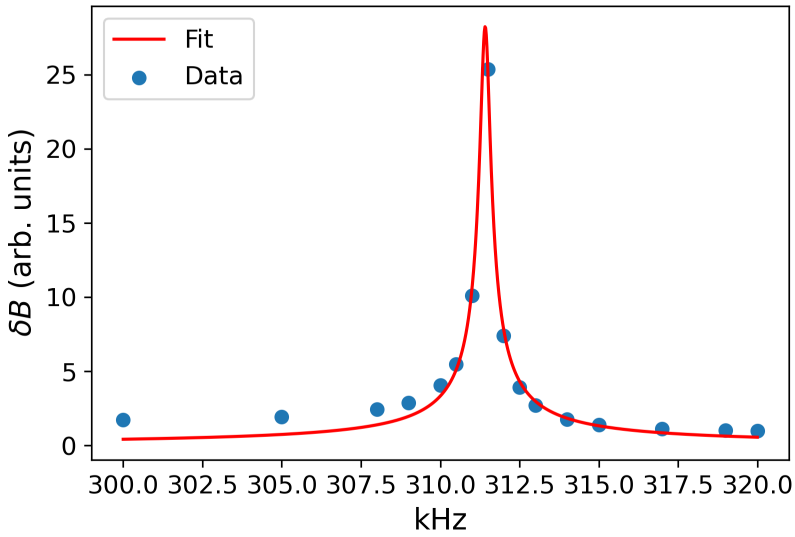

Fig. 6.19 Normalized amplitude of the normal component of the perturbed magnetic field as a function of oscillator frequency f_0 in the neighbourhood of f_{high}. Blue dots, corresponding to numerical results, are fitted by the red curve, assuming the resonant condition (6.7).

magnetic field, normalized to the off-resonance minimum amplitude value (blue dot at $f_0 = 320kHz$). A resonance is found at the frequency obtained by the FFT analysis of the plasma response following a "vertical push". The fit of the resonance condition Eq. 6.7 reveals a resonant frequency $f = 311.4kHz$ and a mode damping rate $\gamma = -1060s^{-1}$.

The mode structure near resonance ($f_0 = 311.5kHz$) is shown in Figs. 6.20 and 6.21. The higher frequency mode presents an orthogonal mode parity with respect to the lower frequency one. The vector plot of Fig. 6.22 shows a perturbed flow, oscillating inward and outward along the equatorial midplane, localized in the plasma core, together with a return poloidal flow in the outer region of the plasma. In Fig. 6.23, 1D plots of the horizontal component of the perturbed momentum along horizontal and vertical slices are shown. The mode structure is global with a strong peak of the poloidal flow, $\tilde{V}_\theta$, close to the plasma edge. This peak is located close to the minimum of the $n = 0$ Alfvén continuum, and the frequency value at the minimum of the spectrum compares well with the one obtained for the mode.

These features are characteristic of the $n = 0$ GAE, as reported in Table 6.1 in the next section, leading to the identification of the high-frequency mode in our NIMROD simulation as a GAE.

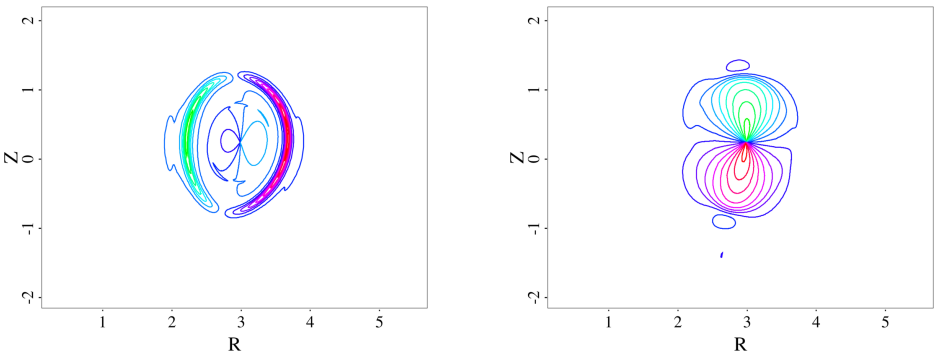

Fig. 6.20 Perturbed magnetic field components at $t = 4.5$ ms for forced oscillator frequency at resonance, $f_0 = 311.5kHz$. (a) Tangential, and (b) normal B-components with respect to the equilibrium flux surfaces.

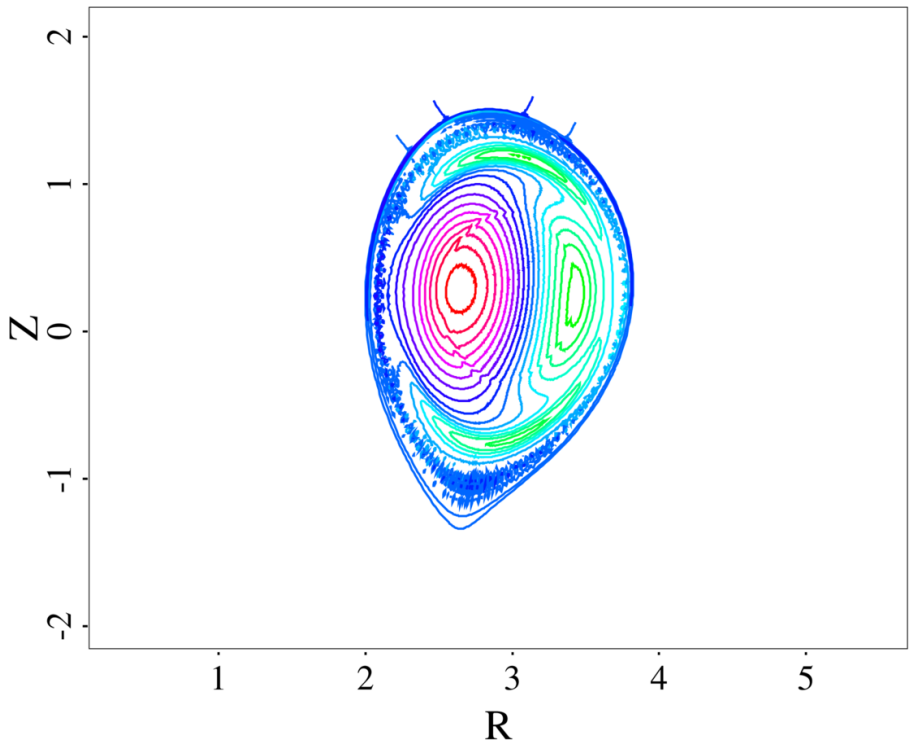

Fig. 6.21 Perturbed pressure at $t = 4.5$ ms for forced oscillator frequency at resonance, $f_0 = 311.5kHz$.

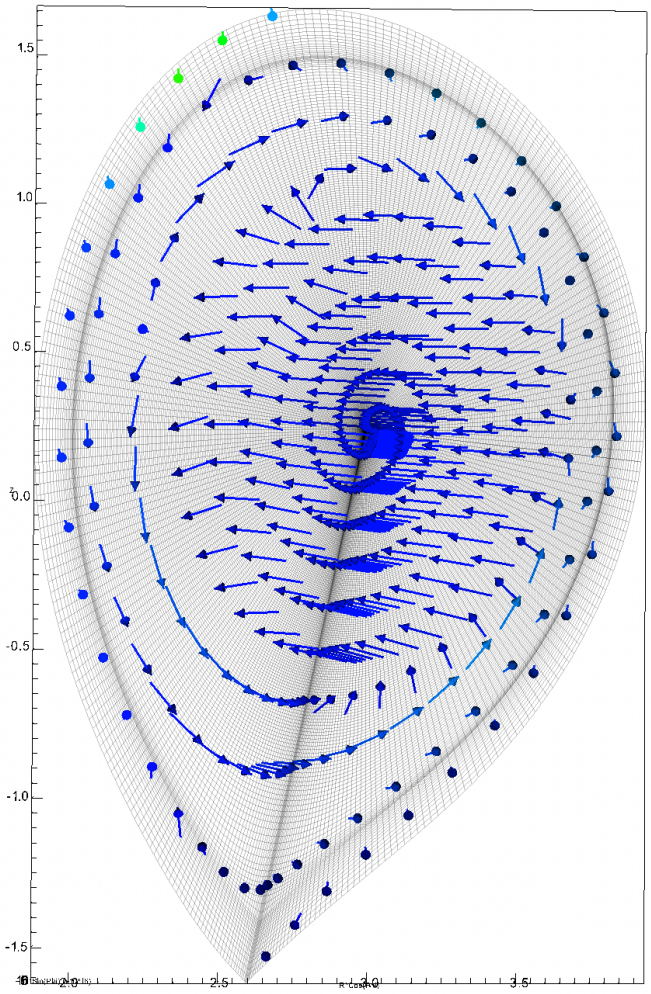

Fig. 6.22 Vector plot of the perturbed velocity $\tilde{\mathbf{v}}$ at $t = 4.5$ ms for forced oscillator frequency at resonance, $f_0 = 311.5kHz$.

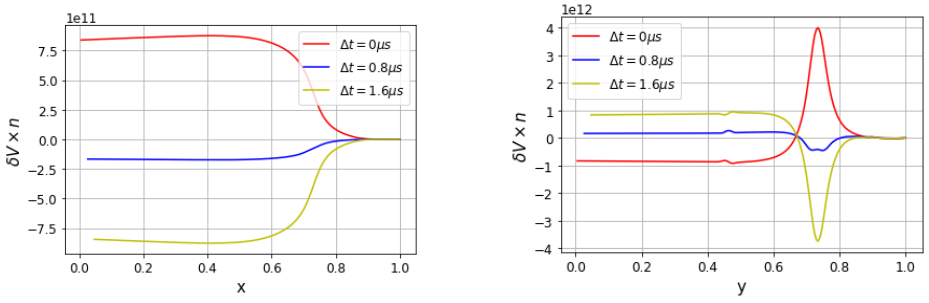

(a) (b)

Fig. 6.23 Horizontal component of the perturbed momentum, plotted in (a) along a horizontal slice, and in (b) along a vertical slice, for different times during one oscillation.

6.5 Concluding remarks

This chapter represents an initial attempt to extend the investigation of $n = 0$ vertical displacement oscillatory modes and their interaction with fast ions to more realistic tokamak conditions. The initial step involved confirming the analytic theory by validating the simplified model with the NIMROD code, which yielded excellent agreement between numerical and analytic outcomes.

In the latter part of this chapter, the analysis was expanded to characterize Vertical Displacement Oscillatory Modes (VDOM) using experimental data from JET discharges. The goal of these simulations was to offer an first description of how VDOM manifests in realistic tokamak geometries with experimental profiles. These simulations aimed to observe stable oscillatory modes, with the free energy for the modes coming either from an initial perturbation or a forced oscillator. Work is in progress to implement the distribution functions outlined in Sec.3.3 in the hybrid kinetic MHD module of the NIMROD code.

An expedient way to investigate damped modes in a numerical simulation of a tokamak plasma, used here for the first time in NIMROD simulations, has been to introduce forced oscillations of the perturbed plasma temperature with a prescribed value of the forcing frequency. When the oscillator frequency matches that of a plasma normal mode, a resonance occurs, which allows the normal mode to grow to a finite amplitude and to be fully resolved numerically. In this way, we can study the normal mode, without relying on carefully selected initial conditions, which facilitates the identification of its distinctive physical properties.

Our simulations suggest the presence of two distinct Alfvén modes as potential explanations for the observations in JET: a lower-frequency $n = 0$ mode, approximately at 180 kHz, identified as a Vertical Displacement Oscillatory Mode (VDOM), and a higher-frequency $n = 0$ mode, around 310 kHz, identified as a Global Alfvén Eigenmode (GAE). In JET discharge #102371, the $n = 0$ mode was excited with a frequency of 320 kHz. If the numerically resolved mode frequency is the sole criterion for comparison with experimental data, one might be inclined to conclude that the observed mode in JET shot 102371 is a GAE. However, it's important to note that both GAE and VDOM could potentially be excited in future tokamak experiments, depending on specific plasma conditions.

A comparison between VDOM and GAE reveals distinctions in their characteristics. GAE predominantly manifest as internal modes, whereas VDOM exhibit external characteristics. The radial structure of GAE results in the perturbed poloidal flow peaking near the minimum of the $n = 0$ continuum spectrum. In contrast, the radial structure of VDOM shows significant insensitivity to the q profile. Both modes are global, yet they differ in parity concerning the poloidal angle. The perturbed flow of GAE follows an even parity, signifying a side-to-side motion of the plasma core along the equatorial plane of the toroidal configuration. On the other hand, the perturbed flow of VDOM exhibits an odd parity, corresponding to a nearly rigid-shift, up-down vertical motion of the plasma core. Both GAE and VDOM frequencies scale inversely with the Alfvén time, i.e., $\omega \propto (B_p'/\rho_m)^{1/2}$. The GAE frequency aligns with the minimum of the $n = 0$ continuum spectrum, influenced by the q profile, with weak dependence on plasma-wall distance. In contrast, the VDOM frequency varies with plasma-wall distance while displaying limited sensitivity to details of the q profile. This comparison between GAE and VDOM is summarized in Table 6.1.

Chapter 7

Conclusion

7.1 Conclusions

In the next generation of magnetic confinement fusion devices, the focus is on achieving a burning plasma, where self-heating is provided by alpha particles generated with an energy of 3.5 MeV through fusion reactions in D-T plasmas. The presence of alpha particles and other energetic ions, produced via auxiliary heating, has a significant impact on the magnetohydrodynamic (MHD) stability of the plasma discharge. Wave-particle resonant interactions can induce various MHD instabilities, ranging from Energetic Particle Modes (EPMs) to the entire class of Alfvén Eigenmodes (AEs) [7–10, 33]. In this thesis, our focus is on the destabilization of Vertical Displacement Oscillatory Modes (VDOM) due to wave-particle resonances. VDOM are natural modes of oscillations in tokamak plasmas and arise due to the passive feedback stabilization of the well-known ideal vertical instability. Although the vertical plasma stability has been extensively studied, the stable branch of the dispersion relation associated with the VDOM solution has not received thorough attention. These modes are damped by wall resistivity and plasma collisional processes such as viscosity, and they are not typically observed in tokamak experiments under normal operation conditions. However, they may be driven unstable by MeV fast ions. The theoretical framework developed in this thesis represents an initial effort to characterize this new type of fast-ion driven instability, providing valuable insights for experimental investigations. Indeed, this research is partially motivated by the observation of saturated $n = 0$ fluctuations with Alfvénic frequency in recent

JET experiments involving fast ions produced by auxiliary heating, as discussed in Ref. [3] and [44], and in recent D-T discharges in presence of alpha particles.

The analytical derivation of the dispersion relation for a vertical plasma displacement is presented in Chapter 4 and is based on Ref.[15]. These vertical displacements are axisymmetric perturbations, with a toroidal mode number of $n = 0$, in a toroidal tokamak plasma. They induce an vertical motion of the entire plasma column, primarily characterized by Fourier components with an elliptical mode number of $m = 1$. The derivation is based on the reduced ideal-MHD model and assumes a simple "straight-tokamak" equilibrium with an elliptical plasma boundary and a uniform current density profile. The equilibrium assumption is motivated by the fact that the stability and growth rate of vertical displacements depend on plasma shaping and total plasma current rather than on details of current density profiles. The vertical stability analysis is conducted using the ideal-MHD energy principle. The method of quadratic forms, along with the normal-mode solution for the mode structure, is demonstrated as an efficient approach to derive the dispersion relation. The relevant dispersion relation is quadratic in γ for the ideal wall case, while it becomes cubic in γ for the resistive wall case. In the resistive wall scenario, an additional purely growing mode with zero frequency emerges, with a growth time on the order of the resistive wall time. Active feedback control systems in tokamak experiments focus on suppressing this purely growing mode. The growth rate of the non-rotating $n = 0$ resistive wall mode has been studied in close to the marginal stability limit, following Ref.[16]. In this limit we showed that the resistive wall growth rate scales with a fractional power of the wall resistivity, and can be much faster than the one obtained in the standard $D > 1$ case.

The other two roots, referred to as "vertical displacement oscillatory modes" (VDOM), are purely oscillatory for the ideal wall case, when the ideal vertical instability is suppressed. These modes exhibit weak damping due to wall resistivity. However, their oscillation frequency is slightly below the poloidal Alfvén frequency, rendering them unaffected by Alfvén continuum damping. This modes can resonate with fast ion populations, generated in a tokamak plasma due to auxiliary heating and/or as products of fusion reactions.

Under specific conditions discussed in Ch.5, and based on Ref. [17], this resonant interaction has the potential to destabilize the VDOM. The stable branch of the dispersion relation linked to the VDOM solution has been expanded to include

kinetic effects arising in the presence of MeV fast ions. Utilizing the method of quadratic forms introduced in Ch.4, the contributions of energetic ions have been naturally integrated through an extended energy principle. The dispersion relation, considering the impact of wave-particle resonant interaction, can be investigated perturbatively. This involves focusing solely on the resonance contributions to the growth rate of the VDOM, while disregarding effects on the mode frequency. The instability can be driven by a mode-particle resonant interaction involving fast ions on both trapped and passing orbits. The necessary conditions for instability is a distribution function of the fast ions with positive slope with respect to energy or anisotropy in velocity space. Various distribution functions have been explored, such as a slowing-down inverted by losses and a single-pitch slowing down. Determining a critical fast ion density threshold for instability involves evaluating the interplay between the drive from mode-particle resonance and damping introduced by the resistive wall. A distribution function influenced by sawtooth oscillations may provide the free energy necessary for the mode destabilization under particular conditions that are under investigation.

The analytic results discussed so far have relied on our simplified "straight-tokamak" equilibrium. In Ch. 6, these analytic findings on $n = 0$ modes have been successfully replicated using the extended-MHD code NIMROD. The close agreement between analytic theory and numerical results serves as a robust benchmark and a valuable initial point for further numerical explorations of $n = 0$ modes in experimental tokamak configurations with realistic plasma geometries. Discrepancies observed between analytic and numerical outcomes have been primarily attributed to differences in the wall shape utilized in the analytic work compared to the NIMROD simulations, along with the fact that NIMROD adopts a low-density, high-resistivity halo plasma instead of the vacuum assumed in the analytic calculations. In cases where ideal-MHD vertical displacements are passively stabilized due to the presence of the ideal wall, VDOM are identified. In the simulations, VDOM exhibit weak damping, owing to the low values of plasma and halo resistivity, viscosity, and other dissipative terms.

In Chapter 6, we then reported the first numerical simulations of VDOM in realistic tokamak geometry, following Ref. [2]. The characteristics of VDOM resolved in these simulations align qualitatively very well with those obtained through analytic work based on the idealized straight tokamak equilibrium. This computational evidence conclusively establishes VDOM as natural modes of oscillations in tokamak

plasmas. For our numerical simulations, we selected the equilibrium profiles from JET discharge #102371, where $n = 0$ modes destabilized by energetic ions were observed. Our simulations reveal the presence of two distinct Alfvén modes that could potentially explain the observed phenomena in JET: a lower-frequency $n = 0$ mode at approximately 180 kHz, identified as a VDOM, and a higher-frequency $n = 0$ mode at around 310 kHz, identified as a Global Alfvén Eigenmode (GAE). We also outlined key distinctions between GAE and VDOM that could aid in experimental identification, as both modes are plausible candidates for interpreting the observed $n = 0$ modes in JET discharges.

In conclusion, this thesis has introduced a new type of fast-ion-driven instability in tokamak plasmas, dubbed as fast-ion-driven Vertical Displacement Oscillatory Modes (VDOM). The results presented are a comprehensive discussion based on the author's publications and research carried out during the Ph.D. period. Both analytical and numerical results consistently depict VDOM as external modes characterized by a nearly rigid shift mode structure, describing the entire plasma's oscillation in the vertical direction with an Alfvénic frequency. Notably, the mode frequency falls below the minimum of the Alfvén frequency for standard tokamak parameters, rendering them immune to strong continuum damping. Consequently, the resonant interaction with MeV fast ions has the potential to drive them unstable. The theoretical framework presented here serves as an initial description of these fast-ion-driven VDOM, aiming to provide a possible interpretation for the observed $n = 0$ perturbations in recent JET experiments.

The theory outlined in this thesis marks an initial exploration into understanding these $n = 0$ instabilities. However, further theoretical advancements are essential to achieve a comprehensive understanding of these phenomena, particularly in more realistic scenarios that account for non-uniform profiles and equilibrium flows. Additionally, a thorough investigation into the sources of inverted distribution functions, which drive these modes, is required. Furthermore, experimental validation of these modes through rigorous modeling remains a crucial aspect under investigation. Through such validation, the theoretical framework can be refined and its applicability to real-world plasma systems might be fully assessed.

Despite these considerations, we can highlight the significance of fast-ion-driven VDOM in tokamak plasmas. Firstly, addressing the challenge of $n = 0$ Vertical Displacement Events (VDE) is crucial for ensuring the safe operation of fusion machines.

In this context, fast-ion-driven VDOM may serve as valuable precursor modes. Their frequency carries essential information about the vertical stability of the plasma, making them potentially useful for VDE mitigation. Another intriguing aspect of fast-ion-driven VDOM is their destabilization through wave-particle resonance with MeV ions. Typically, $n = 0$ perturbations do not directly induce radial transport of resonant particles. However, they may facilitate a faster relaxation of the fast ion distribution function towards a standard slowing down distribution. In the context of alpha particles generated by fusion reactions, these processes could enhance particle slowdown, with alphas exchanging energy with plasma waves rather than electrons. This collisionless extraction of alpha particle energy, known as α-channeling, holds significant implications for the feasibility of controlled fusion energy.

References

[1] Jeffrey P. Freidberg. *Ideal MHD*. Cambridge University Press, 2014.

[2] T. Barberis, C.C. Kim, F. Porcelli, D. Banerjee, N. Hawkes, Ye. O. Kazakov, YQ. Liu, H. J. C. Oliver, S. E. Sharapov, A. Yolbarsop, NIMROD Team, and JET Contributors. Simulations of vertical displacement oscillatory modes in jet. *submitted to Nuclear Fusion*.

[3] H. J. C. Oliver, S. E. Sharapov, B. N. Breizman, and L.-J. Zheng. Axisymmetric global alfvén eigenmodes within the ellipticity-induced frequency gap in the joint european torus. *Phys. Plasmas*, 24(12):122505, 2017.

[4] J D Lawson. Some criteria for a power producing thermonuclear reactor. *Proceedings of the Physical Society. Section B*, 70(1):6, jan 1957.

[5] A.B. Zylstra, O.A. Hurricane, Callahan D.A., and et al. Burning plasma achieved in inertial fusion. *Nature*, 601:542–548, 2022.

[6] I Casiraghi, P Mantica, R Ambrosino, L Aucone, B Baiocchi, L Balbinot, T Barberis, A Castaldo, M Cavedon, L Frassinetti, P Innocente, F Koechl, S Nowak, P Agostinetti, S Ceccuzzi, L Figini, G Granucci, and P Vincenzi. Core integrated simulations for the divertor tokamak test facility scenarios towards consistent core-pedestal-sol modelling. *Plasma Physics and Controlled Fusion*, 65(3):035017, feb 2023.

[7] Liu Chen, R. B. White, and M. N. Rosenbluth. Excitation of internal kink modes by trapped energetic beam ions. *Phys. Rev. Lett.*, 52:1122–1125, Mar 1984.

[8] B. Coppi and F. Porcelli. Theoretical model of fishbone oscillations in magnetically confined plasmas. *Phys. Rev. Lett.*, 57:2272–2275, Nov 1986.

[9] G. Y. Fu and J. W. Van Dam. Excitation of the toroidicity-induced shear Alfvén eigenmode by fusion alpha particles in an ignited tokamak. *Physics of Fluids B: Plasma Physics*, 1(10):1949–1952, 10 1989.

[10] R. Betti and J.P. Freidberg. *Phys. Fluids B:Plasma Phys.*, 3:1865, 1991.

[11] Z. Chang, E.D. Fredrickson, S.J. Zweben, H.K. Park, R. Nazikian, E. Mazzucato, S.H. Batha, M.G. Bell, R.V. Budny, C.E. Bush, D.S. Darrow, D. Ernst, G.Y. Fu, R.J. Hawryluk, K.W. Hill, J.C. Hosea, A.C. Janos, D.L. Jassby, D.W. Johnson, L.C. Johnson, F.M. Levinton, D.K. Mansfield, K.M. McGuire, D.R. Mikkelsen, D. Mueller, D.K. Owens, A.T. Ramsey, S.A. Sabbagh, E.J. Synakowski, H. Takahashi, G. Taylor, M.E. Thompson, R.M. Wieland, K.-L. Wong, and M.C. Zarnstorff. Alfven frequency modes at the edge of tftr plasmas. *Nuclear Fusion*, 35(12):1469, dec 1995.

[12] K.G. McClements, L.C. Appel, M.J. Hole, and A. Thyagaraja. Excitation of axisymmetric alfvénic modes in ohmic tokamak discharges. *Nuclear Fusion*, 42(9):1155, aug 2002.

[13] L. Villard and J. Vaclavik. Alfven frequency modes and global Alfven eigenmodes. *Nucl. Fusion*, 37(11):351, oct 1997.

[14] T Barberis and F Porcelli. Velocity-space distibution function of fast ions in a sawtoothing plasma. *submitted to Plasma Physics adn Controlled Fusion*.

[15] T. Barberis, A. Yolbarsop, and F. Porcelli. Vertical displacement oscillatory modes in tokamak plasmas. *J. Plasma Phys.*, 88(5):905880511, 2022.

[16] F. Porcelli, T. Barberis, and A. Yolbarsop. Vertical displacements close to ideal-mhd marginal stability in tokamak plasmas. *Fundamental Plasma Phys.*, 5:100017, 2023.

[17] T. Barberis, F. Porcelli, and A. Yolbarsop. Fast-ion-driven vertical modes in magnetically confined toroidal plasmas. *Nucl. Fusion*, 62:064002, 2022.

[18] T Barberis D Banerjee, C C Kim and F Porcelli. Linear nimrod simulations of n=0 modes for straight tokamak configuration and comparison with analytic results. *Physics of Plasmas*, 2024.

[19] Nicholas A. Krall, Alvin W. Trivelpiece, and Robert A. Gross. Principles of Plasma Physics. *American Journal of Physics*, 41(12):1380–1381, 12 1973.

[20] R.B. White. Theory of tokamak plasmas. Elsevier, Amsterdam, 1989.

[21] R. J. Goldston. *Introduction to Plasma Physics (1st ed.)*. CRC Press., 1995.

[22] Cole D. Stephens, Xavier Garbet, and Frank Jenko. Analytic guiding center formulas for bounce-transit motion in a concentric circular, finite inverse aspect ratio tokamak geometry. *Physics of Plasmas*, 27(5):052504, 05 2020.

[23] M. D. Kruskal and C. R. Oberman. On the Stability of Plasma in Static Equilibrium. *The Physics of Fluids*, 1(4):275–280, 07 1958.

[24] F Porcelli. Fast particle stabilisation. *Plasma Physics and Controlled Fusion*, 33(13):1601, nov 1991.

[25] Theodore G. Northrop. Adiabatic charged-particle motion. *Reviews of Geophysics*, 1(3):283–304, 1963.

[26] W. W. Heidbrink and R. B. White. Mechanisms of energetic-particle transport in magnetically confined plasmas. *Physics of Plasmas*, 27(3):030901, 03 2020.

[27] Robert G. Littlejohn. Variational principles of guiding centre motion. *Journal of Plasma Physics*, 29(1):111–125, 1983.

[28] G. F. Chew, M. L. Goldberger, F. E. Low, and Subrahmanyan Chandrasekhar. The boltzmann equation an d the one-fluid hydromagnetic equations in the absence of particle collisions. *Proceedings of the Royal Society of London. Series A. Mathematical and Physical Sciences*, 236(1204):112–118, 1956.

[29] I. B. Bernstein, E. A. Frieman, Martin David Kruskal, R. M. Kulsrud, and Subrahmanyan Chandrasekhar. An energy principle for hydromagnetic stability problems. *Proceedings of the Royal Society of London. Series A. Mathematical and Physical Sciences*, 244(1236):17–40, 1958.

[30] E. Frieman and Manuel Rotenberg. On hydromagnetic stability of stationary equilibria. *Rev. Mod. Phys.*, 32:898–902, Oct 1960.

[31] T. Andreussi, P. J. Morrison, and F. Pegoraro. Hamiltonian magnetohydrodynamics: Lagrangian, Eulerian, and dynamically accessible stability—Theory. *Physics of Plasmas*, 20(9):092104, 09 2013.

[32] T. Andreussi, P. J. Morrison, and F. Pegoraro. Hamiltonian magnetohydrodynamics: Lagrangian, Eulerian, and dynamically accessible stability—Examples with translation symmetry. *Physics of Plasmas*, 23(10):102112, 10 2016.

[33] Liu Chen and Fulvio Zonca. *Rev. Mod. Phys.*, 88:015008, Mar 2016.

[34] W. Park, S. Parker, H. Biglari, M. Chance, L. Chen, C. Z. Cheng, T. S. Hahm, W. W. Lee, R. Kulsrud, D. Monticello, L. Sugiyama, and R. White. Three-dimensional hybrid gyrokinetic-magnetohydrodynamics simulation. *Physics of Fluids B: Plasma Physics*, 4(7):2033–2037, 07 1992.

[35] Cesare Tronci, Emanuele Tassi, Enrico Camporeale, and Philip J Morrison. Hybrid vlasov-mhd models: Hamiltonian vs. non-hamiltonian. *Plasma Physics and Controlled Fusion*, 56(9):095008, jul 2014.

[36] F. Porcelli, R. Stankiewicz, W. Kerner, and H. L. Berk. *Phys. Plasmas*, 1(3):470–480, 1994.

[37] J D Huba. *NRL PLASMA FORMULARY Supported by The Office of Naval Research*. Naval Research Laboratory, Washington, DC, 2013.

[38] L-G Eriksson and F Porcelli. Dynamics of energetic ion orbits in magnetically confined plasmas. *Plasma Physics and Controlled Fusion*, 43(4):R145, apr 2001.

[39] T H Stix. Heating of toroidal plasmas by neutral injection. *Plasma Physics*, 14(4):367, apr 1972.

[40] Ya.I. Kolesnichenko. Distribution function for nuclear fusion reaction products in a stationary thermonuclear reactor. *Nuclear Fusion*, 15(1):35, feb 1975.

[41] J P Friedberg. MIT lecture notes, unpublished.

[42] Ya.I. Kolesnichenko and V.V. Lutsenko. Populations of fast ions produced by neutral beam injection pulses. *Nuclear Fusion*, 59(12):126005, sep 2019.

[43] M. A. Van Zeeland, L. Bardoczi, J. Gonzalez-Martin, W.W. Heidbrink, M. Podesta, M. Austin, C.S. Collins, X.D. Du, V.N. Duarte, M. Garcia-Munoz, S. Munaretto, K.E. Thome, Y. Todo, and X. Wang. *Nucl. Fusion*, 61(6):066028, 2021.

[44] V.G. Kiptily, M. Fitzgerald, Ye.O. Kazakov, J. Ongena, M. Nocente, S.E. Sharapov, M. Dreval, Ž. Štancar, T. Craciunescu, J. Garcia, L. Giacomelli, V. Goloborodko, H.J.C. Oliver, H. Weisen, and JET Contributors. Evidence for alfvén eigenmodes driven by alpha particles in D-He3 fusion experiments on JET. *Nuclear Fusion*, 61(11):114006, oct 2021.

[45] D. J. Campbell, D. F. H. Start, J. A. Wesson, D. V. Bartlett, V. P. Bhatnagar, M. Bures, J. G. Cordey, G. A. Cottrell, P. A. Dupperex, A. W. Edwards, C. D. Challis, C. Gormezano, C. W. Gowers, R. S. Granetz, J. H. Hammen, T. Hellsten, J. Jacquinot, E. Lazzaro, P. J. Lomas, N. Lopes Cardozo, P. Mantica, J. A. Snipes, D. Stork, P. E. Stott, P. R. Thomas, E. Thompson, K. Thomsen, and G. Tonetti. Stabilization of sawteeth with additional heating in the jet tokamak. *Phys. Rev. Lett.*, 60:2148–2151, May 1988.

[46] F. Jaulmes, E. Westerhof, and H.J. de Blank. Redistribution of fast ions during sawtooth reconnection. *Nuclear Fusion*, 54(10):104013, oct 2014.

[47] N.N. Gorelenkov, S.D. Pinches, and K. Toi. Energetic particle physics in fusion research in preparation for burning plasma experiments. *Nuclear Fusion*, 54(12):125001, nov 2014.

[48] M.I. Mironov, F.S. Zaitsev, N.N. Gorelenkov, V.I. Afanasyev, F.V. Chernyshev, V.G. Nesenevich, and M.P. Petrov. Sawtooth mixing of alphas, knock-on d, and t ions, and its influence on npa spectra in iter plasma. *Nuclear Fusion*, 58(8):082030, jul 2018.

[49] Ya.I. Kolesnichenko and Yu.V. Yakovenko. Theory of fast ion transport during sawtooth crashes in tokamaks. *Nuclear Fusion*, 36(2):159, feb 1996.

[50] Ya. I. Kolesnichenko, V. V. Lutsenko, Yu. V. Yakovenko, and G. Kamelander. Theory of fast ion transport induced by sawtooth oscillations: Overview and new results. *Physics of Plasmas*, 4(7):2544–2554, 07 1997.

[51] Ya. I. Kolesnichenko, V. V. Lutsenko, R. B. White, and Yu. V. Yakovenko. Theory of resonance influence of sawtooth crashes on ions with large orbit width. *Physics of Plasmas*, 5(8):2963–2976, 08 1998.

[52] A. Bierwage, K. Shinohara, Y. Kazakov, V. G. Kiptily, Ph. Lauber, M. Nocente, Ž. Štancar, S. Sumida, M. Yagi, J. Garcia, S. Ide, and JET Contributors. *Nat. Commun.*, 13:3941, 2022.

[53] S. von Goeler, W. Stodiek, and N. Sauthoff. *Phys. Rev. Lett.*, 33:1201–1203, Nov 1974.

[54] B B Kadomtsev. *Fiz. Plazmy (Sov. J. Plasma. Phys.)*, 1 (1):710 (389), 1 1975.

[55] F Porcelli, D Boucher, and M N Rosenbluth. Model for the sawtooth period and amplitude. *Plasma Physics and Controlled Fusion*, 38(12):2163, dec 1996.

[56] J.A. Wesson. *Nucl. Fusion*, 18(1):87–132, jan 1978.

[57] A. Yolbarsop, F. Porcelli, and R. Fitzpatrick. Impact of magnetic X-points on the vertical stability of tokamak plasmas. *Nucl. Fusion*, 61:114003, 2021.

[58] D. Pfefferlé and A. Bhattacharjee. Algebraic motion of vertically displacing plasmas. *Phys. Plasmas*, 25:022516, 2018.

[59] F. Porcelli and A. Yolbarsop. Analytic equilibrium of "straight tokamak" plasma bounded by a magnetic separatrix. *Phys. Plasmas*, 26:054501, 2019.

[60] J.B. Lister, E.A. Lazarus, A.G. Kellman, J.-M. Moret, J.R. Ferron, F.J. Helton, L.L. Lao, J.A. Leuer, E.J. Strait, T.S. Taylor, and A.D. Turnbull. Experimental study of the vertical stability of high decay index plasmas in the DIII-D tokamak. *Nucl. Fusion*, 30(11):2349, 1990.

[61] E. A. Lazarus, J. B. Lister, and G. H. Neilson. Control of the vertical instability in tokamaks. *Nucl. Fusion*, 30:111, 1990.

[62] A. Portone. Active and passive stabilization of n=0 RWMs in future tokamak devices. *Nucl. Fusion*, 57:126060, 2017.

[63] M. Albanese, R. Mattei and F. Villone. Prediction of the growth rates of VDEs in JET. *Nucl. Fusion*, 44:999, Sep 2004.

[64] F Porcelli, A Yolbarsop, T Barberis, and R Fitzpatrick. Resonant axisymmetric modes. *Journal of Physics: Conference Series*, 1785(1):012004, feb 2021.

[65] A. Yolbarsop, F. Porcelli, W. Liu, and R. Fitzpatrick. Analytic theory of ideal-MHD vertical displacements in tokamak plasmas. *Plasma Phys. Contr. Fusion*, 64:105002, 2022.

[66] H. R. Strauss. *Phys. Fluids*, 19:134, 1976.

[67] G. Laval, R. Pellat, and J. L. Soule. Hydromagnetic stability of a current-carrying pinch with noncircular cross section. *Phys. Fluids*, 17:835, 1974.

[68] T. J. Schep, B. J. Braams, and F. Pegoraro. *Phys. Fluids*, 25(10):1871–1884, 1982.

[69] Jonathan P Graves. Toroidal drift precession and wave–particle interaction in shaped tokamaks with finite beta and neoclassical equilibrium effects. *Plasma Physics and Controlled Fusion*, 55(7):074009, jun 2013.

[70] Z. Qiu, F. Zonca, and L. Chen. Kinetic theories of geodesic acoustic modes: Radial structure, linear excitation by energetic particles and nonlinear saturation. *Plasma Science and Technology*, 13(3):257, jun 2011.

[71] C.R. Sovinec, A.H. Glasser, T.A. Gianakon, D.C. Barnes, R.A. Nebel, S.E. Kruger, S.J. Plimpton, A. Tarditi, M.S. Chu, and the NIMROD Team. *J. Comp. Phys.*, 195:355, 2004.

[72] L.L. Lao, H. St. John, R.D. Stambaugh, A.G. Kellman, and W. Pfeiffer. Reconstruction of current profile parameters and plasma shapes in tokamaks. *Nuclear Fusion*, 25(11):1611, nov 1985.

[73] D.P. O'Brien, L.L. Lao, E.R. Solano, M. Garribba, T.S. Taylor, J.G. Cordey, and J.J. Ellis. Equilibrium analysis of iron core tokamaks using a full domain method. *Nuclear Fusion*, 32(8):1351, aug 1992.

[74] James W. Cooley and John W. Tukey. *Mathematics of Computation*, 19:297–301, 1965.

Appendix A

Derivation of the time-dependent temperature profiles and distribution functions in presence of sawtooth oscillations

A.1 Kadomtsev reconnection

The well known Kadomtsev reconnection model described in [54] prescribes a method for the determination of the post-crash pressure profile making use of helical flux and energy conservation arguments. In particular situations, it allows for analytical work. Starting from the q profile described in Eq. (3.63), it is possible to determine analytically the mixing radius r_{mix}. Kadomtsev model is based on the assumption that magnetic surfaces with equal helical flux ψ_* reconnect, due to a growing magnetic island with poloidal and toroidal mode numbers $m/n = 1$, and that during reconnection the toroidal flux ψ_T is conserved. In cylindrical approximation we can express the normalized helical flux up to leading order in r/R as:

$$\hat{\psi}_*(r^2) = \int_0^{r^2} d\hat{r}^2 \left[q(\hat{r}^2)^{-1} - 1 \right] \tag{A.1}$$

Within the cylindrical approximation, assuming nearly constant toroidal magnetic field, the toroidal flux conservation constraint can be reconsidered as the conser-

vation of the cross-sectional area between reconnecting surfaces. The helical flux corresponding to the q profile of Eq. (3.63), reads:

$$\hat{\psi}_*{}^{pre}(r^2) = \frac{\Delta q}{q_0} r_s^2 \left(\frac{r^2}{r_s^2} - \frac{r^4}{2r_s^4} \right) \tag{A.2}$$

The magnetic axis will reconnect with the magnetic surface at $r = r_{mix}$, $\hat{\psi}_*(0) = \hat{\psi}_*(r_{mix}^2)$, resulting in $r_{mix}^2 = 2r_s^2$. Each magnetic surface inside r_s will reconnect with one outside: labeling an arbitrary radius inside the resonant surface r_1, there will be a radius r_2 at which $\hat{\psi}_*(r_1^2) = \hat{\psi}_*(r_2^2)$. From Eq. (A.2), we obtain $r_2^2 = 2r_s^2 - r_1^2$ and $r_1^2 = 2r_s^2 - r_2^2$. After the reconnection process, each reconnected surface will be again circular, with radius r_k, that can be determined form the toroidal flux (area) conservation constraint as $r_k^2 = r_2^2 - r_1^2$. Combining the two expressions we can write $r_1^2 = r_s^2 - r_k^2/2$ and $r_2^2 = r_s^2 + r_k^2/2$. In particular, the magnetic surfaces after the reconnection will be characterized by $\hat{\psi}_*{}^{rel}(r_k^2) = \hat{\psi}_*{}^{pre}(r_1^2)$. Since r_k is an arbitrary radius of the reconnected magnatic surfaces, we can obtain the reconnected helical flux, and therefore the relaxed q profile:

$$\hat{\psi}_*{}^{rel}(r^2) = \frac{1}{2} r_s^2 \frac{\Delta q}{q_0} \left(1 - \frac{r^4}{4r_s^4} \right) \tag{A.3}$$

$$\frac{d\hat{\psi}_*{}^{rel}(r^2)}{dr^2} = q(r^2)_{rel}^{-1} = 1 - \frac{1}{4} \frac{\Delta q}{q_0} \frac{r^2}{r_s^2} \tag{A.4}$$

In order to determine the relaxed pressure profile, we consider that, during the reconnection, the thermal energy of the plasma involved in the process is conserved, i.e. we impose the conservation of the thermal energy integral within the cross-sectional area between reconnecting surfaces.

$$2\pi \int_{r_1}^{r_2} dr p_{pre}(r^2) = 2\pi \int_0^{r_f} dr p_{rel}(r^2) \tag{A.5}$$

After simple manipulations, we can write

$$\int_0^{r_k^2} dr^2 p_{rel}(r^2) = \int_{r_s^2}^{r_s^2 + r_k^2/2} p_{pre}(r^2) dr^2 - \int_{r_s^2}^{r_s^2 - r_k^2/2} p_{pre}(r^2) dr^2 \tag{A.6}$$

and, differentiating with respect to r_k^2:

$$p_{rel}(r^2) = \frac{1}{2}\left[p_{pre}(r_s^2 + r^2/2) + p_{pre}(r_s^2 - r^2/2)\right] \tag{A.7}$$

If we assume that the pre-crash pressure profile inside the mixing radius $r_{mix} = \sqrt{2}r_s$ is parabolic,

$$p_{pre}(r^2) = p_0\left[1 - \frac{r^2}{r_p^2}\right] \tag{A.8}$$

where p_0 is the onaxis pressure, and $r_p > r_{mix}$, then the relaxed pressure profile is constant:

$$p_{rel}(r^2) = p_0\left[1 - \frac{r_s^2}{r_p^2}\right] = const \tag{A.9}$$

Note that a different assumption for the pre-crash pressure profile in general leads to a non-constant relaxed pressure.

The pressure profile is assumed to depend on time during sawtooth ramps according to:

$$p(r,t) = p_1(t)\left[1 - \beta(t)\frac{r^2}{r_s^2}\right]. \tag{A.10}$$

Thermal energy conservation determines the value of p_{rel},

$$\int_0^{r_{mix}^2} dr^2 p(r,t) = p_{rel} r_{mix}^2, \tag{A.11}$$

and of the parameter $\beta(t) = 1 - p_{rel}/p_1(t)$. The time dependent parameter $p_1(t)$ can be determined describing the temperature evolution during the ramp. Here, we assume that the on-axis temperature increases linearly in time from p_{rel} to $p_{pre}(0)$. In this way one obtains:

$$p_1(t) = p_0\left[1 - \frac{r_s^2}{r_p^2}\left(1 - \frac{t}{\tau_{saw}}\right)\right]. \tag{A.12}$$

With $\beta(t) = 1 - p_{rel}/p_1(t)$, the pressure profile evolution reads:

$$\begin{aligned} p(r,t) &= p_0 \left[1 - \frac{r_s^2}{r_p^2} \left(1 - \frac{t}{\tau_{saw}} \right) - \frac{r^2}{r_p^2} \frac{t}{\tau_{saw}} \right] \\ &= p_{rel} \left[1 + \frac{r_s^2 - r^2}{r_p^2 - r_s^2} \frac{t}{\tau_{saw}} \right] \end{aligned} \tag{A.13}$$

A.2 PDE solution

In this appendix we detail the solution of the differential equation

$$\frac{\partial v^3 f_\alpha}{\partial t} - \frac{v}{\tau_{sd}} \frac{\partial v^3 f_\alpha}{\partial v} + \nu_\alpha v^3 f_\alpha = v^3 S_\alpha \tag{A.14}$$

under the different assumptions considered in the main body of this article. Defining $F_\alpha = v^3 f_\alpha$, one must solve

$$\frac{\partial F_\alpha}{\partial t} - \frac{v}{\tau_{sd}} \frac{\partial F_\alpha}{\partial v} + \nu_\alpha F_\alpha = v^3 S_\alpha \tag{A.15}$$

It is possible to restrict the analysis to the solution of the differential equation for particles born during the generic n-th sawtooth cycle (with $n\tau_{saw} < t < (n+1)\tau_{saw}$). Considering a constant slowing-down time and a varying source term, as in Sec. 3.3.3, we can solve Eq. (A.15) using the method of characteristics. The characteristics equations are:

$$v = c_1 e^{-t/\tau_{sd0}} \tag{A.16}$$

$$c_1 = v e^{t/\tau_{sd0}}. \tag{A.17}$$

These are used to solve the differential equation:

$$\frac{dF_{\alpha,n}}{dt} = v^3 S_{\alpha,n}(t,r,v) - \nu_l F_{\alpha,n}. \tag{A.18}$$

To solve Eq. (A.18) we consider:

$$F_{\alpha,n}(t,r,v) = C(t,r,v)e^{-t\nu_l} \tag{A.19}$$

$$\frac{dC}{dt} = v^3 S_{\alpha,n}(t,r,v)e^{t\nu_l} \tag{A.20}$$

and thus the integral equation:

$$C(t,r,v) = \int_{-\infty}^{t'} dt v^3 S_{\alpha,n}(t,r,v)e^{t\nu_l}. \tag{A.21}$$

The time-dependent source term can be expressed as

$$\begin{aligned} S_{\alpha,n}(r,t,v) = S_{rel}\left[1+A(r)\left(\frac{t}{\tau_{saw}}-n\right)\right]^2 \times \\ H[(n+1)\tau_{saw}-t]H[t-n\tau_{saw}]\delta(v-v_b) \end{aligned} \tag{A.22}$$

with $S_{rel} = c_S n_e^2 T_{0,rel}^2 / v_b^2$ being the source term associated with the relaxed temperature after a sawtooth crash. Applying the characteristic relation of (A.16) and integrating by exploiting the delta function properties within (A.22), we then consider the second characteristic relation A.17, leading to the following expression:

$$\begin{aligned} C(t,r,v) = v_b^2 \tau_{sd0}\left(\frac{v}{v_b}\right)^{\nu_l \tau_{sd0}} e^{t\nu_l} S_{rel} \times \\ \left\{1+A(r)\left[\frac{t}{\tau_{saw}}+\frac{\tau_{sd0}}{\tau_{saw}}\log\left(\frac{v}{v_b}\right)-n\right]\right\}^2 \times \\ H[v_b-v]H[(n+1)\tau_{saw}-t-\frac{\tau_{sd0}}{\tau_{saw}}\log\frac{v}{v_b}]\times \\ H[t+\frac{\tau_{sd0}}{\tau_{saw}}\log\frac{v}{v_b}-n\tau_{saw}] \end{aligned} \tag{A.23}$$

Lastly, from expression (A.19) for $F_{\alpha,n}$, and manipulating the argumet of the Heaviside function, one obtains the relevant distribution function describing particles born

during the n-th sawtooth cycle:

$$f_{\alpha,n}(r,t,v) = \tau_{sd0} v_b^{2-3l_\alpha} v^{-3+3l_\alpha} H\left[v_b - v\right] \times \tag{A.24}$$

$$S_{rel}\left\{1 + A(r)\left[\frac{t}{\tau_{saw}} + \frac{\tau_{sd0}}{\tau_{saw}} \log\left(\frac{v}{v_b}\right) - n\right]\right\}^2 \times$$

$$H\left[v - v_b e^{(n\tau_{saw}-t)/\tau_{sd0}}\right] H\left[v_b e^{((n+1)\tau_{saw}-t)/\tau_{sd0}} - v\right], \tag{A.25}$$

where $l_0 = \nu_l \tau_{sd0}/3$.

The same technique can be considered in order to solve Eq. (A.15) with constant source term and varying slowing-down time, as in Sec. 3.3.4). However, more care is required due to the discontinuities in τ_{sd} introduced by the sawtooth crashes. For simplicity, we neglect the loss term, i.e. we set $\nu_l = 0$. Due to the discontinuities in τ_{sd}, we consider again particles born during the n-th sawtooth cycle, but we solve the differential equation (A.15) separately for each successive sawtooth cycle. During the n-th sawtooth cycle, the slowing-down time varies according to:

$$\tau_{sd}(r,t) = \tau_{sd,rel} h_n(r,t)^{3/2} \tag{A.26}$$

defining $h_n(r,t) = 1 + A(r)\,(t/\tau_{saw} - n)$, while the constant source can be expressed as $S_\alpha = S_0 \delta(v - v_b)$.

We can proceed using the method of characteristics, with characteristic equations:

$$v = c_1 \exp\left[\frac{2\tau_{saw}}{\tau_{sd,rel} A(r)} h_n(r,t)^{-1/2}\right] \tag{A.27}$$

$$c_1 = v \exp\left[-\frac{2\tau_{saw}}{\tau_{sd,rel} A(r)} h_n(r,t)^{-1/2}\right] \tag{A.28}$$

in order to solve

$$\frac{dF_{\alpha,n}^{n-th}}{dt} = v^3 S_0 \delta(v - v_b). \tag{A.29}$$

Integrating in time, Using Eqs. (A.27) and A.28, one obtains the solution valid for the n-th sawtooth period:

$$F_{\alpha,n}^{n-th}(t,r,v) = v_b^2 S_0 \tau_{sd,rel} h_n(r, t_n^{n-th}(r,t,v))^{3/2}$$
$$H[t_n^{n-th}(r,t,v)] H[t - t_n^{n-th}(r,t,v)]$$
$$H[\tau_{saw} - t_n^{n-th}(r,t,v)] \tag{A.30}$$

where

$$t_n^{n-th}(r,t,v) = \frac{\tau_{saw}}{A(r)}\left\{[A(r)n-1]+ \frac{1}{\left[\frac{\tau_{sd,rel}A(r)}{2\tau_{saw}}\log\left(\frac{v_b}{v}\right)+h_n(r,t)^{-1/2}\right]^2}\right\} \tag{A.31}$$

We can rewrite the Heaviside function in terms of velocities:

$$F_{\alpha,n}^{n-th}(t,r,v) = v_b^2 S_0 \tau_{sd,rel} h_n(r,t_n^{n-th}(r,t,v))^{3/2} H[v_b-v]H[v_{n,max}-v]H[v-v_{n,min}] \tag{A.32}$$

with:

$$v_{n,min}^{n-th}(r,t) = v_b \times \exp\left\{-\frac{2\tau_{saw}}{\tau_{sd,rel}A(r)}\left[1-h_n(r,t)^{-1/2}\right]\right\} \tag{A.33}$$

$$v_{n,max}^{n-th}(r,t) = v_b \times \exp\left\{-\frac{2\tau_{saw}}{\tau_{sd,rel}A(r)}\left[\frac{1}{\sqrt{A(r)+1}}-h_n(r,t)^{-1/2}\right]\right\} \tag{A.34}$$

We now look for the solution associated to particles born during the n-th cycle during the (n+1)-th sawtooth cycle. In this case the source term is zero and we have to solve the following differential equation:

$$\frac{\partial F_\alpha}{\partial t} - \frac{v}{\tau_{sd}}\frac{\partial F_\alpha}{\partial v} = 0. \tag{A.35}$$

It is still possible to proceed considering the characteristic equation, but during this cycle the slowing-down time follows

$$\tau_{sd}(r,t) = \tau_{sd,rel} h_{n+1}(r,t)^{3/2}. \tag{A.36}$$

Accordingly, our characteristic equations read

$$v = c_1 \exp\left[\frac{2\tau_{saw}}{\tau_{sd,rel}A(r)} h_{n+1}(r,t)^{-1/2}\right] \tag{A.37}$$

$$c_1 = v \exp\left[-\frac{2\tau_{saw}}{\tau_{sd,rel}A(r)} h_{n+1}(r,t)^{-1/2}\right], \tag{A.38}$$

that we can use to solve:

$$\frac{dF_{\alpha,n}^{n+1-th}}{dt} = 0 \rightarrow F_{\alpha,n}^{n+1-th} = cst \tag{A.39}$$

and then match its solution with the one from the previous sawtooth period. Considering the characteristic equation (A.37), we obtain the following relation for the constant:

$$cst = F_{\alpha,n}^{n-th}(r,(n+1)\tau_{saw}, \\ c_1 \exp\left[\frac{2\tau_{saw}}{\tau_{sd,rel}A(r)} h_{n+1}(r,(n+1)\tau_{saw})^{-1/2}\right]) \tag{A.40}$$

Considering then the expression for $t_n^{n-th}(r,t,v)$ of Eq. (A.31) and the Heaviside functions of Eq. (A.32), together with the second characteristic Eq. (A.38), it is possible to obtain the solution during the (n+1)-th sawtooth period:

$$F_{\alpha,n}^{n+1-th}(t,r,v) = v_b^2 S_0 \tau_{sd,rel} h_n(r, t_n^{n+1-th}(r,t,v))^{3/2} \\ H[v_b - v]H[v_{n,max}^{n+1-th}\Delta v - v]H[v - v_{n,min}^{n+1-th}\Delta v] \tag{A.41}$$

where

$$t_n^{n+1-th}(r,t,v) = \frac{\tau_{saw}}{A(r)}\left\{[A(r)n-1]+ \right. \\ \left. \frac{1}{\left[\frac{\tau_{sd,rel}A(r)}{2\tau_{saw}}\log\left(\frac{v_b}{v}\right) + h_{n+1}(r,t)^{-1/2} - \left(1 - \frac{1}{\sqrt{A(r)+1}}\right)\right]^2}\right\} \tag{A.42}$$

and Δv is defined as:

$$\Delta v = \exp\left\{\frac{-2\tau_{saw}}{\tau_{sd,rel}A(r)}\left(1 - \frac{1}{\sqrt{A(r)+1}}\right)\right\} \tag{A.43}$$

while the new maximum and minimum velocities are:

$$v_{n,min}^{n+1-th}(r,t) = v_b \times \exp\left\{ -\frac{2\tau_{saw}}{\tau_{sd,rel}A(r)} \left[1 - h_{n+1}(r,t)^{-1/2} \right] \right\} \tag{A.44}$$

$$v_{n,max}^{n+1-th}(r,t) = v_b \times \exp\left\{ -\frac{2\tau_{saw}}{\tau_{sd,rel}A(r)} \left[\frac{1}{\sqrt{A(r)+1}} - h_{n+1}(r,t)^{-1/2} \right] \right\}. \tag{A.45}$$

4 The same procedure can be followed in order to derive the solution for later sawtooth periods ($n+2$,$n+3$,...). A recursive expression for the distribution function can be obtained for the evolution of the particles born during the n-th cycle for all times:

$$\begin{aligned} F_{\alpha,n}(r,t,v) &= S_0 v_b^2 H\left[v_b - v\right] \times \\ &\tau_{sd,rel} h_n(r, \hat{t}_n(r,t,v))^{3/2} \times \\ &H\left[v - \hat{v}_{n,min}(r,t)\right] H\left[\hat{v}_{n,max}(r,t) - v\right] \end{aligned} \tag{A.46}$$

where the generalized functions for the characteristic time, maximum and minimum velocities are defined as follows:

$$\begin{aligned} \hat{t}_n(r,t,v) = \frac{\tau_{saw}}{A(r)} \Bigg\{ & [A(r)n - 1] + \\ & \left[\frac{\tau_{sd,rel}A(r)}{2\tau_{saw}} \log\left(\frac{v_b}{v}\right) + \hat{h}_n(r,t)^{-1/2} - \right. \\ & \left. - \left\lfloor \frac{t - n\tau_{saw}}{\tau_{saw}} \right\rfloor \left(1 - \frac{1}{\sqrt{A(r)+1}} \right) \right]^{-2} \Bigg\} \end{aligned} \tag{A.47}$$

$$\hat{v}_{n,min}(r,t) = v_b \Delta v^{\left\lfloor \frac{t-n\tau_{saw}}{\tau_{saw}} \right\rfloor} \times \exp\left\{ -\frac{2\tau_{saw}}{\tau_{sd,rel}A(r)} \left[1 - \hat{h}_n(r,t)^{-1/2} \right] \right\} \tag{A.48}$$

$$\hat{v}_{n,max}(r,t) = v_b \Delta v^{\left\lfloor \frac{t-n\tau_{saw}}{\tau_{saw}} \right\rfloor} \times$$
$$\exp\left\{ -\frac{2\tau_{saw}}{\tau_{sd,rel} A(r)} \left[\frac{1}{\sqrt{A(r)+1}} - \hat{h}_n(r,t)^{-1/2} \right] \right\} \tag{A.49}$$

and the generalized function $\hat{h}(t,r)$ depends on the integer part of $(t-n\tau_{saw})/\tau_{saw}$:

$$\hat{h}_n(t,r) = 1 + A(r) \left(\frac{t}{\tau_{saw}} - n - \left\lfloor \frac{t-n\tau_{saw}}{\tau_{saw}} \right\rfloor \right). \tag{A.50}$$

Remembering the definitions of $F_{\alpha,n}$ and $h_n(t,r)$, the distribution function reads:

$$f_{\alpha,n}(r,t,v) = S_0 \frac{v_b^2}{v^3} H[v_b - v] \times$$
$$\tau_{sd,rel} \left\{ 1 + A(r) \left[\frac{\hat{t}_n(r,t,v)}{\tau_{saw}} - n \right] \right\}^{3/2} \times$$
$$H[v - \hat{v}_{n,min}(r,t)] H[\hat{v}_{n,max}(r,t) - v]. \tag{A.51}$$

In the situation with both the source term and slowing-down time depend on time through the plasma temperature, as in Sec. 3.3.5, the analytic procedure is again the one just described for the case of non-constant slowing-down time of Sec. 3.3.4. Since the source term and the slowing-down time vary in the same way, following the temperature evolution, the only additional effect of the varying source with respect to the previous case lies in the exponent of the varying temperature function, $h_n(r,t)$. The full distribution function can then be expressed as:

$$f_{\alpha,n}(r,t,v) = S_{rel} \frac{v_b^2}{v^3} H[v_b - v] \times$$
$$\tau_{sd,rel} \left\{ 1 + A(r) \left[\frac{\hat{t}_n(r,t,v)}{\tau_{saw}} - n \right] \right\}^{7/2} \times$$
$$H[v - \hat{v}_{n,min}(r,t)] H[\hat{v}_{n,max}(r,t) - v]. \tag{A.52}$$